

Particle Sensing in Gas Turbine Inlets Using Optical Measurements and Machine Learning

Chi Young Moon

Dissertation submitted to the Faculty of the
Virginia Polytechnic Institute and State University
in partial fulfillment of the requirements for the degree of

Doctor of Philosophy
in
Aerospace Engineering

K. Todd Lowe, Chair
Eric G. Paterson
W. Nathan Alexander
Lin Ma

December 17, 2020
Blacksburg, Virginia

Keywords: foreign object damage, engine health monitoring, laser diagnostics

Particle Sensing in Gas Turbine Inlets Using Optical Measurements and Machine Learning

Chi Young Moon

(Abstract)

Propulsion systems are exposed to a variety of foreign objects that can significantly damage or impact their performance. These threats can range from severe dangers such as sandstorms and volcanic eruptions, which can induce engine failure in minutes, to condensation and moisture during ground tests that can negatively impact the engine's fuel efficiency. While numerous computational and experimental studies have investigated the effects of particle ingestion on the component level, an accurate *in-situ* measurement technique is needed for a systematic understanding of the effects and real-time engine health monitoring.

Optical measurement techniques are attractive for this application due to their non-intrusive nature. However, conventional optical particle measurement methods assume the particle to be spherical, which introduces large errors for measuring particles with complex and irregular shapes, such as sand, volcanic ash, and ice crystals. The light-particle interaction contains information on the desired parameters, such as particle shape and size.

The research presented in this dissertation uses this idea for a novel particle sensor concept. Scattering and extinction of light by particles are chosen as crucial features that can identify the particle as its unique signature. Numerical tools are used to simulate the scattering and extinction for particles the sensor is expected to encounter. Machine learning models are trained using the data to use scattering and extinction as inputs and estimate the particle parameters. Different types and applications of supervised machine learning models were investigated, including a layered approach with numerous models and a generalized approach with a single neural network. The particle sensor is first demonstrated using data found in the literature. This study confirmed the importance of non-spherical particles in the library to guide the machine learning models. Further demonstrations are made at a full engine and wind tunnel scale to measure injected condensation and sand sprays, respectively. The mass flow rates of the ingested material were calculated using the model outputs and validated.

(315 words)

This work was supported by the Rolls-Royce Technologies, Inc.

Particle Sensing in Gas Turbine Inlets Using Optical Measurements and Machine Learning

Chi Young Moon

(General Audience Abstract)

Foreign objects ingested into gas turbines can cause serious damage and degrade their performance. Threats can range from sand, dust, and volcanic ash to condensation on ground and high-altitude ice crystals. On the component level, experiments and simulations have been performed to establish the performance decrease and risks to continued operations. However, there is a need for a real-time and non-intrusive measurement technique for the ingested mass. While there are established optical methods applicable for this use, these existing methods assume the particle shape to be spherical. The light-particle interaction contains information on the desired parameters, such as particle shape and size. Optical measurements of these interactions, such as scattering and extinction, can serve as "fingerprints" that can be used to estimate particle parameters.

A novel particle measurement technique utilizing supervised machine learning models is presented. The models are trained using a library containing numerically calculated scattering and extinction data. Laser scattering and extinction measurements are used as inputs for the models. This new technique is first demonstrated by sizing particles found in a particle scattering database in the literature. The method's versatility and ruggedness are then demonstrated by accurately estimating the volume flow rate of a spray nozzle spraying water into a research engine. Additionally, the mass flow of sand particles is measured using this technique in a high-speed wind tunnel, in a similar environment to an engine inlet.

Acknowledgements

None of this would have been possible without the countless people who have helped and encouraged me throughout this process. The following list should hopefully demonstrate how fortunate I have been to have so many people in my support system. First of all, this journey has led me to meeting my wife Cindy. I want to thank her for putting up with this grumpy grad student for all these years (and even becoming one herself!) and always supporting me even when I was at my lowest. And to our pup, Aurora, thank you so much for all the cuddles and being there for me whenever I needed a puppy break! To Uncle Tok and Aunt Pam, who raised me and shaped me into the person I am: thank you so much for everything. I continue to look up to you for your kindness and generosity. Thank you also to Aunt Suzie and Uncle Wil, and Aunt Soon Hwa and Uncle Tok Chin. And Thank you to Dean and Bennie Stauffer, who welcomed me into their family and gave me a sense of home in Blacksburg.

I have been very fortunate to have Dr. Lowe as my advisor. He always believed in me and was always graciously understanding when I came up short. His encouragement and extensive knowledge set me up for success. I will forever be grateful for his mentorship and guidance. I also want to thank my committee members Nathan Alexander, Lin Ma, and Eric Paterson for their valuable feedback. In addition, a large thanks to Dr. Wing Ng, who also provided me with very helpful feedback.

The fellow students I met throughout my time at Virginia Tech gave me so much encouragement and made the journey so much more enjoyable. I have also learned a tremendous amount from everyone. Many thanks to Dan Cadel, Tamy and Pedro Guimarães, Marcie Geesey, Tyler Vincent, Matt Boyda, Kyle Daniel, David Mayo, Will George, Sean Shea, Aaron Defreitas, Ashley Saltzman, Christopher Hickling, Aldo Gargiulo, Agastya Balantrapu, Javad Javaherian, Kevin D'Souza, Alka Panda, Caitlyn Edwards, Anna Wehr, Casey Duke, Adit Acharya, and many more I could not name here. I also want to thank Muzamil Pabani, Tayler Shelly, Will Arrowood, and Jaime Penese for their wonderful friendship, and their efforts to keep me sane throughout this process. To my friends from Chicago: William Syvongsa, Tom Mathews, Wes DeRish, Miriam Schmid, and Katie and Zephan Johnson, we may have spread apart, but you all still have a special place in my heart.

I must also thank the staff at the AOE department, whose assistance has been invaluable. A huge thanks to Kelsey Wall, who always provided clear advice and direction through the whole process, Cameron Hurley and Erin Wilson, who made sure we always had the equipment we needed, and Eric Greenman, Randall Monk, John Gillespie, and Gregg Perley, who spent countless

hours ensuring our safety and assisting us with the experiments. This work also would not have been possible without Dr. Gwi Bo Byun, who provided immense help and feedback throughout the entire process. Thanks also to Fred Smith, Vic Oechsle, and Loren Crook at Rolls-Royce for their support and crucial feedback.

Last but certainly not the least, to my parents: 엄마, 아빠, 항상 사랑합니다! 여기까지 올수있게 도와주시고, 제꿈을 추구할수있게 해주셔서 감사합니다. 떨어져 있어서 함께 매일 아프지만, 부모님의 지원과 애정없이는 이것을 할 수 없었습니다.

Chi Young Moon

December 2020

Contents

List of Figures **ix**

List of Tables **xii**

1 Introduction **1**

- 1.1 Structure and Contents 1
- 1.2 Attributions 2
- 1.3 Achievements 2
- 1.4 List of Publications 3

2 Literature Review **5**

- 2.1 Solid Particles 5
 - 2.1.1 Sand and Dust 5
 - 2.1.2 Volcanic Ash 7
 - 2.1.3 Damage Mechanisms 9
- 2.2 Icing and Condensation 11
 - 2.2.1 Icing 11
 - 2.2.2 Condensation and Moisture 12
- 2.3 Particle Measurement Techniques 13
 - 2.3.1 Established Methods 13
 - 2.3.2 Advanced Techniques 15
- 2.4 Concluding Remarks 17
- References 17

3 Non-spherical particle size estimation using supervised machine learning **27**

- Abstract 28
- 3.1 Introduction 28
- 3.2 Methods 28
 - 3.2.1 The Light Scattering Library 28
 - 3.2.2 Machine Learning Surrogate Models 29
- 3.3 Results 32
 - 3.3.1 Hyperparameter Optimization 32
 - 3.3.2 Classification and Regression Results 33

3.3.3	Simulated Particles	33
3.3.4	Impact of Library Size and Complexity	34
3.4	Conclusion	34
	References	35
3.5	Appendix A: Size Group Optimization	37
4	Non-intrusive optical measurements of gas turbine engine inlet condensation using machine learning	38
	Abstract	39
4.1	Introduction	40
4.2	Methods	41
4.2.1	Particle Scattering and Extinction Library	41
4.2.2	Machine Learning Models	43
4.2.3	Experimental Setup and Input Features	44
4.2.4	Flow Rate Estimation	46
4.2.5	Uncertainty Analysis	46
4.2.6	Validation Methods	46
4.3	Results and Discussion	46
4.3.1	Experimental Inputs	47
4.3.2	Particle Size and Shape Estimation	47
4.3.3	Flow Rate Estimation	47
4.4	Conclusions	48
	References	49
5	Neural-network-based instrument for particle detection and characterization	51
	Abstract	52
5.1	Introduction	52
5.2	Methods	53
5.2.1	The Particle Scattering and Extinction Library	53
5.2.2	Neural Network Model	55
5.2.3	Experimental Setup	56
5.2.4	Mass Flow Estimation	59
5.2.5	Validation Methods	60
5.3	Results and Discussion	61
5.3.1	Neural Network Training	61

5.3.2	Experimental Inputs	62
5.3.3	Neural Network Output	62
5.4	Conclusion	64
	References	65
6	The Particle Scattering and Extinction Library	67
6.1	Introduction	67
6.2	Methods	68
6.2.1	Library Parameters	68
6.2.2	Numerical Methods	73
6.3	Library Contents	75
6.3.1	Extinction Ratio	76
6.3.2	Scattering Intensities	76
6.4	Conclusions	77
	References	77
7	Conclusions and Outlook	84
7.1	Conclusions	84
7.2	Outlook	85
	References	86

List of Figures

2 Literature Review	5
2.1 The volume cumulative distribution for four test dust/sand samples. Data provided by Powder Technology, Inc. [7].	6
2.2 Scanning electron microscope images of A3 and C-spec sand. (a-b-c): A3 test dust under 100x, 1,000x, and 5,000x magnification, respectively. (d-e-f): C-spec sand under 50x, 100x, and 500x magnification, respectively.	7
2.3 A diagram describing the steps of inlet condensation and its effect on fan performance.	12
2.4 Commonly used parameters to define non-spherical particle size.	14
3 Non-spherical particle size estimation using supervised machine learning	27
3.1 Overall process scattering library population, machine learning model training, and particle size estimation.	29
3.2 The classification and regression layers for particle size estimation.	30
3.3 Classification and regression model training and optimization procedure.	31
3.4 Particles used for validation of monodisperse spheroidsizing, corresponding to the parameters in Table 4.	32
3.5 The number and volume density distribution functions for the simulated particle distribution.	32
3.6 Cross-validation error for the optimized classification models for various numbers of size groups and classification methods: ensemble (ENS), linear support vector machine (LSVM), k-nearest neighbor (KNN), and decision trees (DT).	33
3.7 Mean cross-validation RMS error for the optimized regression models for various numbers of size groups and regression methods: linear regression (LR), decision trees (DT), linear support vector machine (LSVM), and ensemble (ENS).	33
3.8 Particle size range and radius estimation using machine learning models.	33
3.9 Effect of different shapes in the scattering library on the relative RMS error on particle radius estimation.	34
4 Non-intrusive optical measurements of gas turbine engine inlet condensation using machine learning	38

4.1	A diagram describing the steps of inlet condensation and its effect on fan performance.	41
4.2	A diagram of the overall methods presented, from library population to estimating particle Sauter mean diameter (D_{32}), distribution width (σ), aspect ratio (AR), number density (C_n), and liquid volume fraction (LVF)	42
4.3	The feature space showing the ranges in the library. (a) Profiles showing different aspect ratios.	44
4.4	(a) Overall layout of the engine experiment and the location of the extinction lasers and detectors. (b) A top view of the lasers and detectors, as well as the beam paths of each laser. (c) Photos of the experimental setup, including the location of the spray nozzle.	45
4.5	(a) A schematic of the scattering setup. (b) A photo of the scattering setup beneath the test engine. (c) A photo showing the laser sheet for scattering measurements, enhanced using a smoke generator.	45
4.6	Normalized mean spray visualization images from the 65% CFS case.	48
4.7	Normalized extinction signal from the 532 nm laser.	48
4.8	Flow rate estimations from the machine learning (ML) and conventional extinction (WMLE) method, as well as the Atrato ultrasonic flowmeter.	49
5	Neural-network-based instrument for particle detection and characterization	51
5.1	A flowchart describing the overall process behind the particle sensor concept. . . .	53
5.2	Feedforward network structure for particle size, shape and distribution width estimation	55
5.3	(a) A schematic showing the wind tunnel layout, including the sand feeder and the optical measurement section. (b) A detailed view of the optical measurement section, with the extinction and scattering components la	57
5.4	A top view of the extinction setup, with the lasers located on the left and the detector components on the right. The green and red arrows indicate the paths for the 532 nm and 10330 nm laser beams, respectively.	58
5.5	A sample of the recorded extinction signal from the 532 nm detector. The detected minimums as the particles passing through the beam path are marked.	58
5.6	(a) The scattering setup showing the laser source and the scanning mirror used to create the laser sheet. (b) A side view of the scattering setup showing the three cameras located below the wind tunnel.	59

5.7	A set of instantaneous scattering images captured by the three cameras. All spatial coordinates are in μm and the contrast has been adjusted to better highlight the particles. (a) Background-subtracted scattering images. (b) The grayscale images with the edges dilated for aiding edge detection. (c) Binarized images with gaps within particles filled. (d) Detected particles that are common in all three views.	60
5.8	SEM images of CSPEC sand at three different magnifications.	61
5.9	The number of particles detected by the extinction detectors.	62
5.10	The neural network outputs from each of the experimental runs.	63
5.11	Sand mass flow rate estimation using the ML approach and monitored values from the precision scale for validation.	64
6	The Particle Scattering and Extinction Library	67
6.1	Number, area, and volume density distribution for a log-normal distribution with $D_{32} = 30 \mu\text{m}$, $\sigma = 1.5$	69
6.2	An example of an oblate spheroid, a prolate spheroid, and an ellipsoid.	71
6.3	Extinction efficiencies calculated with three different numerical schemes for spheres of various sizes and an incident wavelength of 532 nm	75
6.4	Mean efficiency ratio profiles calculated using <i>SMARTIES</i> , ray-tracing, and MatScat.	76
6.5	Extinction ratio between 10330 nm and 532 nm for the various aspect ratios and distribution widths for CSPEC sand. The refractive indices for the respective wavelengths are listed in Table 6.1.	81
6.6	Scattering profiles from the CSPEC library for various aspect ratios and Sauter mean diameters. The distribution width σ has been limited to 1.4 for clarity.	82
6.7	Scattering profiles from the CSPEC library for $D_{32} = 100 \mu\text{m}$ and $AR = 1.5$ with various aspect ratios.	83

List of Tables

3 Non-spherical particle size estimation using supervised machine learning	27
3.1 Ranges of Parameters for the Light Scattering Library	29
3.2 Input/Training Features for the Machine Learning Models.	30
3.3 Test Particles from the A&G Light Scattering Database.	31
3.4 Simulated particle parameters for mono and polydisperse validation tests.	32
3.5 Estimated particle size range and radius as well as the reference radius for the tested A&G particles.	34
3.6 The estimation results from the simulated particles.	34
4 Non-intrusive optical measurements of gas turbine engine inlet condensation using machine learning	38
4.1 Range of parameters included in the library	41
4.2 Estimated aspect ratio from the shape classifier model using the experimental inputs.	47
4.3 Sauter mean diameter estimations from the ML and conventional extinction (WMLE) method, as well as the independent estimation from the phase Doppler particle analyzer (PDPA).	47
5 Neural-network-based instrument for particle detection and characterization	51
5.1 CSPEC sand refractive indices for the three wavelengths used in the library. The data is gathered from [13–16].	54
5.2 Range of parameters included in the library	54
5.3 The results from the neural network training session.	61
5.4 D_{32} estimations from the validation measurements and the ML approach.	64
6 The Particle Scattering and Extinction Library	67
6.1 CSPEC sand refractive indices for the three wavelengths used in the library. The data is gathered from [16, 17, 18, 19].	72

[this page intentionally left blank]

1. Introduction

Propulsion systems are exposed to a variety of foreign objects that can significantly damage or impact their performance. These threats can range from severe dangers such as sandstorms and volcanic eruptions, which can induce engine failure in minutes, to condensation and moisture during ground tests that can negatively impact the engine's fuel efficiency. While numerous computational and experimental studies have investigated the effects of particle ingestion on the component level, an accurate *in-situ* measurement technique is needed for a systematic understanding of the effects and real-time engine health monitoring.

Optical measurement techniques are attractive for this application due to their non-intrusive nature. However, conventional optical particle measurement methods assume the particle to be spherical, which introduces large errors for measuring particles with complex and irregular shapes, such as sand, volcanic ash, and ice crystals. The light-particle interaction contains information on the desired parameters, such as particle shape and size.

The research presented in this dissertation uses this idea for a novel particle sensor concept. Scattering and extinction of light by particles are chosen as crucial features that can identify the particle as its unique signature. Numerical tools are used to simulate the scattering and extinction for particles the sensor is expected to encounter. Machine learning models are trained using the data to use scattering and extinction as inputs and estimate the particle parameters.

1.1 Structure and Contents

The dissertation consists of seven chapters, as described below:

Chapter 1 introduces the dissertation and lays out a general structure.

Chapter 2 provides a review of relevant literature regarding the problem of particle ingestion in gas turbines, as well as conventional and state-of-the-art particle measurement techniques.

Chapter 3 is a research article published in *Applied Optics* (doi:10.1364/AO.385750). It contains the first demonstration of the library-ML approach to particle sizing. A description and details of the library-model concept, as well as results comparing the size estimation of particles found from the Amsterdam and Grenada light scattering database are included.

Chapter 4 is a research article accepted for publication in *Measurement Science and Technology*. Based on an experiment performed at a research engine inlet, it demonstrates the sensor

approach in a realistic environment for measuring inlet condensation. It also documents the first time inlet condensation was measured without a prior calibration.

Chapter 5 is a research article to be submitted to *Optics Express*. It details an experiment performed in a high-speed wind tunnel to measure the mass flow of the sand particles injected into the flow. A generalized neural network approach replaces the layered models methods detailed in Chapters 3 and 4.

Chapter 6 is a standalone chapter containing a detailed explanation of how the particle scattering and extinction library is constructed, including the various particle parameters and the numerical tools. It also includes a discussion of the library contents prepared for the solid particle mass loading sensor, demonstrated in chapter 5.

Chapter 7 concludes the dissertation with a summary and an outlook for future work regarding this sensor technology.

Chapter formatting may vary due to submission guidelines between different publications.

1.2 Attributions

Dr. K. Todd Lowe is the primary advisor and the committee chair. He provided supervision, guidance, and manuscript edits throughout all work presented in this dissertation.

Dr. Gwi Bo Byun is a research scientist at the Advanced Propulsion and Power Lab. He provided extensive feedback and assisted in the experiments detailed in Chapters 4 and 5.

Aldo Gargiulo, Alka Panda and Caitlyn Edwards are fellow students who provided assistance and editorial guidance for work presented in Chapters 3, 4, and 5, respectively.

Fred Smith, Vic Oechsle, and Loren Crook are engineers at Rolls-Royce who regularly provided important feedback throughout all work presented in this dissertation.

1.3 Achievements

The major achievements of this work are:

- Light scattering and extinction were chosen as crucial features that can serve as a "fingerprint" to identifying particles for a sensor application. Non-spherical particles were modeled

using spheroids as surrogate shapes, and appropriate numerical tools were identified and used to generate the training data.

- Machine learning models that use particle scattering and extinction measurements as features were developed for particle size, shape, and size distribution estimation. Different types and applications of supervised machine learning models were investigated, including a layered approach with numerous models and a generalized approach with a single neural network.
- Experiments were performed at full engine and wind tunnel scale to measure injected condensation and sand sprays, respectively. The scattering and extinction measurement rigs, as well as the necessary modifications to introduce the material into the flow were designed and implemented. The mass flow rates of the ingested material were calculated using the model outputs and validated.

1.4 List of Publications

A list of publications produced by the author during his PhD work can be found below.

Peer-reviewed journal articles

- C. Y. Moon, A. Panda, G. Byun, and K. T. Lowe, "Non-intrusive optical measurements of gas turbine engine inlet condensation using machine learning" (accepted to *Measurement Science and Technology*)
- C. Y. Moon, A. Gargiulo, G. Byun, and K. T. Lowe, "Non-spherical particle size estimation using supervised machine learning," *Applied Optics*. doi: 10.1364/AO.385750

Articles in conference proceedings

- C. Y. Moon, C. Edwards, A. Panda, G. Byun, and K. T. Lowe, "Non-spherical particle size and shape estimation using machine learning," in *2020 IEEE Research and Applications of Photonics in Defense Conference (RAPID)*. doi: 10.1109/RAPID49481.2020.9195671
- C. Y. Moon, G. B. Byun, K. T. Lowe, and C. F. Smith, "Turbine Engine Ingested Particle Monitoring: A Novel Application of Quantum Cascade IR Laser Extinction," in *AIAA Propulsion and Energy 2019 Forum*. doi: 10.2514/6.2019-4339
- C. Y. Moon, D. Zhang, K. T. Lowe, and E. G. Paterson, "Decomposition of Periodic Eddies with Varying Energy in a Turbulent Flow Using a Directional Averaging Technique," in *2018*

AIAA Aerospace Sciences Meeting. doi: 10.2514/6.2018-1765

2. Literature Review

The propulsion systems on aircrafts face hostile operating environments. An important part of these threats is foreign matter ingestion. The threats can range from solid particle ingestion, such as sand, dust, volcanic ash, and hail, to aqueous types such as moisture, rain, and supercooled water. In this chapter, the problem of particle ingestion is defined for different particle types. The particle characteristics, such as size, shape, and material, are first defined, followed by their damage mechanisms. The chapter ends with a survey of conventional and state-of-the-art particle measurement methods.

2.1 Solid Particles

2.1.1 Sand and Dust

Sand and dust form the majority of the solid particles that gas turbines are likely to encounter. The method and cause for sand and dust ingestion vary from type of vehicle and operating location. Major sources of desert sand are limited to few spots (the Sahara, Middle East, central Asia, and Australia). However, sand from these areas can travel for thousands of miles, and drylands (a major source for dust) cover nearly 40% of Earth's surface and host more than 2 billion people [1, 2]. For brevity, sand and dust will be used interchangeably going forward. Commercial jets operate in areas near deserts or frequented by sand storms, which can carry particles up to thousands of feet in altitude [3, 4]. Helicopters are especially susceptible to ingesting sand and dust as they hover, takeoff, or land [4, 5].

Dust can be roughly divided into three major categories based on the size. Clay-sized particles are less than 4 μm in length. Silt-sized particles are approximately 4 to 63 μm in length, while anything larger than that can be considered as grains [2]. The vast majority of dust composition is quartz (silica or SiO_2) and alumina (Al_2O_3) [2, 6]. Other components can include organic matter, sulphates, and salts [3, 6]. While their quantity by volume/mass is low, the presence of these material can have a significant impact on the threat to gas turbines.

Since the size and material composition can vary from sample to sample, there are test dust and contaminates set by standards. ISO 12103-1 establishes standard contaminates for automotive filter testing. These samples, commonly known as Arizona road/test dust (ARD or ATD) and AC test dust, originally came from dust collected behind tractors in Arizona. The ISO 12103-1 test dust are divided into four samples by size: ultrafine (A1), fine (A2), medium (A3), and coarse (A4)

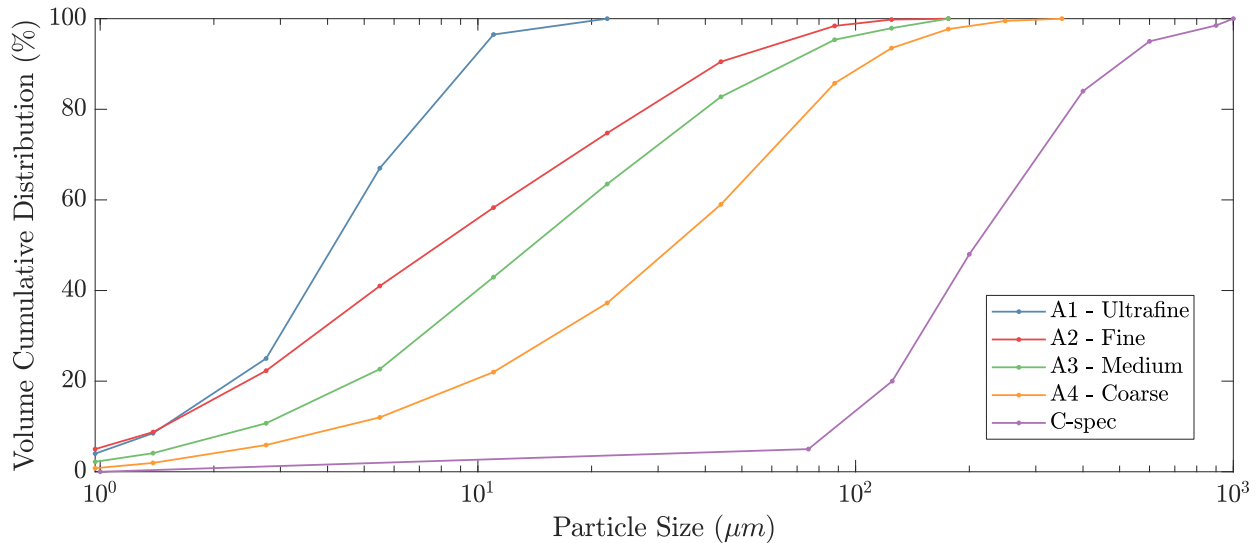


Figure 2.1: The volume cumulative distribution for four test dust/sand samples. Data provided by Powder Technology, Inc. [7].

[7]. A1 can be considered as the clay-sized particle, while A2 through A4 can be considered as silt-sized. The main components of ARD are silica and aluminum oxide. For larger particles, Mil-E-5007D/C, a US military spec for gas turbines, establishes a test sand standard using pure silica. Commonly referred as C-spec sand, these grain-sized particles are much larger than any of the ARD samples. Figure 2.1 shows the volume cumulative distribution comparisons between the four ARD samples and C-spec. Figure 2.2 is a collage of scanning electron microscope (SEM) images of A3 and C-spec sand. The difference in the particle size is demonstrated by the magnification required to show the particles. These images also show some insight into the particle shape. Both samples are clearly non-spherical. In Figure 2.2c, some specks attached to larger particles are also observed.

The wide variety of sand described above affect gas turbines differently. Safety regulations ground aircraft when conditions pose too high of a risk for flights. Grounding flights and minor exposure to dust during flight have significant economical cost through downtime and increased maintenance. However, in military or emergency uses, helicopters in particular are exposed to heavy dust and sand conditions. From the first helicopter powered by a gas turbine introduced to the U.S. military (UH-1 Huey), sand and dust particle ingestion has become a major concern for their operations [5]. During the Vietnam War, approximately 60% of unscheduled engine maintenance and removals were due to foreign object damage or sand ingestion [8]. After this experience, inlet particle separators, which rely on momentum to remove larger particles from the intake, were

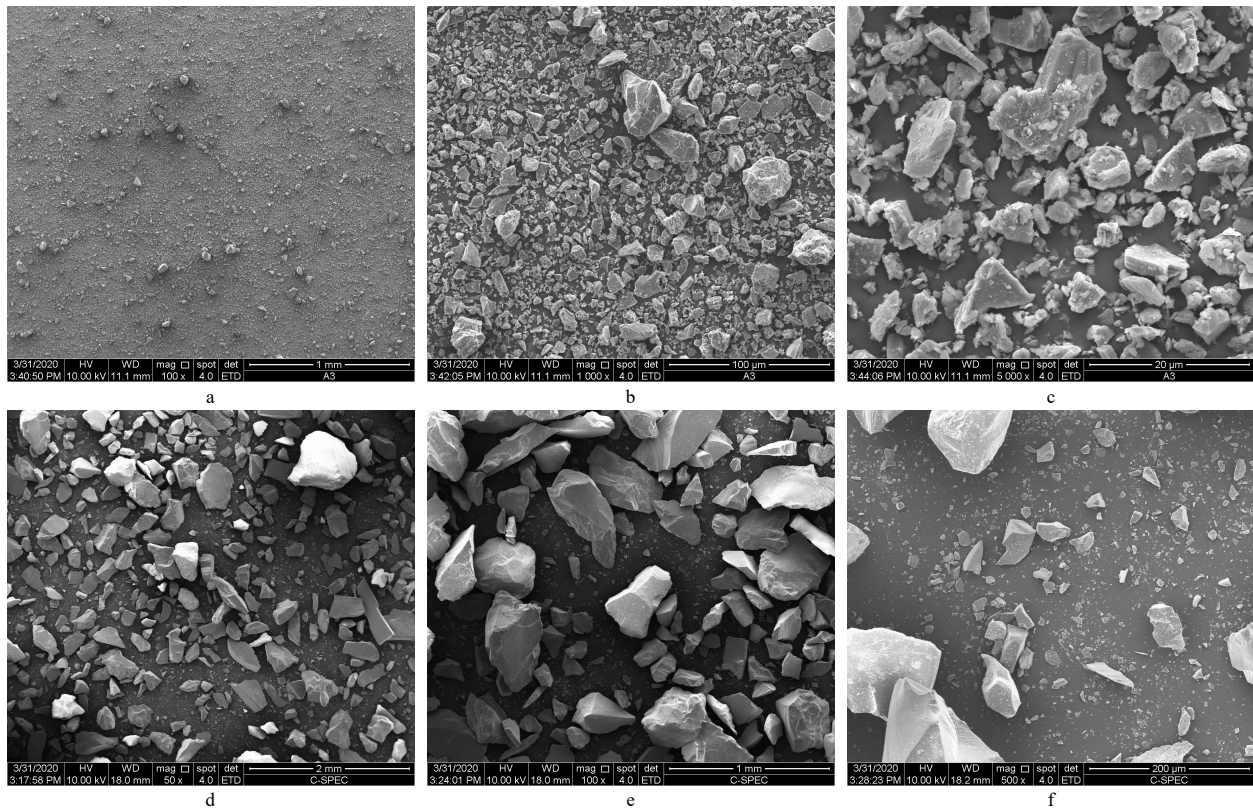


Figure 2.2: Scanning electron microscope images of A3 and C-spec sand. (a-b-c): A3 test dust under 100x, 1,000x, and 5,000x magnification, respectively. (d-e-f): C-spec sand under 50x, 100x, and 500x magnification, respectively.

installed on helicopter engines. While the separators increased operation hours, they were still limited to 50 250 hours during the first Gulf War [4, 8]. Their continued operations in the Middle-East magnifies the problem of sand ingestion for helicopters. Not limited to military uses, the air medical fleet in an Australian province was grounded for weeks in 2009 during a severe dust storms, demonstrating a critical weakness in the system [9].

2.1.2 Volcanic Ash

Volcanic ash also presents a major threat to commercial airliner's operations. While avoiding eruptions is possible, most volcanoes are not monitored in real time, ash can rise rapidly (up to 600 ft/s), and easily reach cruising altitudes of aircraft (exceeding 150,000 ft) [10]. It can drift for thousands of miles, affecting large areas where cancellations can cause significant economic damage and social disruption [3, 11]. Hours can pass before eruptions are detected via satellite images, while the physical evidences of ash encounters (odor of sulfur in the cabin, St. Elmo's

glow or electrostatic discharge on the body, and visible ash sighting) are not noticeable until well-past the safety threshold for ash concentration. [3, 12].

Volcanic ash does not deviate significantly from the composition of sand and dust presented above. The main element is still SiO_2 . Typically, volcanic ash will contain higher shares of sulphates and salts [6, 13]. For size, the range can vary from millimeters to micrometers, similar to dust and sand. Databases of particle size, composition, and SEM images for many dust and volcanic ash examples are referenced [6, 14]. For in-flight volcanic ash encounters, the majority of the coarse particles are quickly removed via gravitational settling [15, 16]. Both fluid dynamic modeling and remote sensing show that while larger particles ($63\mu\text{m} < D < 1000\mu\text{m}$) settle on the order of hours, while finer particles can linger in the atmosphere up to days [15].

The International Civil Aviation Organization's current Ash Contingency Plan describes volcanic ash contamination levels using peak mass concentration: low ($<2 \text{ mg}/\text{m}^3$), medium ($2\text{-}4 \text{ mg}/\text{m}^3$), and high ($<4 \text{ mg}/\text{m}^3$) [17]. However, the peak concentration is not the only determining factor for safe turbine operations. The exposure time is the other important factor, determining how much volcanic ash is ingested in total [3]. For example, the current Rolls-Royce guidance for its engines are set at a dosage of $14.4 \text{ g s}/\text{m}^3$, which corresponds to one hour at the medium contamination level of $4 \text{ mg}/\text{m}^3$ or two hours at $2 \text{ mg}/\text{m}^3$ [18, 3].

The difference from dust to volcanic ash is mainly the unpredictability of eruptions. Even as eruptions are on-going, a shift in the weather or intensity in the eruption can lead to aircrafts being caught at a high-risk location. Hence, while there are fewer eruptions than dust/sand storms, there are more documented volcanic ash encounters that led to significant mechanical failures in the gas turbine. From 1953 to 2009, 94 ash encounters were reported and confirmed, and 79 of those incidents caused damage to the aircraft. Nine encounters involved complete failure in one or more engines, requiring in-flight restarts. Severe damage such as engine failure can occur within minutes of exposure time, with four such incidents occurring within 10 minutes [11].

One notable eruption is the Redoubt volcano in Alaska. The eruption with ash plumes up to 22,000 ft occurred from December 1989 to June 1990. On December 15th, during one of its most vigorous eruptions, KLM Flight 867 en route to Anchorage was notified of the eruption. Even with the advance warning, the flight crew were not able to see the ash cloud and the aircraft entered the plume. While attempting to climb out of the plume, all four engines stalled within 2 minutes. The aircraft glided without power for nearly 4 minutes until 2 engines were restarted. The other two engines were restarted after another 4 minutes and the aircraft successfully landed

subsequently. During those 8 minutes, the aircraft went from 27,900 ft in altitude to 13,300 ft. The ground elevation in this area ranged from 7,000 ft to 11,000 ft, demonstrating how perilous this incident had been [19]. Lack of reliable real-time detection methods and the possibility of serious damage within minutes make volcanic ash a significant threat to aircraft.

2.1.3 Damage Mechanisms

In this section, two major damage mechanisms of solid particle ingestion in gas turbines are presented: erosion and deposition. Important factors for each mechanism, as well as the resulting impact on the turbine are surveyed from the literature.

Erosion

Erosion is the physical removal of material due to particle collision. It can occur when suspended solid particles flow into the engine and impact onto components. Cold section components, such as the fan and compressor blades are more susceptible to erosion damage as they are the first component ingested particles are likely to encounter.

Erosion on the fan and compressor blades are mainly determined by the particle size. The particle size and the flow condition determines the particle's Stokes number (St), which describes how closely the particle will follow the flow path [20]. For smaller particles ($St \ll 1$), the particles will simply move with the flow and do not interact with the fan, and are directly ingested into the core flow [15]. Particles with sufficient size ($St \geq 1$) will have too much momentum and separate from the flow path. These particles can collide with components, leading to erosion.

A computational study by Vogel et al. investigated two-phase particle-laden flows into a high-bypass gas turbine engine [15]. While the engine geometry was simplified and spherical particles were assumed to have perfect elastic collisions, the simulations confirmed the particle size dependency for fan collisions. In addition, the collisions and the flow past the fan acts as a particle separator, leading to a maximum of 30% reduction in mass concentration for larger ($> 100 \mu m$) particles in the core flow [15].

The impact of erosion on individual components has also been studied extensively through experiments and simulations. In all components, erosion changes the geometry of the affected part. For airfoils on fans, compressors, and turbine stages, erosion changes the airfoil profile, reduces the chord length, introduces surface roughness, and increases the tip clearance [5, 6, 21, 22, 23, 24, 25, 26, 27]. The increased tip clearance can lead to surges and even engine failure [26]. Changes in the

airfoil geometry deviates the component performance from design. For compressor blades, erosion typically sharpens the trailing edge and blunts the leading edge [23]. In a full-scale experiment performed by Kline et al., sand was injected into a General Electric T64 turboshaft engine to test erosion-resistant compressor fan blade coating [26]. Surging and engine failure occurred after 5.5 hours (or 35 kilograms of ingested sand). Erosion on the compressor blades without the coating was found to have been responsible for all of the engine performance losses [26].

The amount of erosion and its impact on components are determined by both the particle and body characteristics. As previously mentioned, particle size is the most important factor in whether it will collide with the components. The impact angle and velocity, as well as the particle size and shape are significant factors that affect the amount of material that is removed from the component [22, 28, 29, 30]. Volcanic ash is an example of the shape dependency; it is typically more abrasive due to the sharper angular shapes [15, 31, 32].

Deposition

Deposition is the melting of material onto components. As the particles pass through the gas turbine, they can reach their melting temperature and become molten. The molten materials can then deposit onto surfaces and cool into solids. The high temperatures required for deposition to occur limit it to the hot sections of the gas turbine: the combustion chamber and turbines.

There are many delivery mechanisms for molten particles to attach to surfaces. For larger particles ($St > 1$), just as the erosion section described, its momentum can overcome the flow and make contact with surfaces [33]. For smaller particles ($St \ll 1$), there are few explanations for particle deposits on the surface. Turbulent eddies in the flow can bring particles onto surfaces. For extremely small particles, Brownian diffusion or the random-walk process can delivery molten particles to the surface. In addition, if there is a temperature gradient between the flow and the surface, the random collision on the particle from the gas will take place more often than the face towards the surface, leading to a net force towards the surface. This process is called thermophoresis. A detailed explanation of these processes can be found in the cited references [34, 35, 36, 37].

Molten materials can block cooling channels and fuel nozzles. They can also attach to turbine blades, affecting the geometry as well as removing thermal protective coatings, sulfidation, and hot corrosion [4, 6]. The damage done to components via deposition is dependent on the amount of deposited material and particle composition. One area of focused research is based on calcium-magnesium-alumino-silicate (CMAS) attacks on turbine blade coating [3, 4, 38]. These elements

are found in sand, dirt, and volcanic ash.

The impact angle, blade geometry, and operating conditions are pivotal for understanding if deposition will occur, and if so, how much buildup will occur [4, 6]. Boulanger et al. performed a series of deposition experiments of Arizona Road Dust on Hastelloy-X, a nickel alloy analogous to turbine blade material. These experiments covered a range of impingement angles and ambient temperatures [39, 40]. Quantifying the particle deposits on the samples, an empirical relationship between the ambient temperature and the impingement angle was found [40]. Kim et al. constructed a deposition rig using combustors and guide vanes from gas turbines. Injecting volcanic ash samples, a range of turbine inlet temperatures were tested for deposition [41]. In addition to confirming the temperature dependency, this experiment revealed that an initial onset of deposition can accelerate further material accumulation [41].

2.2 Icing and Condensation

Threats from ingested particles are not limited to solids. In this section, brief overviews of two different mechanisms are presented: aircraft icing during flight and condensation ingestion on ground testing.

2.2.1 Icing

Icing occurs when aircraft fly in clouds with conditions sufficient for the droplets to freeze on impact to the body [42, 43]. Accumulation rate is dependent on two factors: the rate at which water intercepts the body in question and the rate at which the impinging water will freeze. The collection or catch efficiency, which describes the rate the water droplets will intercept the body, is dependent on both the body itself (shape, size, angle), as well as the cloud characteristics: droplet diameter and the liquid water content. The freezing rate can be defined as a heat transfer problem, dependent on ambient conditions and temperature of the body in question.

Dependent on all those variables, three different freezing mechanisms are used to describe icing problems. Rime ice forms when the supercooled droplets freeze on impact. Low ambient temperature, flow speed, and liquid water content are required for rime ice to form. When any of those quantities increase, glaze ice can form, where the droplets run along the surface before freezing. Glaze ice is smoother and more transparent than rime ice. Beak ice forms when high temperature and velocity are involved. As the higher temperature keeps the ice from fully freezing,

this slush gathers in the suction side of the airfoil, forming a beak shape [42, 44]. While most fixed wing aircraft will encounter rime and glaze ice, all three forms of ice can exist simultaneously on helicopter rotor blades [45].

Icing can affect almost every component on aircrafts. Accretion on airfoils and control surfaces is a large and active area of research [42, 43, 46, 47, 48, 49, 50]. Within gas turbines, however, inlets, fans, and compressors are the main components affected by ice accretion [51, 52, 53]. The effect of ice accretion on fan and compressor blades are similar to deposition effects. The geometry change induces deviation in lift and drag from design parameters [44]. However, the risk of permanent component damage is lower as opposed to hot deposition.

2.2.2 Condensation and Moisture

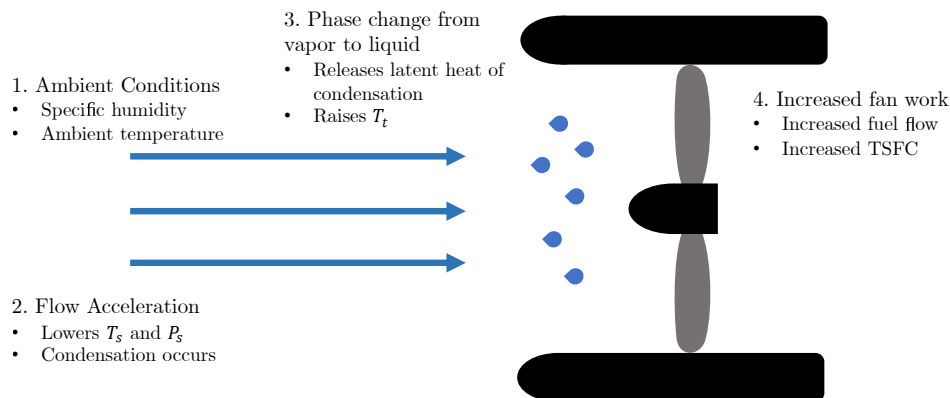


Figure 2.3: A diagram describing the steps of inlet condensation and its effect on fan performance.

Condensation and moisture ingestion can occur while on the ground. These situations include taxiing and ground tests during engine development. Figure 2.3 shows the condensation formation process. The important factors for inlet condensation formation are: the ambient (specific humidity and temperature) and inlet flow conditions (geometry and Mach number). Flow's static pressure and temperature decreases as it accelerates through the engine inlet. If sufficient conditions are met, the static pressure of the water vapor mixed within the air decreases to the saturation line, where water can exist as liquid and vapor in equilibrium. A portion of the water vapor must then condense to maintain this equilibrium, forming liquid water as condensation.

While ingesting liquid water has no destructive effects like sand or dust, the condensation formation process affects the flow to change the turbine performance. As water condenses into liquid, the released latent heat of condensation raises the total temperature of the flow. With higher total

temperature, more work by the fan is required to produce the same pressure ratio. The additional work leads to higher fuel consumption and thrust specific fuel consumption (TSFC), as much as 2%. [54]. In addition, the ingested water can form a thin layer on surfaces, including fan and compressor blades, deviating from the designed performance [55]. During gas turbine development, conditions indicating condensation effects on performance prohibits testing and valuable time and resources are lost [56]. Limited empirical corrections for performance variations are available, but an accurate measurement of the ingested liquid mass is needed to develop relationships between engine performance and condensation. Droplet volume and number density are required for this purpose. Some earlier research efforts revealed droplet size distributions ranging from 1 to 30 μm [56].

2.3 Particle Measurement Techniques

As explained in the preceding sections, particle size, shape, and composition are the important characteristics needed for accurately assessing the effect of ingested particles on gas turbine components. In this section, some established particle measurement techniques, as well as a survey of the state of the art techniques from the literature are presented.

2.3.1 Established Methods

Laser Diagnostics

The vast majority of the commercially available particle analyzers assume that the particle is spherical and its material composition is known *a priori*. Optical approaches using lasers as coherent light sources are the most ubiquitous. Assuming a spherical particle, light scattering and extinction as well as interferometry is used for particle size methods. Laser scattering methods, also sometimes known as laser diffraction, Mie scattering, and dynamic light scattering, use the scattered pattern of light from particle-laser interaction [57, 58, 59, 60]. In most devices, multiple views are used, particularly in the forward scattering region (shallow scattering angles), where the scattering intensity is sensitive to particle size. For this method, a prior knowledge of the particle material is required as the scattering pattern is also a function of the refractive index.

Another established optical technique is interferometry. Phase Doppler particle analyzers probe a small volume illuminated by crossing laser beams [61]. As particles pass through this volume, the scattered light reaches detectors. The particle size is proportional to the phase shift between the

signals. Aerodynamic drag is also proportional to the particle size. By measuring the time of flight through a known distance, the drag correlations for spherical particles can be used to determine the particle size [62].

These methods all have the benefit of accessibility through off-the-shelf devices. These devices are relatively simple to operate, with additional training available through their vendors. However, they are limited to spherical particles, and the particles must be sampled from the interested region.

Direct Imaging

Direct imaging is an established method for determining the statistical shape and size of non-spherical particles [63, 64, 65]. Using a number of lasers or LEDs as a light source, an image of particles (or sometimes the particle shadow) passing through the measurement plane is acquired. Image analysis builds a statistical database of particle size and shape characteristics.

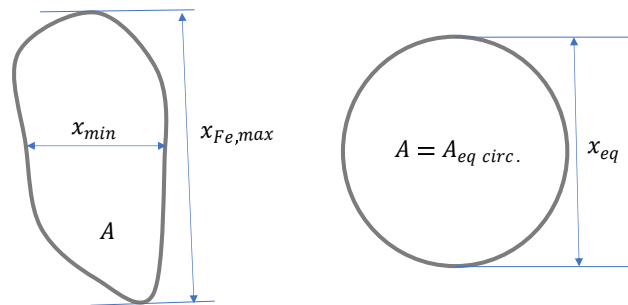


Figure 2.4: Commonly used parameters to define non-spherical particle size.

Figure 2.4 shows three commonly used parameters to define non-spherical particle size. If the shape on the left is representative of the imaged particle, x_{min} corresponds to the minimum length and is sometimes referred as the particle width. Measurements based on x_{min} correspond most closely to results acquired by physically sieving the particles. Feret maximum diameter, indicated as $x_{Fe,max}$, describes the maximum length. The circle shown in the right side of Figure 2.4 has the equivalent area to the imaged particle. The diameter of this circle is the particle's equivalent area diameter.

For quantifying particle shape, the most commonly used metric is the aspect ratio. Confusingly, its definition can vary from source to source. The definition used most often is:

$$AR = \frac{x_{min}}{x_{Fe,max}} \quad (2.1)$$

An aspect ratio of 1 indicates that the projected image of the particle is a regular polygon, such as a circle or a square. The circularity or roundness is defined as:

$$\text{Circularity} = \frac{4\pi A}{P^2} \quad (2.2)$$

where A is the area and P is the perimeter determined by the particle outline. Circularity of 1 describes a perfect circle. It is an especially useful metric for determining if the particle image contains jagged or sharp edges.

These direct imaging devices allow more accurate measurements non-spherical particle size and shape. However, for most devices, the particles must be sampled from the region of interest to be measured. Horiba's EyeCon2 is a real-time imaging device that can be placed to view a particle flow [65]. While the real-time image processing capabilities are impressive, the particle size range is limited from 50 μm to 5 mm , and the flow speed limit is 10 m/s , making it unsuitable for turbine inlet particle monitoring.

2.3.2 Advanced Techniques

Spectroscopy

Spectroscopy is the most reliable method for identifying material composition. Reflectance spectroscopy can be performed from images from the ground, aircrafts, and satellites for remote sensing of sand and dust [66, 67]. A more appropriate application of spectroscopy for inlet sensing involves breaking down the particles using directed energy. Laser-induced breakdown spectroscopy (LIBS) uses focused laser pulses to breakdown the material into plasma [68]. The spectral emission of the plasma is then captured with a spectrometer and matched to known signatures. Advancements in miniaturization allowed for a LIBS instrument called ChemCam to be a part of the Mars rover Curiosity [69, 70]. ChemCam utilizes a pulse infrared laser and records the plasma signatures ranging from near-UV to near-infrared wavelength range.

A spectrometer probe designed for monitoring gas turbine inlet particles discharges plasma to breakdown passing materials for spectroscopy measurements [71]. The bench level experiments demonstrating this concept validated its ability to determine the CMAS components of sand in a dynamic flow. In addition, a correlation between the particle size and the plasma discharge field was established, showing the ability to quantifying particle size in the future.

Interferometry

Interferometric imaging is another advanced particle measurement technique for size and shape. This category includes methods such as digital holography (DH), interferometric particle imaging, and Fourier interferometric imaging. DH is based on the interference between a reference wave and the light scattered by a particle [72, 73, 74]. The particle is not directly imaged, but reconstructed numerically using the recorded waves. It has been successfully used to measure particle size, and position and shape in 3D.

Interferometric out-of-focus imaging has been used successfully for ice crystals, sparsely populated sprays, supercooled water, and coal particles [75, 76, 77, 78, 79]. The operating principle is that the 2D Fourier transform of the out-of-focus image or interferogram is the 2D autocorrelation of particle shape, with a scaling factor. Dual-beam version of this technique has shown to improve its shape and size estimations [76]. However, at the present, even with multiple view points, it is impossible to discern viewing fields with multiple (more than 2) overlapping particles.

Machine Learning

Machine learning refers to statistical methods that can model complex systems, recognize and learn patterns, and much more. It encompasses sub-fields such as supervised and unsupervised models, artificial neural networks, and deep learning models. Therefore, there is not an exclusive way it can be applied for the purpose of particle analysis. One of the more straight forward method is to approximate complex functions for solving the inverse problem. Talebi-Moghaddam et al. measured the scattering profile of flame soot particles using a wide-angle light scattering (WALS) apparatus [80]. WALS utilizes an ellipsoidal mirror to get a wide angular range snapshot using a single camera [81, 82]. An artificial neural network trained on simulated aggregate data using the multi-sphere T-matrix method was used to estimate the soot morphological parameters. Numerous other examples of using multi-angle scattering features for particle sizing can be found in the literature, even though many are still confined to spherical particles [83, 84, 85, 86, 87].

Another strength in applied machine learning is image analysis. Convolution neural networks (CNN) are typically fully-connected multilayer neural networks that are mostly commonly used for object recognition, motion analysis, and image generation or restoration [88]. Utilizing its strength in image recognition, Li et al. used a two-channel-output CNN for identifying and segmenting images of bubbles in flow fields acquired using shadowgraphy [89]. Even the models were trained using synthetic bubble images generated another neural network [90]. Remarkable improvements,

especially for overlapped or obscured bubbles, were noticed for bubble size and shape estimation compared to conventional shadowgraph image processing procedures. Similar methods were used to segment particles in multi-phase flows and estimate the particle size distribution [91]. Image recognition neural networks have also been adapted for classifying features from hyperspectral images [92].

2.4 Concluding Remarks

In this chapter, the problem of particle ingestion was defined for the wide range of particles a gas turbine might face. The non-spherical and complex shape, a broad size range, as well as numerous particle types and materials make accurate measurements of ingested particles very challenging. In addition, the preference for a real-time and non-intrusive measurement makes many of the established and state-of-the-art techniques unfeasible as sensor technology candidates. There currently is a need for such technique that can accurately estimate the ingested mass using particle shape, size, and number density.

References

- [1] U. Safriel, Z. Adeel, D. Niemeijer, J. Puigdefabregas, R. White, R. Lal, M. Winslow, J. Ziedler, S. Prince, E. Archer, C. King, B. Shapiro, K. Wessels, T. T. Nielsen, B. Portnov, I. Reshef, J. Thornell, E. Lachman, and D. McNab, *Dryland systems*. Island Press, 2005, vol. 1, pp. 623–662.
- [2] N. Middleton, “Desert dust hazards: A global review,” *Aeolian Research*, vol. 24, pp. 53–63, Feb. 2017. [Online]. Available: <http://dx.doi.org/10.1016/j.aeolia.2016.12.001>
- [3] R. J. Clarkson, E. J. Majewicz, and P. Mack, “A re-evaluation of the 2010 quantitative understanding of the effects volcanic ash has on gas turbine engines,” *Proceedings of the Institution of Mechanical Engineers, Part G: Journal of Aerospace Engineering*, vol. 230, no. 12, pp. 2274–2291, Oct. 2016. [Online]. Available: <http://journals.sagepub.com/doi/10.1177/0954410015623372>
- [4] A. Hamed, W. C. Tabakoff, and R. Wenglarz, “Erosion and Deposition in Turbomachinery,” *Journal of Propulsion and Power*, vol. 22, no. 2, pp. 350–360, Mar. 2006. [Online]. Available: <https://arc.aiaa.org/doi/10.2514/1.18462>
- [5] V. R. Edwards and P. L. Rouse, “U.S. Army Rotorcraft Turboshaft Engines Sand & Dust Erosion Considerations,” *AGARDCP - 558*, vol. Paper 3, 1994.

- [6] C. A. Wood, S. L. Slater, M. Zonneveldt, J. Thornton, N. Armstrong, and R. A. Antoniou, “Characterisation of Dirt, Dust and Volcanic Ash: A Study on the Potential for Gas Turbine Engine Degradation,” Defence Science Technology Group, Tech. Rep., 2017. [Online]. Available: <https://www.dst.defence.gov.au/sites/default/files/publications/documents/DST-Group-TR-3367.pdf>
- [7] Powder Technology Inc., “Arizona Test Dust History.” [Online]. Available: <https://www.powdertechinc.com/test-dust-contaminants/test-dust-history/>
- [8] I. Delgado and M. Proctor, “A Review of Engine Seal Requirements for Current and Future Army Engine Platforms,” in *43rd AIAA/ASME/SAE/ASEE Joint Propulsion Conference & Exhibit*, vol. 7, no. March. Reston, Virginia: American Institute of Aeronautics and Astronautics, Jul. 2007, pp. 7110–7127. [Online]. Available: <http://arc.aiaa.org/doi/abs/10.2514/6.2007-5734>
- [9] A. L. Holyoak, P. J. Aitken, and M. S. Elcock, “Australian Dust Storm: Impact on a Statewide Air Medical Retrieval Service,” *Air Medical Journal*, vol. 30, no. 6, pp. 322–327, Nov. 2011. [Online]. Available: <http://dx.doi.org/10.1016/j.amj.2010.12.010>
- [10] G. F. Ulfarsson and E. A. Unger, “Impacts and Responses of Icelandic Aviation to the 2010 Eyjafjallajökull Volcanic Eruption,” *Transportation Research Record: Journal of the Transportation Research Board*, vol. 2214, no. 1, pp. 144–151, Jan. 2011. [Online]. Available: <http://journals.sagepub.com/doi/10.3141/2214-18>
- [11] M. Guffanti, T. J. Casadevall, and K. Budding, “Encounters of Aircraft with Volcanic Ash Clouds : A Compilation of Known Incidents , 1953 – 2009,” *U.S. Geological Survey Data Series*, vol. 545, 2009.
- [12] M. G. Dunn, “Operation of Gas Turbine Engines in an Environment Contaminated With Volcanic Ash,” *Journal of Turbomachinery*, vol. 134, no. 5, p. 051001, 2012.
- [13] R. J. Clarkson, “Engine Environmental Protection (EEP) R&T.”
- [14] O. Muñoz, F. Moreno, D. Guirado, D. Dabrowska, H. Volten, and J. Hovenier, “The Amsterdam–Granada Light Scattering Database,” *Journal of Quantitative Spectroscopy and Radiative Transfer*, vol. 113, no. 7, pp. 565–574, May 2012.
- [15] A. Vogel, A. J. Durant, M. Cassiani, R. J. Clarkson, M. Slaby, S. Diplas, K. Krüger, and A. Stohl, “Simulation of Volcanic Ash Ingestion Into a Large Aero Engine: Particle–Fan Interactions,” *Journal of Turbomachinery*, vol. 141, no. 1, pp. 1–12, Jan. 2019.
- [16] W. Rose and A. Durant, “Fine ash content of explosive eruptions,” *Journal of Volcanology and Geothermal Research*, vol. 186, no. 1-2, pp. 32–39, Sep. 2009. [Online]. Available: <http://dx.doi.org/10.1016/j.jvolgeores.2009.01.010>

- [17] ICAO, “Volcanic ash contingency plan,” International Civil Aviation Organization, Neuilly-sur-Seine, Tech. Rep., 2016. [Online]. Available: <https://www.icao.int/EURNAT/EURandNATDocuments/EUR+NATVACP.pdf>
- [18] A. J. Prata and A. T. Prata, “Eyjafjallajökull volcanic ash concentrations determined using Spin Enhanced Visible and Infrared Imager measurements,” *Journal of Geophysical Research Atmospheres*, vol. 117, no. 6, pp. 1–24, 2012.
- [19] T. J. Casadevall, “The 1989-1990 eruption of Redoubt Volcano, Alaska: impacts on aircraft operations,” *Journal of Volcanology and Geothermal Research*, vol. 62, no. 1-4, pp. 301–316, 1994.
- [20] C. T. Crowe, J. D. Schwarzkopf, M. Sommerfeld, and Y. Tsuji, *Multiphase Flows with Droplets and Particles*, 2nd ed. Boca Raton: CRC Press, 2012.
- [21] Y. N. Sugano, H and S. Taguchi, “Study on the ash erosion of axial induced draft fans for coal-fired boilers,” Mitsubishi Heavy Ind., Tech. Rep.
- [22] G. Grant and W. Tabakoff, “Erosion Prediction in Turbomachinery Resulting from Environmental Solid Particles,” *Journal of Aircraft*, vol. 12, no. 5, pp. 471–478, may 1975. [Online]. Available: <https://arc.aiaa.org/doi/10.2514/3.59826>
- [23] C. Balan and W. Tabakoff, “Axial flow compressor performance deterioration,” in *AIAA//SAE//ASEE 20th Joint Propulsion Conference, 1984*. Reston, Virginia: American Institute of Aeronautics and Astronautics, Jun. 1984. [Online]. Available: <http://arc.aiaa.org/doi/10.2514/6.1984-1208>
- [24] J. Richardson, G. P. Sallee, W. Aircraft, and E. Hartford, “Causes of high pressure compressor deterioration in service,” in *15th Joint Propulsion Conference*. Reston, Virginia: American Institute of Aeronautics and Astronautics, Jun. 1979. [Online]. Available: <http://arc.aiaa.org/doi/10.2514/6.1979-1234>
- [25] M. G. Dunn, C. Padova, J. E. Moller, and R. M. Adams, “Performance Deterioration of a Turbofan and a Turbojet Engine Upon Exposure to a Dust Environment,” *Journal of Engineering for Gas Turbines and Power*, vol. 109, no. 3, pp. 336–343, July 1987. [Online]. Available: <https://asmedigitalcollection.asme.org/gasturbinespower/article/109/3/336/406972/Performance-Deterioration-of-a-Turbofan-and-a>
- [26] M. Klein and G. Simpson, “The Development of Innovative Methods for Erosion Testing a Russian Coating on GE T64 Gas Turbine Engine Compressor Blades,” in *Volume 2: Turbo Expo 2004*. ASMEDC, jan 2004, pp. 347–352. [Online]. Available: <https://asmedigitalcollection.asme.org/GT/proceedings/GT2004/41677/347/299845>
- [27] W. Tabakoff and G. Simpson, “Experimental study of deterioration and retention on coated

- and uncoated compressor and turbine blades,” *40th AIAA Aerospace Sciences Meeting and Exhibit*, no. January, 2002.
- [28] Y. Oka, M. Nishimura, K. Nagahashi, and M. Matsumura, “Control and evaluation of particle impact conditions in a sand erosion test facility,” *Wear*, vol. 250, no. 1-12, pp. 736–743, oct 2001. [Online]. Available: <https://linkinghub.elsevier.com/retrieve/pii/S0043164801007104>
- [29] R. Kotwal and W. Tabakoff, “A New Approach for Erosion Prediction Due To Fly Ash,” *Journal of Engineering for Power*, vol. 103, no. 2, pp. 265–270, April 1981. [Online]. Available: <https://asmedigitalcollection.asme.org/gasturbinespower/article/103/2/265/451004/A-New-Approach-for-Erosion-Prediction-Due-To-Fly>
- [30] T. Wakeman and W. Tabakoff, “Measured particle rebound characteristics useful for erosion prediction.” 1982.
- [31] G. Bagheri and C. Bonadonna, “Chapter 2 - aerodynamics of volcanic particles: Characterization of size, shape, and settling velocity,” in *Volcanic Ash*, S. Mackie, K. Cashman, H. Ricketts, A. Rust, and M. Watson, Eds. Elsevier, 2016, pp. 39 – 52. [Online]. Available: <http://www.sciencedirect.com/science/article/pii/B9780081004050000057>
- [32] A. Vogel, S. Diplas, A. J. Durant, A. S. Azar, M. F. Sunding, W. I. Rose, A. Sytchkova, C. Bonadonna, K. Krüger, and A. Stohl, “Reference data set of volcanic ash physicochemical and optical properties,” *Journal of Geophysical Research: Atmospheres*, vol. 122, no. 17, pp. 9485–9514, 2017.
- [33] M. C. G. Smith, “A Theoretical Note Upon The Mechanism of Deposition in Turbine Blade Fouling,” Gt. Brit. National Gas Turbine Establishment, Tech. Rep., 1952. [Online]. Available: <https://www.osti.gov/biblio/4202598>
- [34] L. Talbot, R. K. Cheng, R. W. Schefer, and D. R. Willis, “Thermophoresiss of Particles in a Heated Boundary Layer,” Tech. Rep., 1979.
- [35] J. Cleaver and B. Yates, “A sub layer model for the deposition of particles from a turbulent flow,” *Chemical Engineering Science*, vol. 30, no. 8, pp. 983–992, aug 1975. [Online]. Available: <https://linkinghub.elsevier.com/retrieve/pii/0009250975800650>
- [36] S. K. Friedlander and H. F. Johnstone, “Deposition of Suspended Particles from Turbulent Gas Streams,” *Industrial & Engineering Chemistry*, vol. 49, no. 7, pp. 1151–1156, 1957.
- [37] C. S. Lin, R. W. Moulton, and G. L. Putnam, “Mass Transfer between Solid Wall and Fluid Streams. Mechanism and Eddy Distribution Relationships in Turbulent Flow.” *Industrial & Engineering Chemistry*, vol. 45, no. 3, pp. 636–640, 1953.
- [38] L. Li, N. Hitchman, and J. Knapp, “Failure of Thermal Barrier Coatings Subjected to CMAS Attack,” *Journal of Thermal Spray Technology*, vol. 19, no. 1-2, pp. 148–155, Jan. 2010.

- [Online]. Available: <http://link.springer.com/10.1007/s11666-009-9356-8>
- [39] A. J. Boulanger, H. D. Patel, J. Hutchinson, W. DeShong, W. Xu, W. F. Ng, and S. V. Ekkad, "Preliminary Experimental Investigation of Initial Onset of Sand Deposition in the Turbine Section of Gas Turbines," *ASME Turbo Expo 2016, Volume 1: Aircraft Engine; Fans and Blowers; Marine*, pp. 1–10, 2016. [Online]. Available: <http://proceedings.asmedigitalcollection.asme.org/proceeding.aspx?doi=10.1115/GT2016-56059>
- [40] A. Boulanger, J. Hutchinson, W. Ng, S. Ekkad, M. Keefe, W. Xu, B. Barker, and K. Hsu, "Experimental investigation of the onset of sand deposits on Hastelloy-X between 1,000°C and 1,100°C," *The Aeronautical Journal*, vol. 121, no. 1242, pp. 1187–1199, Aug. 2017. [Online]. Available: https://www.cambridge.org/core/product/identifier/S0001924017000483/type/journal_{_}article
- [41] J. Kim, M. G. Dunn, A. J. Baran, D. P. Wade, and E. L. Tremba, "Deposition of Volcanic Materials in the Hot Sections of Two Gas Turbine Engines," *Journal of Engineering for Gas Turbines and Power*, vol. 115, no. 3, p. 641, 1993. [Online]. Available: <http://gasturbinespower.asmedigitalcollection.asme.org/article.aspx?articleid=1418899>
- [42] R. W. Gent, N. P. Dart, and J. T. Cansdale, "Aircraft icing," *Philosophical Transactions of the Royal Society of London. Series A: Mathematical, Physical and Engineering Sciences*, vol. 358, no. 1776, pp. 2873–2911, Nov. 2000. [Online]. Available: <https://royalsocietypublishing.org/doi/10.1098/rsta.2000.0689>
- [43] Y. Cao, W. Tan, and Z. Wu, "Aircraft icing: An ongoing threat to aviation safety," *Aerospace Science and Technology*, vol. 75, pp. 353–385, Apr. 2018. [Online]. Available: <https://doi.org/10.1016/j.ast.2017.12.028>
- [44] "Ice Accretion Simulation," NATO Fluid Dynamics Panel Working Group 20, Tech. Rep. December, 1997.
- [45] R. Gent, R. Markiewicz, and J. Cansdale, "Further studies of helicopter rotor ice accretion and protection," 1985.
- [46] T. Cebeci and F. Kafyeke, "Aircraft Icing," *Annual Review of Fluid Mechanics*, vol. 35, no. 1, pp. 11–21, Jan. 2003. [Online]. Available: <http://www.annualreviews.org/doi/10.1146/annurev.fluid.35.101101.161217>
- [47] F. Caliskan and C. Hajiyev, "A review of in-flight detection and identification of aircraft icing and reconfigurable control," *Progress in Aerospace Sciences*, vol. 60, pp. 12–34, Jul. 2013. [Online]. Available: <http://dx.doi.org/10.1016/j.paerosci.2012.11.001>
- [48] P. Appiah-Kubi, "U.S Inflight Icing Accidents and Incidents, 2006 to 2010," Ph.D. dissertation, University of Tennessee, Knoxville, 2011.

- [49] L. Peck, C. C. Ryerson, and C. J. Martel, “Army Aircraft Icing,” Cold Regions Research and Engineering Laboratory, Tech. Rep. September, 2002.
- [50] M. M. Oleskiw, “A review of 65 years of aircraft in-flight icing research at NRC,” *Canadian Aeronautics and Space Journal*, vol. 47, no. 3, pp. 259–268, 2001.
- [51] J. J. Lacey, “Turbine Engine Icing and Ice Detection,” in *ASME 1972 International Gas Turbine and Fluids Engineering Conference and Products Show*. American Society of Mechanical Engineers, Mar. 1972. [Online]. Available: <https://asmedigitalcollection.asme.org/GT/proceedings/GT1972/79818/SanFrancisco,California,USA/230912>
- [52] T. Currie, P. Struk, J.-C. Tsao, D. Fuleki, and D. Knezevici, “Fundamental Study of Mixed-Phase Icing with Application to Ice Crystal Accretion in Aircraft Jet Engines,” in *4th AIAA Atmospheric and Space Environments Conference*. Reston, Virginia: American Institute of Aeronautics and Astronautics, Jun. 2012, pp. 1–17. [Online]. Available: <http://arc.aiaa.org/doi/10.2514/6.2012-3035>
- [53] C. Willbanks and R. J. Schulz, “Analytical Study of Icing Simulation for Turbine Engines in Altitude Test Cells,” *Journal of Aircraft*, vol. 12, no. 12, pp. 960–967, Dec. 1975. [Online]. Available: <https://arc.aiaa.org/doi/10.2514/3.59900>
- [54] J. Potter and R. P. Tatam, “Optical condensation measurement in gas turbine engine inlets,” in *Optical Technology in Fluid, Thermal, and Combustion Flow III*, S. S. Cha, J. D. Trolinger, and M. Kawahashi, Eds., vol. 3172, no. November 1997, Nov. 1997, pp. 422–433. [Online]. Available: <http://proceedings.spiedigitallibrary.org/proceeding.aspx?articleid=930786>
- [55] T. Nikolaidis, “Water ingestion effects on gas turbine engine performance,” PhD Thesis, Cranfield University, Feb. 2008.
- [56] J. Blake, “Effects of condensation in the JT9D turbofan engine bellmouth inlet,” in *11th Propulsion Conference*. Reston, Virginia: American Institute of Aeronautics and Astronautics, Sep. 1975, pp. 0–9. [Online]. Available: <http://arc.aiaa.org/doi/10.2514/6.1975-1325>
- [57] Horiba, “Partica LA-960V2.” [Online]. Available: https://www.horiba.com/en_en/products/detail/action/show/Product/partica-la-960v2-1944/
- [58] Fritsch GmbH, “Laser Particle Sizer ANALYSETTE 22 NeXT Nano.” [Online]. Available: <https://www.fritsch-international.com/particle-sizing/static-light-scattering/details/product/laser-particle-sizer-analyssette-22-next-nano/>
- [59] Microtrac, “Microtrac S3500: Particle Size Analyzer.” [Online]. Available: <https://www.microtrac.com/products/particle-size-shape-analysis/laser-diffraction/s3500/>
- [60] Malvern Panalytical, “Spraytec.” [Online]. Available: <https://www.malvernpanalytical.com/>

- en/products/product-range/spraytec
- [61] TSI Incorporated, “Phase Doppler Particle Analyzers.” [Online]. Available: [https://tsi.com/products/fluid-mechanics-systems/phase-doppler-particle-analyzers-\(pdpa\)-systems/](https://tsi.com/products/fluid-mechanics-systems/phase-doppler-particle-analyzers-(pdpa)-systems/)
- [62] —, “AERODYNAMIC PARTICLE SIZER.” [Online]. Available: [https://www.tsi.com/products/particle-sizers/particle-size-spectrometers/aerodynamic-particle-sizer-\(aps\)-spectrometer-3321/](https://www.tsi.com/products/particle-sizers/particle-size-spectrometers/aerodynamic-particle-sizer-(aps)-spectrometer-3321/)
- [63] Microtrac, “CAMSizer X2.” [Online]. Available: <https://www.microtrac.com/products/particle-size-shape-analysis/dynamic-image-analysis/camsizer-x2/function-features/>
- [64] Sympatec GmbH, “QICPIC.” [Online]. Available: <https://www.sympatec.com/en/particle-measurement/sensors/dynamic-image-analysis/qicpic/>
- [65] Horiba, “Eyecon2.” [Online]. Available: https://www.horiba.com/en_en/products/detail/action/show/Product/eyecon2tm-2000/
- [66] R. N. Clark and T. L. Roush, “Reflectance spectroscopy: Quantitative analysis techniques for remote sensing applications,” *Journal of Geophysical Research: Solid Earth*, vol. 89, no. B7, pp. 6329–6340, Jul. 1984. [Online]. Available: <http://doi.wiley.com/10.1029/JB089iB07p06329>
- [67] Y. Kaufman, A. Wald, L. Remer, Bo-Cai Gao, Rong-Rong Li, and L. Flynn, “The MODIS 2.1- μm channel-correlation with visible reflectance for use in remote sensing of aerosol,” *IEEE Transactions on Geoscience and Remote Sensing*, vol. 35, no. 5, pp. 1286–1298, 1997. [Online]. Available: <http://ieeexplore.ieee.org/document/628795/>
- [68] D. W. Hahn and N. Omenetto, “Laser-induced breakdown spectroscopy (LIBS), part I: Review of basic diagnostics and plasmaparticle interactions: Still-challenging issues within the analytical plasma community,” *Applied Spectroscopy*, vol. 64, no. 12, pp. 335–366, 2010.
- [69] R. C. Wiens, S. Maurice, B. Barraclough, M. Saccoccio, W. C. Barkley, J. F. Bell, S. Bender, J. Bernardin, D. Blaney, J. Blank *et al.*, “The chemcam instrument suite on the mars science laboratory (msl) rover: Body unit and combined system tests,” *Space science reviews*, vol. 170, no. 1-4, pp. 167–227, 2012.
- [70] S. Maurice, R. Wiens, M. Saccoccio, B. Barraclough, O. Gasnault, O. Forni, N. Mangold, D. Baratoux, S. Bender, G. Berger *et al.*, “The chemcam instrument suite on the mars science laboratory (msl) rover: Science objectives and mast unit description,” *Space science reviews*, vol. 170, no. 1-4, pp. 95–166, 2012.
- [71] G. Papadopoulos, D. Bivolaru, and J. Lin, “Real Time Gas Turbine Engine Particulate Ingestion Sensor for Particle Size and Composition,” in *Volume 6: Ceramics; Controls, Diagnostics, and Instrumentation; Education; Manufacturing Materials and Metallurgy*. ASME,

- June 2018, p. V006T05A029.
- [72] J. Katz and J. Sheng, “Applications of Holography in Fluid Mechanics and Particle Dynamics,” *Annual Review of Fluid Mechanics*, vol. 42, no. 1, pp. 531–555, Jan. 2010. [Online]. Available: <http://www.annualreviews.org/doi/10.1146/annurev-fluid-121108-145508>
- [73] M. J. Berg and G. Videen, “Digital holographic imaging of aerosol particles in flight,” *Journal of Quantitative Spectroscopy and Radiative Transfer*, vol. 112, no. 11, pp. 1776–1783, Jul. 2011. [Online]. Available: <http://dx.doi.org/10.1016/j.jqsrt.2011.01.013>
- [74] A. Wang, T. G. Dimiduk, J. Fung, S. Razavi, I. Kretzschmar, K. Chaudhary, and V. N. Manoharan, “Using the discrete dipole approximation and holographic microscopy to measure rotational dynamics of non-spherical colloidal particles,” *Journal of Quantitative Spectroscopy and Radiative Transfer*, vol. 146, pp. 499–509, Oct. 2014. [Online]. Available: <http://dx.doi.org/10.1016/j.jqsrt.2013.12.019>
- [75] M. Talbi, G. Grehan, and M. Brunel, “Interferometric particle imaging of ice particles using a multi-view optical system,” *Applied Optics*, vol. 57, no. 21, p. 6188, 2018.
- [76] X. Wu, L. Shi, Z. Lin, Y. Wu, M. Brunel, J. Jacquot, and G. Gréhan, “Dual-beam interferometric particle imaging for size and shape characterization of irregular coal micro-particle: Validation with digital inline holography,” *Journal of Quantitative Spectroscopy and Radiative Transfer*, vol. 241, p. 106728, Jan. 2020. [Online]. Available: <https://doi.org/10.1016/j.jqsrt.2019.106728>
- [77] L. Ouldarbi, M. Talbi, S. Coëtmellec, D. Lebrun, G. Gréhan, G. Perret, and M. Brunel, “3D-shape recognition and size measurement of irregular rough particles using multi-views interferometric out-of-focus imaging,” *Applied Optics*, vol. 55, no. 32, p. 9154, 2016.
- [78] G. König, K. Anders, and A. Frohn, “A new light-scattering technique to measure the diameter of periodically generated moving droplets,” *Journal of Aerosol Science*, vol. 17, no. 2, pp. 157–167, Jan. 1986.
- [79] Y. Hardalupas, S. Sahu, A. M. Taylor, and K. Zarogoulidis, “Simultaneous planar measurement of droplet velocity and size with gas phase velocities in a spray by combined ilids and piv techniques,” *Experiments in fluids*, vol. 49, no. 2, pp. 417–434, 2010.
- [80] S. Talebi-Moghaddam, F. Bauer, F. Huber, S. Will, and K. Daun, “Inferring soot morphology through multi-angle light scattering using an artificial neural network,” *Journal of Quantitative Spectroscopy and Radiative Transfer*, vol. 251, p. 106957, Aug. 2020. [Online]. Available: <https://linkinghub.elsevier.com/retrieve/pii/S002240731930809X>
- [81] H. Oltmann, J. Reimann, and S. Will, “Single-shot measurement of soot aggregate sizes by wide-angle light scattering (WALS),” *Applied Physics B*, vol. 106, no. 1, pp. 171–183, Jan.

2012. [Online]. Available: <http://link.springer.com/10.1007/s00340-011-4781-z>
- [82] F. J. Huber, S. Will, and K. J. Daun, “Sizing aerosolized fractal nanoparticle aggregates through Bayesian analysis of wide-angle light scattering (WALS) data,” *Journal of Quantitative Spectroscopy and Radiative Transfer*, vol. 184, pp. 27–39, Nov. 2016. [Online]. Available: <http://dx.doi.org/10.1016/j.jqsrt.2016.06.030>
- [83] Z. Ulanowski, Z. Wang, P. H. Kaye, and I. K. Ludlow, “Application of neural networks to the inverse light scattering problem for spheres,” *Applied Optics*, vol. 37, no. 18, p. 4027, Jun. 1998. [Online]. Available: <https://www.osapublishing.org/abstract.cfm?URI=ao-37-18-4027>
- [84] V. V. Berdnik and V. A. Loiko, “Retrieval of size and refractive index of spherical particles by multiangle light scattering: neural network method application,” *Applied Optics*, vol. 48, no. 32, p. 6178, Nov. 2009. [Online]. Available: <https://www.osapublishing.org/abstract.cfm?URI=ao-48-32-6178>
- [85] A. Yevick, M. Hannel, and D. G. Grier, “Machine-learning approach to holographic particle characterization,” *Optics Express*, vol. 22, no. 22, p. 26884, Nov. 2014. [Online]. Available: <https://www.osapublishing.org/oe/abstract.cfm?uri=oe-22-22-26884>
- [86] J. J. Rudiger, K. Book, B. Baker, J. S. DeGrassie, and S. Hammel, “A machine learning approach for predicting atmospheric aerosol size distributions,” in *Laser Communication and Propagation through the Atmosphere and Oceans VI*, A. M. van Eijk, S. M. Hammel, and J. P. Bos, Eds., no. September 2017. SPIE, Sep. 2017, p. 26.
- [87] L. M. Gugliotta, G. S. Stegmayer, L. A. Clementi, V. D. G. Gonzalez, R. J. Minari, J. R. Leiza, and J. R. Vega, “A Neural Network Model for Estimating the Particle Size Distribution of Dilute Latex from Multiangle Dynamic Light Scattering Measurements,” *Particle & Particle Systems Characterization*, vol. 26, no. 1-2, pp. 41–52, Apr. 2009. [Online]. Available: <http://doi.wiley.com/10.1002/ppsc.200800010>
- [88] M. T. Hagan, H. B. Demuth, M. H. Beale, and O. De Jesús, *Neural Network Design*, 2nd ed.
- [89] J. Li, S. Shao, and J. Hong, “Machine learning shadowgraph for particle size and shape characterization,” *Measurement Science and Technology*, vol. 32, no. 1, p. 015406, Jan. 2021. [Online]. Available: <https://iopscience.iop.org/article/10.1088/1361-6501/abae90>
- [90] Y. Fu and Y. Liu, “Bubgan: Bubble generative adversarial networks for synthesizing realistic bubbly flow images,” *Chemical Engineering Science*, vol. 204, pp. 35–47, 2019.
- [91] J. Schäfer, P. Schmitt, M. W. Hlawitschka, and H. Bart, “Measuring Particle Size Distributions in Multiphase Flows Using a Convolutional Neural Network,” *Chemie Ingenieur Technik*, vol. 91, no. 11, pp. 1688–1695, Nov. 2019. [Online]. Available: <https://onlinelibrary.wiley.com/doi/10.1002/cite.201900099>

- [92] P. Ghamisi, Y. Chen, and X. X. Zhu, “A Self-Improving Convolution Neural Network for the Classification of Hyperspectral Data,” *IEEE Geoscience and Remote Sensing Letters*, vol. 13, no. 10, pp. 1537–1541, 2016.

3. Non-spherical particle size estimation using supervised machine learning

The contents of this chapter have been published in *Applied Optics* (C. Y. Moon, A. Gargiulo, G. Byun, and K. T. Lowe, "Non-spherical particle size estimation using supervised machine learning," *Appl. Opt.* 59, 3237–3245 (2020). doi:10.1364/AO.385750.

The accepted manuscript version has been included with permission from The Optical Society.

Non-spherical particle size estimation using supervised machine learning

CHI YOUNG MOON^{1*}, ALDO GARGIULO¹, GWIBO BYUN¹, AND K. TODD LOWE¹

¹Kevin T. Crofton Department of Aerospace and Ocean Engineering, Virginia Tech, Blacksburg, VA, 20036

*Corresponding author: chimoon@vt.edu

Compiled February 28, 2020

The inverse scattering problem of non-spherical particle size estimation is solved using a series of supervised machine learning models trained on a library of light scattering data. By establishing a large library with spheres and spheroids as fundamental shapes, and through optimization of model hyperparameters, the trained models are able to accurately estimate a precise equivalent volume sphere radius of particles from an external database and simulations, with root mean square errors of 2.6% and 1.9% for the external and simulated particles, respectively. It was found that classification via a k-nearest neighbor model and refinement via a trained ensemble regression model performed best for equivalent volume measurements.

© 2020 Optical Society of America

<http://dx.doi.org/10.1364/ao.XX.XXXXXX>

1. INTRODUCTION

Particle sizing is an important problem with a long history, due to its broad utility ranging from atmospheric to biomedical sciences. While many approaches are available, methods utilizing the light scattering and extinction from particles are popular, due to its non-intrusive nature and relative ease in implementation. The so-called inverse problem of measuring light scattering and extinction and retrieving particle has been a research topic for decades [1–6].

With this history, some topics, such as sizing a dispersion of spherical particles, are mature enough to be commercialized. However, as most particles in practice are not spherical, these assumptions place limitations on the use and validity of these techniques. Non-spherical particle sizing is an active research area, with many early efforts focused on analytically solving the inverse problem [7–10].

Machine learning (or statistical learning) allows modeling of complex systems without necessarily having an analytic solution to the problem [11]. This approach is useful when there might not be a fundamental physical relation for modeling purposes [12–14], or the physical model is very complex, such as non-spherical particle size retrieval. Since the direct problem of calculating scattering parameters of known particles is much easier than solving the inverse, a large data set of scattering parameters can be generated and used for training machine learning models. Scattering observations of unknown particles can then be entered as the input for the trained models, and its output would be an estimation of the parameters based on the training data.

While initial concepts utilizing neural networks for particle

size estimation have been proposed in the past, many are limited by requiring a wide (if not the full) angular range for scattering observations, and by being limited in shape (spherical) and size [15–20]. As the full scattering profile is rarely available for remote sensing, these applications lack practicality.

A machine learning-based non-spherical particle sizing method using intensity data at three distinct angular positions as features is presented. A pre-established database of light scattering data is used to train a series of supervised machine learning classifier and regression models. The trained models are able to solve the inverse scattering problem using five features based on only three distinct observations. This novel technique is then demonstrated by estimating the equivalent volume sphere radius of particles found in an external scattering database, as well as simulated non-spherical particles.

2. METHODS

A schematic of the overall process is shown in Fig. 1. Particle scattering data is first generated using numerical tools then organized into a library. Layers of classification and regression models are trained using the scattering library for particle size estimation. Scattering features from the target particles are used as inputs to the trained models, which then estimates the particle size. Details of each step described are presented in the following sections.

A. The Light Scattering Library

A library containing scattering profiles for particles in the range of interest (chosen by the user) is generated and used as the training data for the supervised machine learning models. The

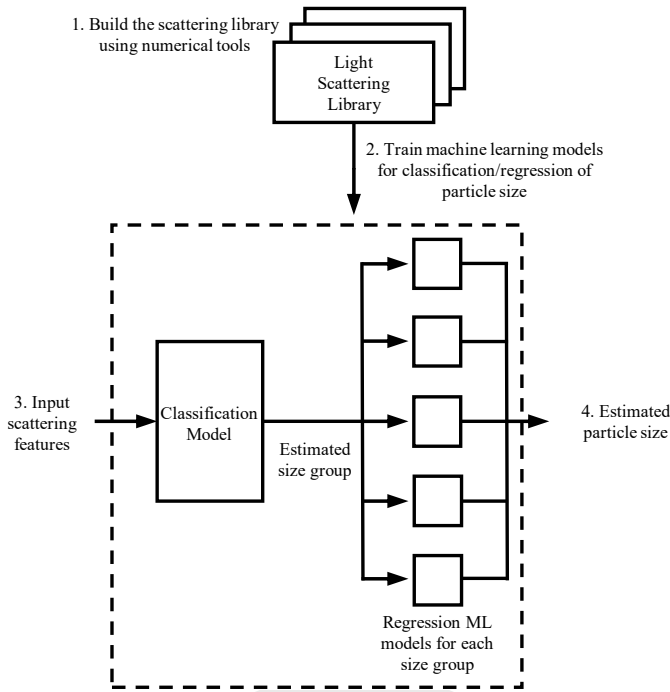


Fig. 1. Overall process scattering library population, machine learning model training, and particle size estimation.

entries in the database vary in a wide range of parameters: shape, size, and material properties (represented by its refractive index). While the overall library is proposed to include several fundamental shapes, such as spheres, spheroids, cubes, and prisms, the current work will focus on the generation and usage of spherical and spheroidal particles. The method for generating the scattering profiles vary depending upon the shape and size of the particle. The non-dimensional size parameter,

$$x = \frac{2\pi r}{\lambda} \quad (1)$$

where λ is the wavelength of incident light and r is the characteristics length of the particle is used to determine what regime particle scattering (and method used to generate its profile) takes place. For spherical particles, the characteristics length is simply the particle radius. For non-spherical particles, equivalent volume sphere radius, or its effective radius is used to calculate its size parameter.

Geometric optics approximation is considered to be sufficient at capturing the scattering phenomena when the particle is much larger than the wavelength of the incident light ($x \geq 10$) [21–23]. Developed by Macke et al., a FORTRAN based geometric optics code suite was used to populate the large spherical and spheroidal entries in the library [23]. Originally developed for atmospheric research purposes, this code package introduces a number of rays as the incident plane wave, which are traced through the input particle geometry using Snell's law and Fresnel's equations. A number of internal reflections are allowed before the escaping rays are sampled in angular bins for quantifying the particle scattering. This program also features averaging out random orientations for non-spherical particles.

For smaller particles ($x \approx 1$), exact methods are available, depending on particle shape. Mie theory is used for determining scattering by spheres [22], while the T-matrix method is used for spheroids [24]. Both Mie theory and the T-matrix method

can extend beyond the shapes mentioned above and would be useful for extending the library in the future. While the methods provide exact solutions for their respective shapes, a limit for numerical convergence is imposed by the particle size. MatScat, a MATLAB program developed by Schäfer [25, 26] was used to populate the smaller spherical entries in the library. For smaller spheroids, SMARTIES, a MATLAB program by Somerville et al. [24] was used for generating particle scattering parameters for the library. A threshold of $x \approx 40$ was used for the transition point between the small particles (using Mie theory and the T-matrix method) and the large particles (using geometric optics). Combining the entries for both shapes, the library contains the following representative features of light scattering: scattering intensity, phase function for different polarization of incident light, differential scattering cross section, extinction coefficient, and extinction cross-section. While only the scattering intensity is currently used as the training feature, further development of the method by including some of the other features is expected to improve this technique.

Using all three codes discussed above, the light scattering library was generated for ranges of varying particle parameters: refractive index, aspect ratio, and size parameter. Table 1 shows the ranges of particle parameters for the scattering library. 50 entries linearly spaced were used to fill out the radius range. All calculations were performed with the incident light's wavelength fixed at 532 nm. Aspect ratios of 0.5, 1, 1.5, 2 and 3 were used to cover the range of shapes, with spheres and spheroids as listed below. For refractive index, entries with values of 1.3, 1.4, 1.5, 1.6, and 1.7 were generated. With these variations, a total of 1,250 entries were generated to form the light scattering library. However, only entries with refractive index $n = 1.5$ were used since the vast majority of the test particles had refractive indices in this range and to reduce the model training computational time.

Table 1. Ranges of Parameters for the Light Scattering Library

Parameter	Range
Equivalent volume sphere radius (r)	1 μm - 25 μm
Size parameter (x)	6 - 300
Aspect ratio (AR)	0.5 - 3
Refractive index (n)	1.3 - 1.7

B. Machine Learning Surrogate Models

The library contains data sets linking a particle's scattering patterns to its predefined characteristics, e.g. particle type, shape, and size. A particle's size can be estimated if the scattering observation matches with an entry within the library. However, this is only possible if that measured scattering profile is specifically contained and labeled within the library. It is not feasible to extend the library to match all scattering profiles one might encounter, since particles in actuality have infinitely complex shapes (and therefore infinitely complex scattering profiles), and it is impossible to know what type of particles may be encountered *a priori*. To address this dilemma, a surrogate model is used to predict the outcome.

Using the scattering library, such surrogate models can be established to link measured scattering profiles to specific parti-

cles. One way of utilizing labeled data to infer an appropriate surrogate model, which not only fits that data set but also predicts and labels newly observed unlabeled data, is supervised machine learning [11, 27]. Supervised machine learning represents the task of inferring a model or a function that maps an input to an output based on labeled example input-output pairs, often referred to as training data. The obtained model can then be used to map unforeseen test observations as input to the desired output. The scattering library acts as a labeled training data set to train a surrogate model using supervised machine learning, which characterizes newly observed particles based on their measured light scattering profiles.

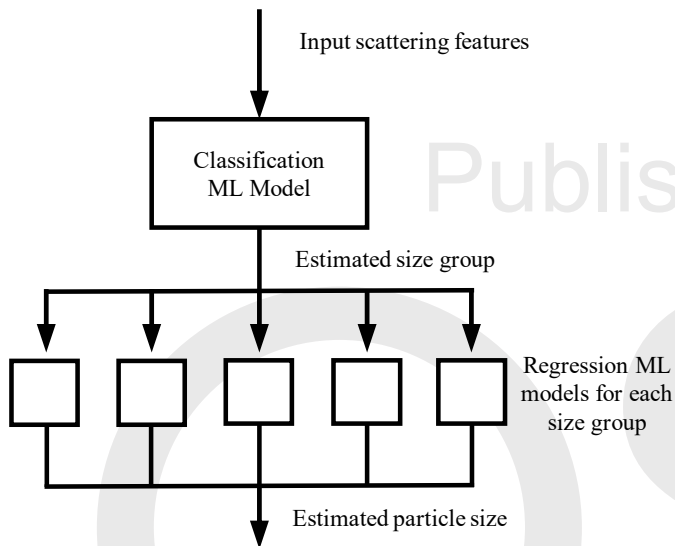


Fig. 2. The classification and regression layers for particle size estimation.

In the present approach, both classification and regression models are used for sizing particles. Classification methods have qualitative outcome variables, as opposed to regression methods, which have quantitative outcome variables [11, 28]. The classification models are first trained on groups of similarly sized particle data, which determine what group (and therefore the particle's size range) the input particle belongs to. This classification process is also used to filter down the library data to particles only in the size range estimated. The remaining filtered data is used to train a regression model, which precisely estimates the size of the input particle. Originally, a single classification layer was used to classify particles. However, the training accuracy decreased as the library increased in size and complexity, which inspired the current approach with classification and regression layers, where the training data reduces based on the previous step's output.

In the scattering library, the non-dimensional size parameter ranges from 5 to 300, as shown by Table 1. The 50 linearly spaced entries were divided up to various numbers of size groups or N for their impact on the estimation. From 2 groups (where the library is divided into smaller and larger halves), to 25 groups (where each group consists of two size parameters) were used to train the various classifier models.

The scattering profiles as a function of the scattering angle form the basis for the machine learning model inputs. Three intensity values on the scattering profile (at 5, 10, and 30 degrees) were used to form distinct inputs. These forward scatter angles

have been shown to be highly sensitive to particle size, while the side scatter at 30 degrees, which shows a relatively low sensitivity to size, is used to normalize these intensities [21]. The scattering angle used for the input feature is important to the model's ability to accurately sort or estimate particles by size, as this sensitivity is what allows the machine learning models to create feature maps that are more distinguishable as the size parameter changes. The first two features were the intensity ratios from the forward points (5 and 10 degrees) to the intensity at 30 degrees. The intensity ratios as the input feature allows for a simpler practical application. Any discrepancy between equipment, such as the incident laser intensity, detector/camera properties from test to test is negated by using a ratio of intensities. The three additional features were the absolute difference in intensity from a reference particle. This means that the difference in intensity at each angle were calculated independently for the training data (a scattering profile from the library database) as well as the inputs for estimation using an experimental scattering profile of the same particle, a spherical water droplet with a refractive index of $m = 1.3$ and size of $r = 1.1 \mu\text{m}$ [29].

Table 2. Input/Training Features for the Machine Learning Models.

Name	Formulation
Intensity Ratio 1	$IR_1 = \frac{I(\theta_1=5^\circ)}{I(\theta_3=30^\circ)}$
Intensity Ratio 2	$IR_2 = \frac{I(\theta_2=10^\circ)}{I(\theta_3=30^\circ)}$
Absolute Intensity Shift 1	$AIS_1 = I(\theta_1 = 5^\circ) - I_{ref}(\theta_1 = 5^\circ) $
Absolute Intensity Shift 2	$AIS_2 = I(\theta_2 = 10^\circ) - I_{ref}(\theta_2 = 10^\circ) $
Absolute Intensity Shift 3	$AIS_3 = I(\theta_3 = 30^\circ) - I_{ref}(\theta_3 = 30^\circ) $

Both the classification and regression models were trained and optimized based on cross-validation accuracy. Optimization of model parameters or hyperparameters, are performed to tune the models for optimal performance facing random inputs outside of the training data. Cross-validation is a statistical method to estimate model performance by training a model on only a subset of the data and using the remainder as test inputs [11, 28]. Since the training data contain the labeled outputs, the correct outputs for the withheld data used as test inputs are known, thus the model can be assessed on its performance. K-fold cross-validation is a common method for cross-validating statistical learning models. The training data are divided into k number of subsets or folds. $(k - 1)$ folds are used to train the data, while the k^{th} fold is used as the test/validation data.

For hyperparameter optimization, a Bayesian optimization process using MATLAB was performed to iterate on model training for the cross-validation results using $k = 10$, a commonly recognized value that balances error in both bias and variance [11, 27, 28]. Cross-validation on classification models results in a model accuracy score, or how well the model classified the k^{th} test data. Similarly, cross-validation on regression models is scored by the root mean square (RMS) error, from the difference between the test data to the model output. The optimization algorithm trains a model, estimates performance using cross-validation, and iterates to tune its hyper-parameters to achieve maximum accuracy or minimum RMS error, for classification and regression models, respectively. Models for each variation listed in this section went through 100 iterations for this opti-

mization process.

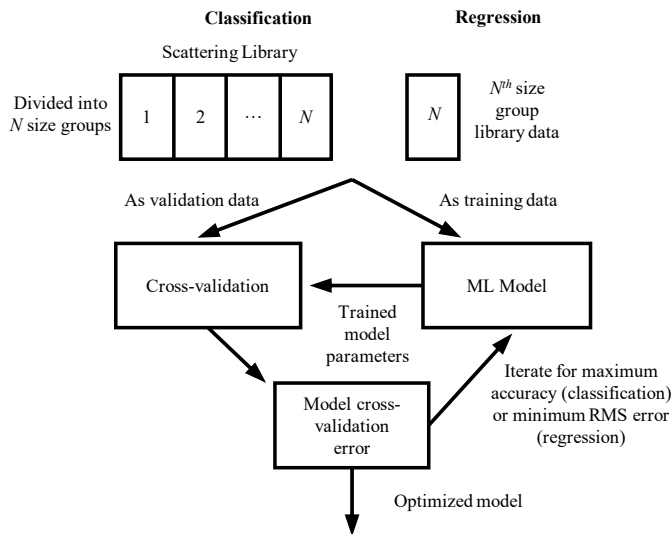


Fig. 3. Classification and regression model training and optimization procedure.

Four different methods each were used for both the classification and regression model building. Decision trees (DT), linear support vector machines (SVM), k-nearest neighbor (KNN), and ensemble methods were used for classification. Ensemble methods use a large number of weaker models, such as decision trees to boost its performance. For regression models, DT, SVM, ensemble methods, as well as linear regression were used. The detail workings of each method will not be given in this work, but can be found in the cited references [11, 27, 28].

An external scattering database of ash, sand, and minerals was used to test the trained models. The Amsterdam and Grenada (A&G) Light Scattering Database [30] contains experimental scattering matrices of a wide range of irregular particles, from various origins and composition. In addition, scanning electron microscope (SEM) images of the particles, equivalent volume sphere radius, approximate size distribution, refractive index, and composition are available as reference. The equivalent volume sphere radius, wavelength of light used, as well as the resulting size parameter for the particles tested are listed in Table 3. The listed particle size is acquired from Fritsch Analysette A22 and Malvern Instruments Mastersizer 2000 particle sizers. These devices use Fraunhofer diffraction or Mie theory to estimate a size distribution using a spherical assumption. While these particles are highly irregular in shape (as visible through the microscope images), testing the wide range of particles in this database is valuable as a step in validating the presented method, as it provides data from real particle samples. The test particles are divided into 3 categories: volcanic ash, cosmic dust analogs, and miscellaneous. Volcanic ash particles are named after the volcanoes producing them, while the cosmic dust analogs are mostly volcanic ash processed to match dust samples from the Lunar (JSC-1A) and the Martian (JSC0, JSC200) surfaces [31, 32]. The reference water droplet, used to calculate the absolute difference in intensity at the three observation points for the test input, is also listed in Table 3. In practical applications, the user may use calibrated materials such as polystyrene latex spheres as the reference particle. While the wavelengths used in these experiments do not match to the value used to generate the library entries, since the size parameter takes both

diameter and wavelength into account, the estimation can be done by classifying and regressing for the size parameter, then converting to the particle size using its incident wavelength. The estimation shown in the results section will be converted from the size parameter output to its corresponding radius, using Eq. 1. The baseline model was trained with the complete library (all aspect ratios, $m = 1.5$), and additional test cases were run with a segmented library as the training set, investigating the impact of the library size and the complexity of the shapes included.

Table 3. Test Particles from the A&G Light Scattering Database. The reference water droplet used to calculate the absolute intensity shifts is indicated by an asterisk.

Name	Effective Radius (μm)	Wavelength (nm)	Size Parameter
Volcanic Ash			
Eyjafjallajökull[33]	7.8	647	75.8
St. Helens[34]	4.1	633	40.7
Lokon[35]	7.1	442	100.9
Pinatubo[35, 36]	3.0	442	42.7
Puyuhue[33]	8.6	647	83.5
Spurr[34]	14.4	633	142.9
Cosmic Dust Analogs			
JSC0[31]	15.9	488	204.1
JSC-1A[32]	29.5	647	286.5
JSC200[31]	28.1	647	272.9
Miscellaneous			
Fly Ash[37]	3.7	442	51.9
Basalt[31]	6.9	647	67.0
Calcite[31, 38]	3.3	448	46.3
Loess[35]	3.9	442	55.4
Quartz[35]	2.3	442	32.7
Sahara Sand[35]	8.2	442	116.6
Water Droplet*[29]	1.1	442	15.6

For further validation, particle scattering of differing size, shape, and distribution was simulated and used as inputs for the trained models. Three spheroids as monodisperse particles were simulated for testing are shown in Fig. 4. The size and shape of the spheroids were chosen to cover a wide range of possible particles and to ensure that the simulated particles do not match with any other entry in the scattering library. The geometric parameters of the simulated spheroids can be found in Table 4.

A polydisperse distribution of particles was also simulated for additional validation. A log-normal size distribution was used to generate and simulate the particle light scattering. The log-normal distribution is defined in Eq. 2 and is defined by two

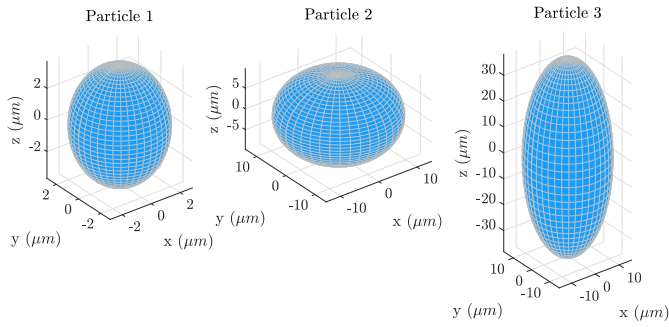


Fig. 4. Particles used for validation of monodisperse spheroid sizing, corresponding to the parameters in Table 4.

Table 4. Simulated particle parameters for mono and polydisperse validation tests.

Monodisperse			
Particle #	Aspect Ratio	Refractive Index	Equivalent Volume Sphere Radius (μm)
1	1.3	1.5	3.1
2	0.7	1.5	12.3
3	2.5	1.5	20.7
Polydisperse			
	μ	σ	r_{eff} (μm)
	0.1	1.0	13.5

parameters, μ and σ .

$$n(r) = \frac{1}{r\sigma\sqrt{2\pi}} \exp\left(-\frac{(\ln r - \mu)^2}{2\sigma^2}\right) \quad (2)$$

An effective radius of the distribution is defined in Eq. 3.

$$r_{eff} = \frac{\int_0^\infty r^3 n(r) dr}{\int_0^\infty r^2 n(r) dr} \quad (3)$$

This effective radius is similarly how the A&G database characterized its measured size distribution. The parameters used to generate the simulated distribution, as well as its effective radius, are listed in Table 4. Using the listed values of μ and σ , the resulting number and volume density distribution functions are shown in Fig. 5.

3. RESULTS

The cross-validation accuracy and errors from the classification and regression models are presented to demonstrate the process of narrowing down the number of size groups used to divide up the library, as well as the choice of classification and regression models. The particle size estimation results from models trained with the full library using the Amsterdam and Grenada database, as well as several simulated particles is intended to provide a clear demonstration of the method's capabilities. In addition, the impact of the scattering library size and complexity used to train the models on the method accuracy is shown.

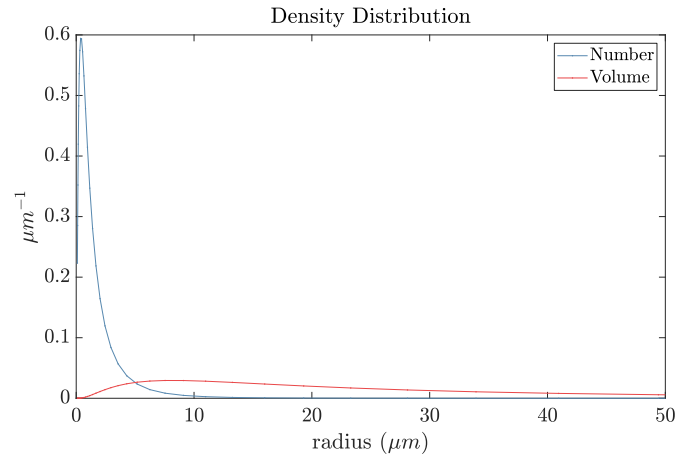


Fig. 5. The number and volume density distribution functions for the simulated particle distribution.

A. Hyperparameter Optimization

The optimized models from the process detailed in the previous section were assessed for both their final cross-validation accuracy and performance when sizing the A&G particles. Figure 6 shows the cross-validation error (or $1 - \text{Accuracy}$) for the variations in the number of size groups (N) used to divide the library data set used to train them as well as the four classification models: ensemble (ENS), linear support vector machine (LSVM), k-nearest neighbor (KNN), and decision tree (DT). As expected, fewer groups used to divide up the library results in better cross-validation performance. With $N = 2$, the classifier models are only tasked with determining whether the input particle belongs in the smaller or larger halves of the data set. As N increases, the classification task is more difficult by having fewer data points in each group for training and smaller size range that makes up each interval.

For the regression model training cross-validation, as the library is divided into N number of groups, each size group has its own regression model and accompanying cross-validation RMS error. As the number of size groups used to divide up the library for training varies, the cross-validation errors of the models across the size groups can be averaged as an indication of regression model performance. This mean cross-validation error ϵ_N is defined as:

$$\epsilon_N = \frac{1}{N} \sum_{i=1}^{i=N} \epsilon_i \quad (4)$$

where ϵ_i is the cross-validation RMS error from the regression model at each size group and N is the number of size groups used to divide the library. When looking at the mean cross-validation error as shown on Fig. 7, as fewer groups are used to divide up the library, the cross-validation error is increased. With increased number of groups (and therefore smaller size groups), Fig. 7 shows that the regression models have a lower cross-validation error, showing an opposite behavior from the classification models.

For determining an optimal N , a balanced approach was used for considering both the classification and regression models, as well as the fact that the classification algorithm must first place the input data in the correct interval for the regression model to estimate the particle size well. By looking at the overall performance of the model for sizing the particles from the

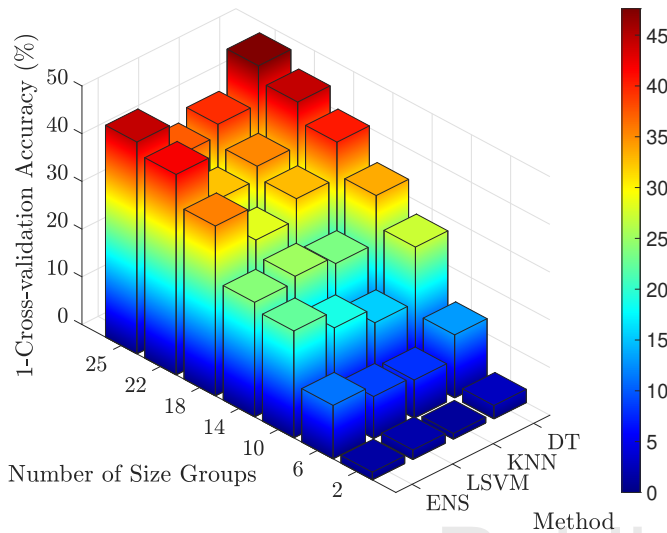


Fig. 6. Cross-validation error for the optimized classification models for various numbers of size groups and classification methods: ensemble (ENS), linear support vector machine (LSVM), k-nearest neighbor (KNN), and decision trees (DT).

A&G database, a combination of using KNN classifier, ensemble regression model, and $N = 10$ size groups produced the minimum RMS relative error. Correspondingly, the KNN classifier and ensemble regression model is shown to have the best cross-validation performance against the other methods. While the cross-validation performance supports the actual performance of the model, it did not correlate for variations in the number of groups used.

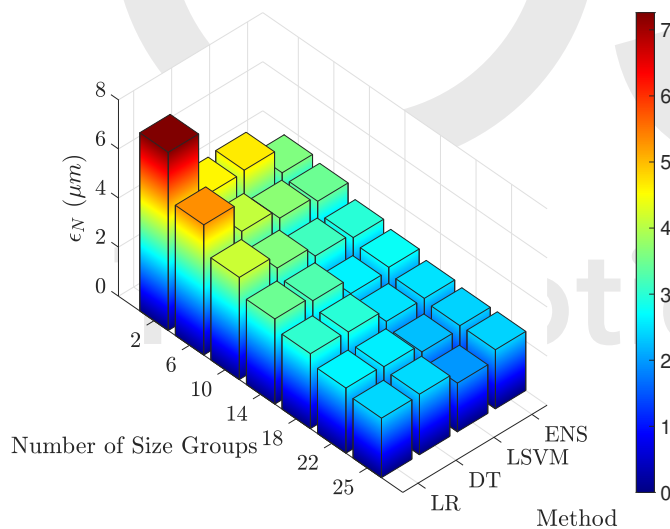


Fig. 7. Mean cross-validation RMS error for the optimized regression models for various numbers of size groups and regression methods: linear regression (LR), decision trees (DT), linear support vector machine (LSVM), and ensemble (ENS).

B. Classification and Regression Results

A combination of KNN classifier, ensemble regression model, and $N = 10$ was found to have the minimum RMS error of 2.6% when sizing the A&G particles. The resulting

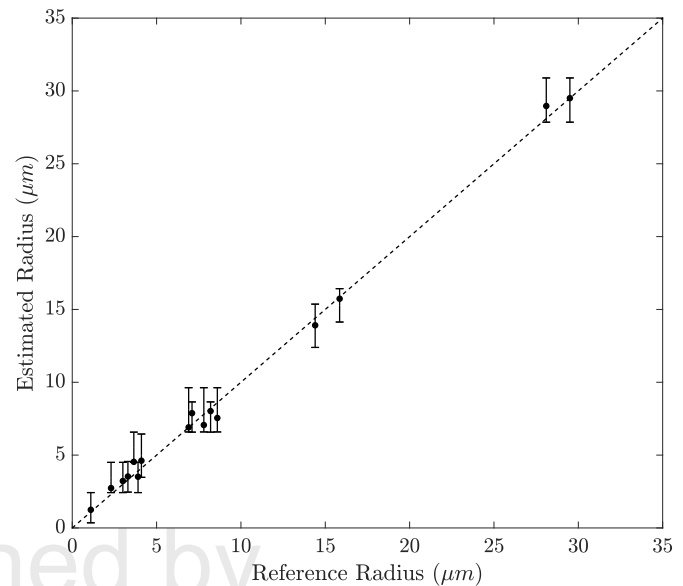


Fig. 8. Particle size range and radius estimation using machine learning models. The interval represents the estimated range by the classification model, while the solid dot represents the precise estimation from the regression model.

classification intervals, precise estimation from the regression models, as well as the reference value from the A&G database are listed in Table 5. For the KNN classifier's hyperparameters, the number of neighbors (k) was optimized to 12, the distance metric to Mahalanobis, with an inverse distance weight applied. For the regression models for each size group, while the specific hyperparameters varied, a common factor seen throughout was the boosting algorithm, which was optimized to be LSBoost.

The classification model performed excellently, failing to place the inputs in the correct interval only twice (for quartz and fly ash). In both cases, the classification models overestimated the size range, but the regression model for the fly ash particle attempted to compensate by estimating the lower limit of the size group. A visual representation of the model's performance is shown in Fig. 8. The estimation results do not show a bias in accuracy with regards to particle size.

C. Simulated Particles

The same optimal combination of group number, classification/regression models was evaluated for the simulated particles. These simulated particles capture the full effect of the non-spherical shapes, as the A&G particles did. However, the reference radius used for establishing the method's effectiveness were measured particle sizers that use the spherical assumption. Testing the presented method using simulated particles allows comparison to the true particle size and demonstrate the ability to size non-spherical particles. For the monodisperse particle estimation, the true as well as the estimated radius for each particle is listed in Table 6. The classification model first correctly placed the inputs in the correct size groups, and the regression model converged to values that led to excellent agreement between the estimated and true particle size. The relative errors across the three particles had a RMS value of 1.9%.

For the simulated distribution of particles, the classification model once again placed the input into the correct size group. The regression model then converged to a size estimation close

Table 5. Estimated particle size range and radius as well as the reference radius for the tested A&G particles.

Name	Classification Range (μm)	Regression Estimation (μm)	Reference Radius (μm)
Volcanic Ash			
Eyafjallajökull	6.6-9.6	7.1	7.8
St. Helens	3.5-6.4	4.6	4.1
Lokon	6.6-8.7	7.9	7.1
Pinatubo	2.4-4.5	3.2	3.0
Puyuhue	6.6-9.6	7.5	8.6
Spurr	12.4-15.4	13.9	14.4
Cosmic Dust Analogs			
JSC0	14.1-16.4	15.7	15.9
JSC-1A	27.9-30.9	29.5	29.5
JSC200	27.9-30.9	29	28.1
Miscellaneous			
Fly Ash	4.5-6.6	4.5	3.7
Basalt	6.6-9.6	6.9	6.9
Calcite	2.5-4.6	3.5	3.3
Loess	2.4-4.5	3.5	3.9
Quartz	2.4-4.5	2.7	2.3
Sahara Sand	6.6-8.7	8	8.2
Water Droplet*	0.35-2.4	1.2	1.1

Table 6. The estimation results from the simulated particles.

Monodisperse			
Particle #	Classification Range (μm)	Regression Estimation (μm)	Reference Radius (μm)
1	2.9-5.4	3.1	3.1
2	10.4-12.9	12.4	12.3
3	20.4-22.9	21.1	20.7
Polydisperse			
	Classification Range (μm)	Regression Estimation (μm)	Reference Radius (μm)
	12.4-15.6	13.1	13.5

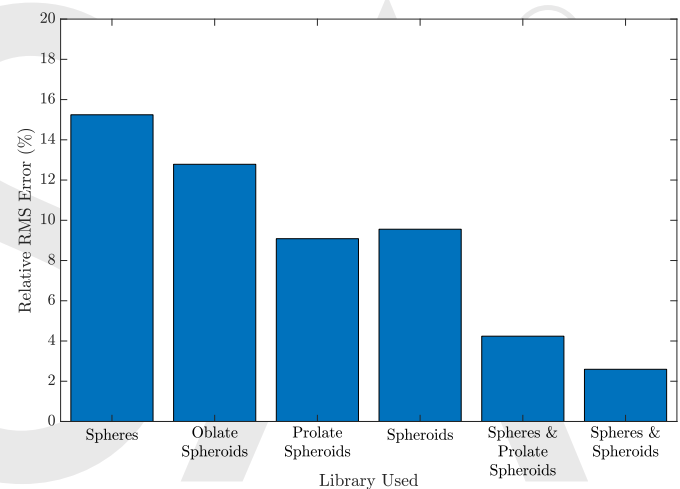
to the true value, with a relative error of 3.0%.

D. Impact of Library Size and Complexity

With the baseline model's performance established, the results from test cases using a limited subset of the library for model training are shown in Fig. 9. The number of size groups used

as well as the classification and regression methods were kept constant from the baseline case using the sphere and spheroid library, whose results were shown in the previous section. With the data set segregated by the particle shape (the aspect ratio), the libraries used to train the models vary in shape (from spheres to spheroids) and in size (e.g., more entries are in the spheroid case than the spheres only). Figure 9 shows that as the training library gets larger and more complex in shape, the relative RMS error for particle size estimation decreases. This is consistent with expected behavior, as the test particles are highly irregular in shape [30]. The models are trained with larger data set containing more particle shapes, demonstrating the benefits of generating a large library.

Current limitations on this method are based on the particles present in the library for model training. The A&G database contains relatively small particles (tested in the present work) and very large particles with characteristic lengths greater than 1 mm. Validation demonstrated by the simulated particle tests are also limited to the size range present in the scattering library. As discussed in this section, expanding the library with a wider size range and more complex shapes is hypothesized to both expand the accuracy and capabilities of this method.

**Fig. 9. Effect of different shapes in the scattering library on the relative RMS error on particle radius estimation.**

4. CONCLUSION

A new method for estimating non-spherical particle size was detailed and demonstrated. Trained on a pre-established database of particle light scattering, the supervised machine learning models first classify the approximate size range, then estimate a precise radius using classifier and regression models, respectively. Testing this method using an external collection of particle scattering profiles, the trained models were able to accurately estimate the particle radius, with relative RMS error low as 2.6% across 16 different particle samples varying in size, shape and composition.

This accuracy is significant as the tested particles are irregular in shape and surface, but the machine learning models accurately size them only using a library consisting only of spheres and spheroids. Multiple factors are believed to have contributed to this performance. One is that for most sand and volcanic ash particles, while their surfaces are highly irregular, their aspect ratio values are within our library's scope (<2) [39, 40]. The

library for non-spherical entries as well as the test particles from the A&G database are generated and measured as randomly oriented particles. In addition, spheroids have been found to be acceptable as modeling shapes for volcanic ash [33]. For particles such as ice crystals, whose structures are even more irregular than sand or ash and not represented in the library adequately, additional work would be required for finding a good representative shape and incorporating them into the library and the models.

The current implementation of the method is limited by the parameter ranges in the scattering library. However, the method could be applied for a wider size range and additional shapes as opposed to some of others referenced in the introduction. For larger particles, as long as new library entries covering that size range are added, new models can be trained to accommodate this capability. A similar approach could be taken for classifying shapes. For example, if this technique were to be applied to remote sensing of ice crystals, some library entries with basic crystalline shapes could be added. Based on the presented results, an increase in estimation accuracy would be expected.

As this is the first implementation of this method, numerous improvements are envisioned. Since particles in practice are composed of a distribution, not a single size, the ability to estimate the mean radius is just the first step. The next step in the method's development would be to retrieve another parameter that can define the size distribution, such as the effective variance.

The current structure of separate classification and regression layers could be envisioned as a single neural network, with one or several hidden layers that can perform as the size group classifier or individual regression models. This would be a worthwhile investigation in the future as it could reduce the complexity and training time necessary to train and implement multiple layers and models.

The angular locations as well as the number of scattering features used as the input feature warrant further investigation in future work. While the current angles used for features were determined empirically based upon known size sensitivity in the forward scattering region, further optimization based on the input scattering angles should be considered. In addition, the intensity difference as inputs require a common particle to serve as the reference. Testing the A&G particles, a water droplet with a well-known shape, refractive index, and size was available. However, as this technique advances, input features only based on normalization would eliminate the need for such calibration. Combined with the number and location of the intensity inputs, such optimization is imagined for future endeavours.

Funding.

Rolls-Royce North American Technologies, Inc.

Acknowledgements.

The authors are grateful to Prof. Lin Ma for his contributions to the early stages of this work.

Disclosures.

The authors declare no conflicts of interest.

REFERENCES

- G. Yamamoto and M. Tanaka, "Determination of Aerosol Size Distribution from Spectral Attenuation Measurements," *Appl. Opt.* **8**, 447 (1969).
- M. D. King, D. M. Byrne, B. M. Herman, and J. A. Reagan, "Aerosol Size Distributions Obtained by Inversions of Spectral Optical Depth Measurements," *J. Atmospheric Sci.* **35**, 2153–2167 (1978).
- G. Ramachandran and D. Leith, "Extraction of aerosol-size distributions from multispectral light extinction data," *Aerosol Sci. Technol.* **17**, 303–325 (1992).
- G. P. Box, K. M. Sealey, and M. A. Box, "Inversion of Mie Extinction Measurements Using Analytic Eigenfunction Theory," *J. Atmospheric Sci.* **49**, 2074–2081 (1992).
- L. Wang, X. Sun, K. Sun, and F. Li, "Retrieval of particle size distribution in multispectral region," in *International Conference on Optical Instruments and Technology: Optoelectronic Measurement Technology and Systems*, (2011), November 2011, p. 82012H.
- L. Ma and R. K. Hanson, "Measurement of aerosol size distribution functions by wavelength-multiplexed laser extinction," *Appl. Phys. B: Lasers Opt.* **81**, 567–576 (2005).
- J.-Q. Zhao, F. Zhang, and J. Li, "Analytical inversion of the absorption spectrum to determine non-spherical particle size distribution," *J. Quant. Spectrosc. Radiat. Transf.* **149**, 128–137 (2014).
- X. Sun, H. Tang, and G. Yuan, "Anomalous diffraction approximation method for retrieval of spherical and spheroidal particle size distributions in total light scattering," *J. Quant. Spectrosc. Radiat. Transf.* **109**, 89–106 (2008).
- Y. Liu, W. P. Arnott, and J. Hallett, "Particle size distribution retrieval from multispectral optical depth: Influences of particle nonsphericity and refractive index," *J. Geophys. Res. Atmospheres* **104**, 31753–31762 (1999).
- M. I. Mishchenko, A. A. Lacis, B. E. Carlson, and L. D. Travis, "Nonsphericity of dust-like tropospheric aerosols: Implications for aerosol remote sensing and climate modeling," *Geophys. Res. Lett.* **22**, 1077–1080 (1995).
- G. James, D. Witten, T. Hastie, and R. Tibshirani, *An Introduction to Statistical Learning*, vol. 103 of *Springer Texts in Statistics* (Springer New York, New York, NY, 2013).
- A. E. Maxwell, T. A. Warner, and F. Fang, "Implementation of machine-learning classification in remote sensing: An applied review," *Int. J. Remote. Sens.* **39**, 2784–2817 (2018).
- G. Mountrakis, J. Im, and C. Ogole, "Support vector machines in remote sensing: A review," *ISPRS J. Photogramm. Remote. Sens.* **66**, 247–259 (2011).
- S. Barbon, A. P. A. da Costa Barbon, R. G. Mantovani, and D. F. Barbin, "Machine Learning Applied to Near-Infrared Spectra for Chicken Meat Classification," *J. Spectrosc.* **2018**, 1–12 (2018).
- A. Yevick, M. Hannel, and D. G. Grier, "Machine-learning approach to holographic particle characterization," *Opt. Express* **22**, 26884 (2014).
- A. Ishimaru, S. Kitamura, R. J. Marks, L. Tsang, C. M. Lam, and D. C. Park, "Particle-size distribution determination using optical sensing and neural networks," *Opt. Lett.* **15**, 1221 (1990).
- Z. Ulanowski, Z. Wang, P. H. Kaye, and I. K. Ludlow, "Application of neural networks to the inverse light scattering problem for spheres," *Appl. Opt.* **37**, 4027 (1998).
- V. V. Berdnik and V. A. Loiko, "Retrieval of size and refractive index of spherical particles by multiangle light scattering: neural network method application," *Appl. Opt.* **48**, 6178 (2009).
- L. M. Gugliotta, G. S. Stegmayer, L. A. Clementi, V. D. G. Gonzalez, R. J. Minari, J. R. Leiza, and J. R. Vega, "A Neural Network Model for Estimating the Particle Size Distribution of Dilute Latex from Multiangle Dynamic Light Scattering Measurements," *Part. & Part. Syst. Charact.* **26**, 41–52 (2009).
- J. J. Rudiger, K. Book, B. Baker, J. S. DeGrassie, and S. Hammel, "A machine learning approach for predicting atmospheric aerosol size distributions," in *Laser Communication and Propagation through the Atmosphere and Oceans VI*, A. M. van Eijk, S. M. Hammel, and J. P. Bos, eds. (SPIE, 2017), September 2017, p. 26.

21. H. C. van de Hulst, *Light Scattering by Small Particles* (Dover Publications, 1981).
22. C. F. Bohren and D. R. Huffman, *Absorption and Scattering of Light by Small Particles* (Wiley, 2004).
23. A. Macke, M. I. Mishchenko, K. Muinonen, and B. E. Carlson, "Scattering of light by large nonspherical particles: ray-tracing approximation versus T-matrix method," *Opt. Lett.* **20**, 1934 (1995).
24. W. R. C. Somerville, B. Auguie, and E. C. Le Ru, "SMARTIES: Spheroids Modelled Accurately with a Robust T-matrix Implementation for Electromagnetic Scattering," *Astrophys. Source Code Libr. record ascl:1603.007* (2016).
25. J.-P. Schäfer, "Implementierung und Anwendung analytischer und numerischer Verfahren zur Lösung der Maxwellgleichungen für die Untersuchung der Lichtausbreitung in biologischem Gewebe," Ph.D. thesis, Universität Ulm (2011).
26. J. Schäfer, S.-C. Lee, and A. Kienle, "Calculation of the near fields for the scattering of electromagnetic waves by multiple infinite cylinders at perpendicular incidence," *J. Quant. Spectrosc. Radiat. Transf.* **113**, 2113–2123 (2012).
27. S. Theodoridis, *Machine Learning* (Elsevier, London, 2015).
28. T. Hastie, R. Tibshirani, and J. Friedman, *The Elements of Statistical Learning*, vol. 27 of *Springer Series in Statistics* (Springer New York, New York, NY, 2009).
29. O. Muñoz, F. Moreno, D. Guirado, J. L. Ramos, A. López, F. Girela, J. M. Jerónimo, L. P. Costillo, and I. Bustamante, "Experimental determination of scattering matrices of dust particles at visible wavelengths: The IAA light scattering apparatus," *J. Quant. Spectrosc. Radiat. Transf.* **111**, 187–196 (2010).
30. O. Muñoz, F. Moreno, D. Guirado, D. Dabrowska, H. Volten, and J. Hovenier, "The Amsterdam–Granada Light Scattering Database," *J. Quant. Spectrosc. Radiat. Transf.* **113**, 565–574 (2012).
31. D. D. Dabrowska, O. Muñoz, F. Moreno, J. L. Ramos, J. Martínez-Frías, and G. Wurm, "Scattering matrices of martian dust analogs at 488nm and 647nm," *Icarus*. **250**, 83–94 (2015).
32. J. Escobar-Cerezo, O. Muñoz, F. Moreno, D. Guirado, J. C. Gómez Martín, J. D. Goguen, E. J. Garboczi, A. N. Chiaromonti, T. Lafarge, and R. A. West, "An Experimental Scattering Matrix for Lunar Regolith Simulant JSC-1A at Visible Wavelengths," *The Astrophys. J. Suppl. Ser.* **235**, 19 (2018).
33. S. Merikallio, O. Muñoz, A.-M. Sundström, T. H. Virtanen, M. Horttanainen, G. de Leeuw, and T. Nousiainen, "Optical modeling of volcanic ash particles using ellipsoids," *J. Geophys. Res. Atmospheres* **120**, 4102–4116 (2015).
34. O. Muñoz, H. Volten, J. W. Hovenier, B. Veihelmann, W. J. van der Zande, L. B. Waters, and W. I. Rose, "Scattering matrices of volcanic ash particles of Mount St. Helens, Redoubt, and Mount Spurr Volcanoes," *J. Geophys. Res. D: Atmospheres* **109**, 1–16 (2004).
35. H. Volten, O. Muñoz, E. Rol, J. F. de Haan, W. Vassen, J. W. Hovenier, K. Muinonen, and T. Nousiainen, "Scattering matrices of mineral aerosol particles at 441.6 nm and 632.8 nm," *J. Geophys. Res. Atmospheres* **106**, 17375–17401 (2001).
36. O. Muñoz, H. Volten, J. F. De Haan, W. Vassen, and J. W. Hovenier, "Experimental determination of the phase function and degree of linear polarization of El Chichón and Pinatubo volcanic ashes," *J. Geophys. Res. Atmospheres* **107**, 1–8 (2002).
37. O. Muñoz, H. Volten, J. F. de Haan, W. Vassen, and J. W. Hovenier, "Experimental determination of scattering matrices of randomly oriented fly ash and clay particles at 442 and 633 nm," *J. Geophys. Res. Atmospheres* **106**, 22833–22844 (2001).
38. D. D. Dabrowska, O. Muñoz, F. Moreno, T. Nousiainen, E. Zubko, and A. C. Marra, "Experimental and simulated scattering matrices of small calcite particles at 647nm," *J. Quant. Spectrosc. Radiat. Transf.* **124**, 62–78 (2013).
39. R. Fletcher and D. Bright, "Shape Factors of ISO 12103-A3 (Medium Test Dust)," *Filtr. + Sep.* **37**, 48–56 (2000).
40. C. M. Riley, W. I. Rose, and G. J. S. Bluth, "Quantitative shape measurements of distal volcanic ash," *J. Geophys. Res. Solid Earth* **108**, 1–15 (2003).

3.5 Appendix A: Size Group Optimization

During the training process, one of the factors used for the optimization of the number of size groups was the cross-validation errors of the classification and regression models, shown in Figures 6 and 7. As a clarification, the cross-validation RMS errors shown in Figure 7 are based on an assumption that the testing input belongs in that size group, meaning that the classification model has accurately sorted the input in the previous layer.

4. Non-intrusive optical measurements of gas turbine engine inlet condensation using machine learning

The contents of this chapter have been accepted to be published in *Measurement Science and Technology* (C. Y. Moon, A. Panda, G. Byun, C. Frederic Smith, and K.T. Lowe, "Non-intrusive optical measurements of gas turbine engine inlet condensation using machine learning". doi:10.1088/1361-6501/abcf63

Author's Original/Preprint version of the accepted manuscript has been included with permission from IOP Publishing.

Non-intrusive optical measurements of gas turbine engine inlet condensation using machine learning

Chi Young Moon¹, Alka Panda¹, Gwibo Byun¹, C. Frederic Smith², and K. Todd Lowe¹

¹ Crofton Department of Aerospace and Ocean Engineering, Blacksburg, VA, USA

² Rolls-Royce North American Technologies, Inc., Indianapolis, IN, USA

E-mail: chimoon@vt.edu

XX 2020

Abstract. We demonstrate a novel application of supervised machine learning (ML) models to quantify the size, shape, number density, and distribution parameters of a water spray introduced at a gas turbine inlet. Only a limited set of laser scattering and extinction observations, acquired by pairs of photodetectors and cameras, are required for an accurate output. A phase Doppler particle analyzer (PDPA) as well as a conventional extinction inversion method are used to validate the particle size estimation, with the ML method converging closely to both. By measuring a water spray, where a spherical particle shape can be assumed, these size estimate validations were allowed to be made, which would have been difficult for a non-spherical particle measurement. By combining all the estimated parameters, the liquid volume fraction (LVF) as well as the liquid flow rate is estimated and compared to a traceable ultrasonic flowmeter. To our knowledge, this is the first *in situ* condensation load measurement made at a gas turbine inlet without a prior calibration. The ML approach is able to accurately estimate the liquid flow rate, with the majority of the estimates lying within the uncertainty bounds of the flowmeter and a root-mean-square difference of 0.8 L/hr or 7.4 %. Estimating the liquid flow rate using all the particle parameters demonstrates the method's robustness and readiness for accurately measuring even non-spherical particles. The low number of required optical observations also makes this technique attractive for more generalized inlet particle measurements including sand, dust, and volcanic ash, in addition to condensation.

Submitted to: *Meas. Sci. Technol.*

1. Introduction

Particle ingestion is a critical issue for turbine engine operations. Whether it is ice or volcanic ash during flight, sand at airports near deserts, or excessive moisture and condensation during ground testing, particle ingestion can cause damage and impact the engine’s performance [1, 2, 3, 4]. Water ingestion is of particular interest for ground testing, due to its effect on engine performance. Condensation can occur naturally at the inlet and cause as much as a 2% increase in specific fuel consumption (SFC) [3].

Figure 1 shows the condensation formation process and how it affects the fan performance. The important factors in determining if and how much condensation will form in the inlet is determined by the ambient (specific humidity and temperature of the air), and flow (inlet geometry and Mach number) conditions. As the flow accelerates, the static pressure (P_s) and temperature (T_s) of air decreases. The static pressure and temperature of the water vapors mixed within the air also decreases, with pressure decrease affected by the specific humidity. If sufficient conditions are met, the static temperature will drop to the saturation line, where water can exist as liquid and vapor in equilibrium. At this condition, a portion of the water vapor must condense to maintain this equilibrium, forming liquid water as condensation.

As liquid water forms through condensation, its latent heat of condensation is released, raising the total temperature (T_t). The increased total temperature is what leads to the performance decreased at the fan. With the increased total temperature of the flow, more work is needed to produce the same fan pressure ratio, which leads to higher fuel consumption and higher thrust specific fuel consumption (TSFC).

In addition, the water droplets can form a thin film on the airfoil surface, deviating its performance parameters from design [3, 5]. Valuable testing time is lost when the relative humidity and temperature readings indicate that the condensation effects are over the acceptable limit [6, 3].

While limited empirical corrections are available, an accurate measurement of the ingested mass is needed to develop reliable relationships between engine performance and condensation [6, 3]. Quantities that need to be reliably measured for this purpose are droplet volume and number density. Earlier efforts on inlet condensation study revealed droplet size distributions ranging from 1 to 30 μm [6].

Optical methods are attractive for this application as they can be non-intrusive. In particular, Mie extinction is a viable technique for this purpose, as the setup can be relatively simple and only limited optical access is needed [7]. Conventional extinction methods rely on the spherical assumption, which can

be made safely for condensation measurements but not for typical solid particle ingestion. While laser extinction for particle sizing has a long development history, a common limitation has been the wavelength of laser used. When using multiple lasers with different wavelengths, they have been limited to a narrow spectral band, typically from near-UV to near-IR. The narrow spectral width introduces ambiguities and limits the ability to size larger particles. These limits would prevent measurements of condensation with the upper limit of 30 μm in diameter [8, 9, 10]. The theoretical benefit of extending the spectral width was studied along with a novel way to utilize multi-wavelength laser extinction [7, 11]. Potter et al. [3] measured the liquid water content (LWC) of condensation entering in a subsonic suction tunnel as a mock inlet using a CO₂ laser emitting at 10.6 μm . However, using a single wavelength extinction, this method required an external measurement of LWC to calibrate the measurements. Replacing CO₂ lasers, the proliferation of quantum cascade (QC) lasers led to affordable and off-the-shelf lasers that can emit in the mid to far infrared [12].

The extended spectral width allows for the following two things. First is an application of an existing wavelength-multiplexed laser extinction (WMLE) method using the extended capabilities provided by the QC laser [7, 11, 13]. More importantly, a machine learning (ML) approach for particle characterization is achieved using multi-wavelength extinction as one of its features. Previous efforts demonstrated the concept of ML models and a vast library of relevant particle data for model training and validation [14].

We present an application of supervised machine learning models for inlet particle measurements, using a water spray as a stand-in for condensation. The introduction of laser extinction as a feature allows for a calibration-free measurement of ingested mass flow of condensation in a gas turbine inlet. In addition, while the previous models only solved for an equivalent mean diameter for non-spherical particles, the presented method expands on them by introducing additional model layers that estimate for particle shape (via aspect ratio) and particle distribution width. While droplet shapes could safely be assumed as spherical, the presented method does not rely on such an assumption, and we demonstrate its ability to estimate the particle shape for showing the robustness of the method and to prepare for future applications for solid non-spherical particles that inlets are likely to encounter, such as dust and sand.

Machine learning is a statistical tool that uses data to fit functions that can model complex systems [15]. Our previous efforts used a pre-established

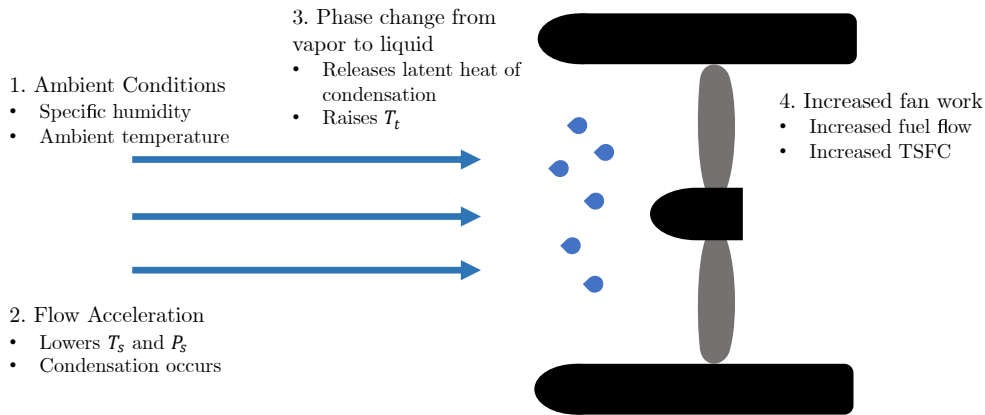


Figure 1. A diagram describing the steps of inlet condensation and its effect on fan performance.

library of particle scattering data to accurately size non-spherical particles found in the literature [14]. The features used previously were scattering intensity ratios at different scattering angles and an intensity shift relative to a known reference, requiring a calibration. In the presented method, multi-wavelength extinction replaces that intensity shift while keeping the scattering intensity ratio as features. The current developments are a major step forward for robust, precision measurements in harsh industrial applications, in our case gas turbine engine inlets, of particle ingestion rates without the need for prior calibration.

This paper is structured as the following. Section 2 describes the overall methods, including the library used as the training data, model setup, experimental method to acquire the input data, uncertainty quantification, and the validation methods. Section 3 describes the acquired data from the experiment, model outputs including estimated particle shape, size, and distribution, as well as their comparison to the validation data, followed by an overall conclusion in section 4.

2. Methods

An overview of the method is shown on Figure 2. A scattering and extinction library based on particles of interest is generated using numerical tools. This library is then used to train a series of supervised machine learning models designed to estimate the particle shape, distribution width, and Sauter mean diameter based on established inputs. The inputs, the intensity and extinction ratios, are acquired in measurements of a water spray introduced to a test engine inlet at Virginia Tech. The intensity ratio is measured by two cameras capturing the scattering intensity from the droplets using a scanning laser sheet. The extinction ratio at two different wavelengths is

measured by two photodetectors, using the intensity with and without the water spray in the flow. The inputs are then put through the layers of the machine learning models to determine the particle parameters. In the following subsections, each step presented on the overview is described in detail.

2.1. Particle Scattering and Extinction Library

The library is used to train the models that evaluate the inputs. For accurate models, the entry parameters in the library must encompass the range of expected particles the sensor is likely to see. The main varying parameters for the library are the particle shape, distribution width, and Sauter mean diameter. The current iteration of the library uses ellipsoids and spheres as shapes. The input measurements from the experiment were measured in a long straight optical section. Therefore, no significant acceleration and droplet deformation are expected, and spherical entries are sufficient for modeling the droplets. However, oblate and prolate ellipsoid entries were included in the dataset and training to verify that the models could estimate the shape as spheres, a way to demonstrate the method’s robustness and for future applications on solid non-spherical particles, such as sand and ash.

Table 1. Range of parameters included in the library.

Parameter	Values
D_{32} (μm)	0.1 - 50
σ	1.2 - 1.8
Aspect Ratio	0.5 - 2.0

Table 1 shows the parameter ranges used to populate the library. While numerical tools were used to initially generate monodisperse scattering and extinction data, a log-normal distribution was used to integrate them to represent a polydisperse cloud of particles of different mean size (D_{32}), distribution

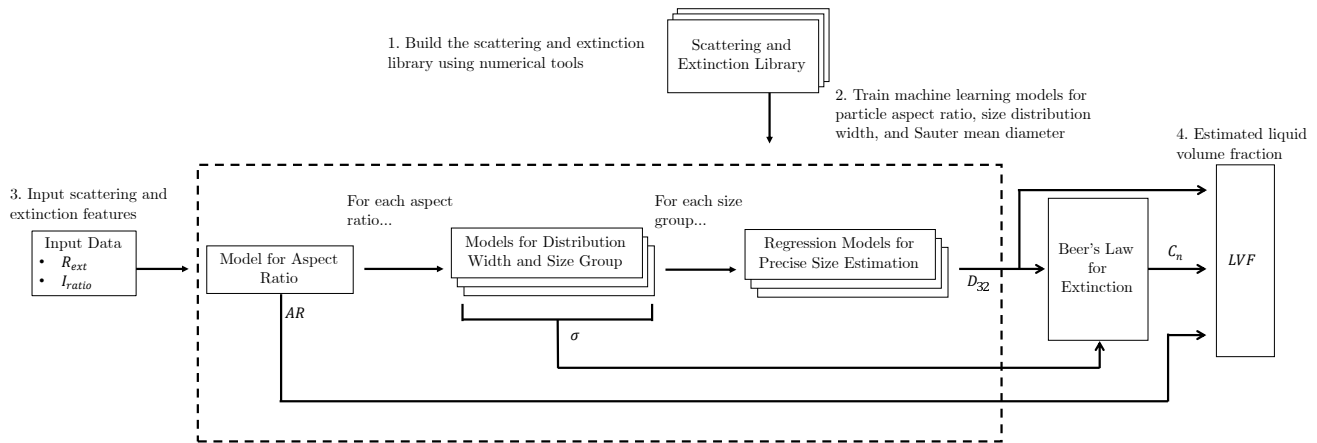


Figure 2. A diagram of the overall methods presented, from library population to estimating particle Sauter mean diameter (D_{32}), distribution width (σ), aspect ratio (AR), number density (C_n), and liquid volume fraction (LVF).

width (σ), and shape (aspect ratio). A log-normal distribution is defined as:

$$f(D) = \frac{1}{\sqrt{2\pi}D \ln \sigma} \exp\left[-\frac{1}{2 \ln(\sigma)^2} (\ln(D) - \ln(\bar{D}))^2\right] \quad (1)$$

Where \bar{D} is the mean diameter and σ is the distribution width. The Sauter mean diameter (SMD), D_{32} , is a useful metric that describes the diameter of a sphere with an equivalent surface area to volume ratio as the particle. It is defined as:

$$D_{32} = \frac{\int_0^\infty f(D)D^3 dD}{\int_0^\infty f(D)D^2 dD} \quad (2)$$

SMD is also twice the value as the effective radius r_{eff} , typically used in meteorology for describing cloud droplet distributions. This metric represents the mean radius for scattering [16]. The mean diameter \bar{D} is related to the SMD by:

$$\ln(\bar{D}) = \ln(D_{32}) - \frac{5}{2}(\ln(\sigma))^2 \quad (3)$$

σ is the geometric standard deviation for the distribution, which describes the following among other things: 95% of all particles in the distribution lie in the range from $\bar{D}/2\sigma$ to $\bar{D}2\sigma$ [17]. σ value of 1 describes a monodisperse distribution.

The aspect ratio (AR) is used for describing the particle shape. For spheres where $AR = 1$, the log-normal distribution described above can be used to represent particle distributions using the sphere diameter. However, for non-spherical prolate and oblate spheroids, an equivalent surface area sphere radius (and diameter) is used for calculating the distribution parameters [18].

For the parameters described in this section, the number of points used to fill out the range determines the number of data points within the library. A full-factorial combination of five hundred, six, and seven entries was used to fill out the Sauter mean diameter

(D_{32}), the standard deviation (σ), and the aspect ratio (AR), respectively. This brings the entire library to $500 \times 6 \times 7 = 21,000$ unique points.

The calculated quantities for each data points are the scattering intensity profiles (S_1 and S_2) and the extinction efficiency (\bar{Q}_{ext}). Three different numerical tools were used to calculate these quantities: MatScat [19], SMARTIES [20], and a geometric optics ray-tracing tool developed by Macke et. al [18]. MatScat uses Mie theory for spheres, while SMARTIES uses the T-matrix method for spheroids. These two methods provide exact solutions for their respective shapes but are limited by the particle size that can be computed for a given incident wavelength. The size parameter is a non-dimensional number that describes the ratio between the characteristic length of the particle and the incident wavelength. For a spherical particle, it is defined as:

$$x = \frac{2\pi r}{\lambda} \quad (4)$$

Where r is the particle radius and λ is the incident wavelength. For non-spherical particles, r is once again the equivalent surface-area-sphere radius. As x increases, the exact solution methods, especially the T-matrix method, face convergence issues. For larger particles (and therefore x values), the geometric optics approximation is used to calculate for the scattering parameters, which is accomplished by the Macke ray-tracing code suite. The ray-tracing code was used when SMARTIES failed to converge. While varying slightly for different aspect ratios, the switching point was $x \approx 50$. Macke et al. verified the ray-tracing code's ability to accurately calculate the scattering profiles for particles in this size parameter range [18]. For the ratio of extinction, a simple validation test was performed using only spheres, since exact solutions for spheres can converge for large particles given enough processing time. Between the exact solutions and combined

case of SMARTIES and ray-tracing, a peak error of 6% in ratio of extinction occurred only for the very small particles ($D_{32} \leq 1 \mu m$), providing confidence that the ray-tracing approximation is sufficient for populating the particle library. The ray-tracing tool also features averaging random orientations for non-spherical particles.

In accordance with the experimental setup, the scattering intensity profiles are calculated using an incident wavelength of 488 nm. For the extinction efficiencies, 532 nm and 10,330 nm are used as the incident wavelength.

2.2. Machine Learning Models

The entries in the scattering and extinction library are used to train and validate the machine learning models. Machine or statistical learning models use the library data to fit functions that relate the particle's scattering and extinction patterns to its characteristics. The application of supervised machine learning models for estimating non-spherical particle characteristics was demonstrated previously by the authors [14]. Many of the basic details regarding the method can be found in this prior publication. The current work expands on the previous efforts by introducing new features and additional model layers for shape and size distribution estimation.

The first input, the scattering intensity ratio R_{int} , is carried over from the previous iteration. It is a ratio of scattered light intensity between forward scattering (near 2 degrees) and side scattering (near 40 degrees) angles. The forward scattering region is generally sensitive to particle size, while the side scatter is used to normalize the forward scattering intensity. This negates any need for calibration between different laser intensities and camera properties.

The second input is the extinction ratio between two wavelengths. Two lasers at different wavelengths (532 nm and 10330 nm) are introduced to the particle flow, and its incident and transmitted intensities are recorded. For a single wavelength, the measured extinction τ is expressed as:

$$\tau_i = -\ln \frac{I_t}{I_0} \quad (5)$$

Where τ_i is the measured extinction at a given wavelength λ_i , I_t and I_0 are the transmitted and incident laser intensities, respectively. The extinction ratio can be formed as the following:

$$R_{ext,ij} = \frac{\tau_i}{\tau_j} = \frac{\overline{Q}_{ext}(\lambda_i, D_{32})}{\overline{Q}_{ext}(\lambda_j, D_{32})} \quad (6)$$

From the library perspective, the extinction ratio (measured) is equal to the ratio of the mean extinction efficiencies \overline{Q}_{ext} (calculated) at the same wavelengths.

The addition of the extinction ratio as a feature eliminates the need for the prior calibration feature from the method's previous iteration.

Figure 3 shows the difference in input features based on the particle parameters. The feature response to the aspect ratio is shown on Figure 3a. As the aspect ratio deviates from 1, the features trend in the same direction, with the $AR = 0.5$ case being noticeably different. As the distribution width increases on Figure 3b, the scattering intensity ratio smooths out the feature behavior as expected. Figure 3c shows that as the particle size increases, the extinction ratio converges to a value of one, due to the fact that Q_{ext} converges to a value of two. The smallest particles in the library still have a finite size ($D_{32} = 0.1 \mu m$). The extinction efficiency terms used to calculate the ratio of extinction converge to 0 as particle size approaches 0, but reviewing the library data showed that the difference in the two wavelengths leads to the brief increase in the extinction ratio for extremely small particles, visible in Figure 3c.

The models in different layers shown in Figure 2 are set and trained for their own objectives. The aspect ratio and the size group layers use classification models, while the distribution width and the precise size estimation uses regression models. Classification models have distinct and pre-allocated outcome variables, while regression models have quantitative outcome variables [21]. While there are many different models for both classification and regression, based on our previous work, an approach comprising the k-nearest neighbor (KNN) method for classification and the ensemble boosted tree method for regression is used [14].

The data used to train the models in different layers are filtered based on the previous step. For example, while the model for determining the aspect ratio is trained using the entire library, the models for distribution width and size group are trained using only the library entries with corresponding aspect ratio. The regression models are trained using only library data for the corresponding shape and the size group.

The models are trained using the library data, and their hyperparameters are optimized through cross-validation. The training data are randomly shuffled into training and validation sets. Models are scored post-training using the validation set, then the process is repeated to converge on maximum training accuracy. For classification models, the training accuracy is simply its accuracy score on correctly identifying the validation sets. For regression models, the training iteration minimizes the error on validation set estimation. The optimization objectives were monitored for convergence with one thousand iterations as the maximum iteration limit. While

Feature Maps

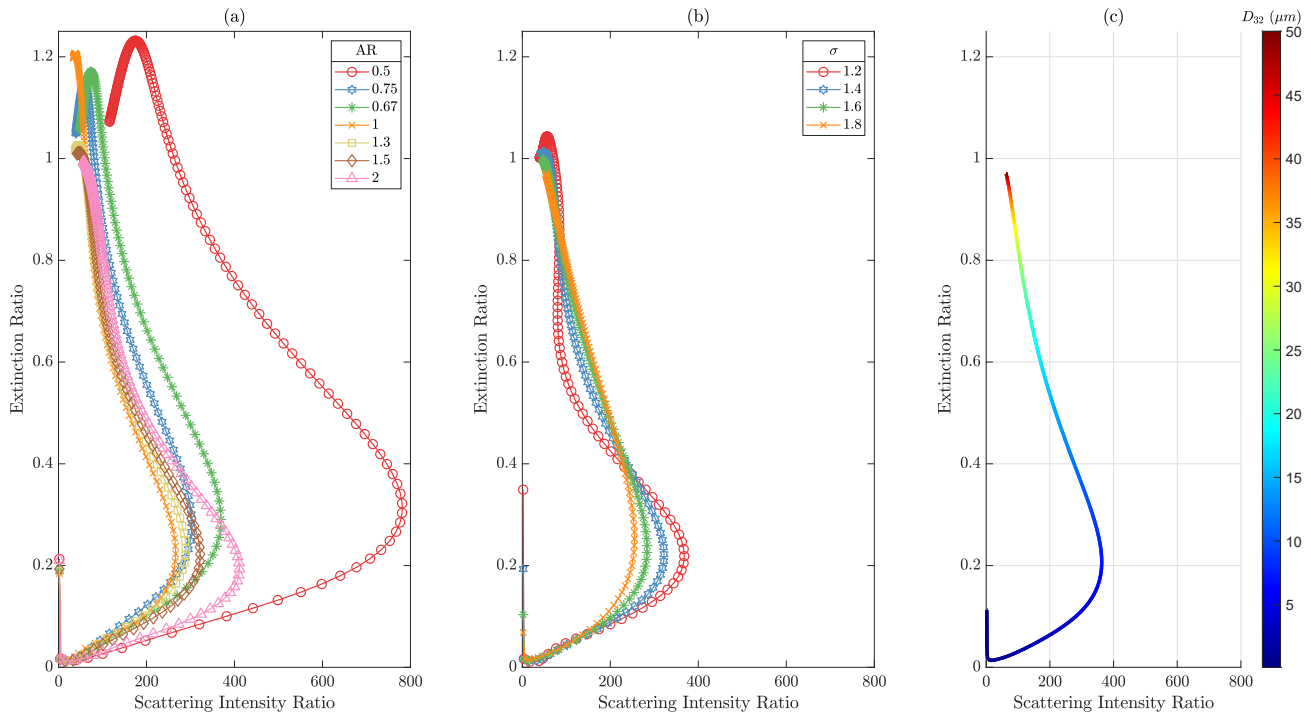


Figure 3. The feature space showing the ranges in the library. (a) Profiles showing different aspect ratios. Only entries with $\sigma = 1.4$ are shown for clarity. (b) Profiles representing different distribution widths. Only entries with $AR = 1.5$ are shown for clarity. (c) Profiles representing different Sauter mean diameter. The aspect ratio and distribution width are limited to 2.0 and 1.6, respectively.

no convergence criteria were set to stop the training process before the maximum iteration limit, the training process for all models reached the maximum performance parameters before 200 iterations. These model parameters with best performances were then used with the experimental inputs.

2.3. Experimental Setup and Input Features

An experiment was performed on a test engine at Virginia Tech to demonstrate the ability to measure mass flow rate of water ingestion in an engine inlet using this novel technique. A test section with optical access for the laser beams was attached between the bell mouth inlet and the fan on a Pratt & Whitney Canada JT15D research engine. Figure 4 shows the experiment schematic for the extinction ratio input, as well as the photos of the implemented setup. An atomizing nozzle upstream of the bell mouth was used to produce the water spray. The JD Ultrasonics Sonicom 086H nozzle was mounted 0.53 m (equivalent to the test section diameter) ahead of the bell mouth. The spray nozzle was supplied with pressurized water and air for its operation. The air and water pressure were fixed at 483 kPa and 103 kPa, respectively. The pressurized water

flow from the pressure pot was connected to an Atrato Ultrasonic Flowmeter Model 720V20SD/A. This National Physical Laboratory (NPL) traceable flowmeter recorded the flow rate while the spray was on. This recorded flow rate was then used to verify the estimated flow rate.

Figure 4a shows the experiment layout with the location of the extinction lasers and the detector unit. The two laser beams at different wavelengths are combined into a single beam. As shown in figure 4b, the 532 nm beam (visible green) emitted by a Genesis MX laser is simply reflected using a silver mirror. A Thorlabs model MLQ MIR quantum cascade laser emits at 10330 nm (infrared), which is then reflected by a N-BK7 window. N-BK7 is optically clear substrate that allows the 532 nm beam through but reflects the infrared beam to combine them. A box constructed from black acrylic panels covered the lasers to protect them from water and dust during engine operations.

Optical access to the test section is provided by BaF₂ windows on both sides. This material was chosen as it allows the transmission of both visible and infrared beams. After going through the flow, the combined beam enters the detector unit and is split according to the wavelength, then introduced to a spectral filter and a lens to focus the beam onto

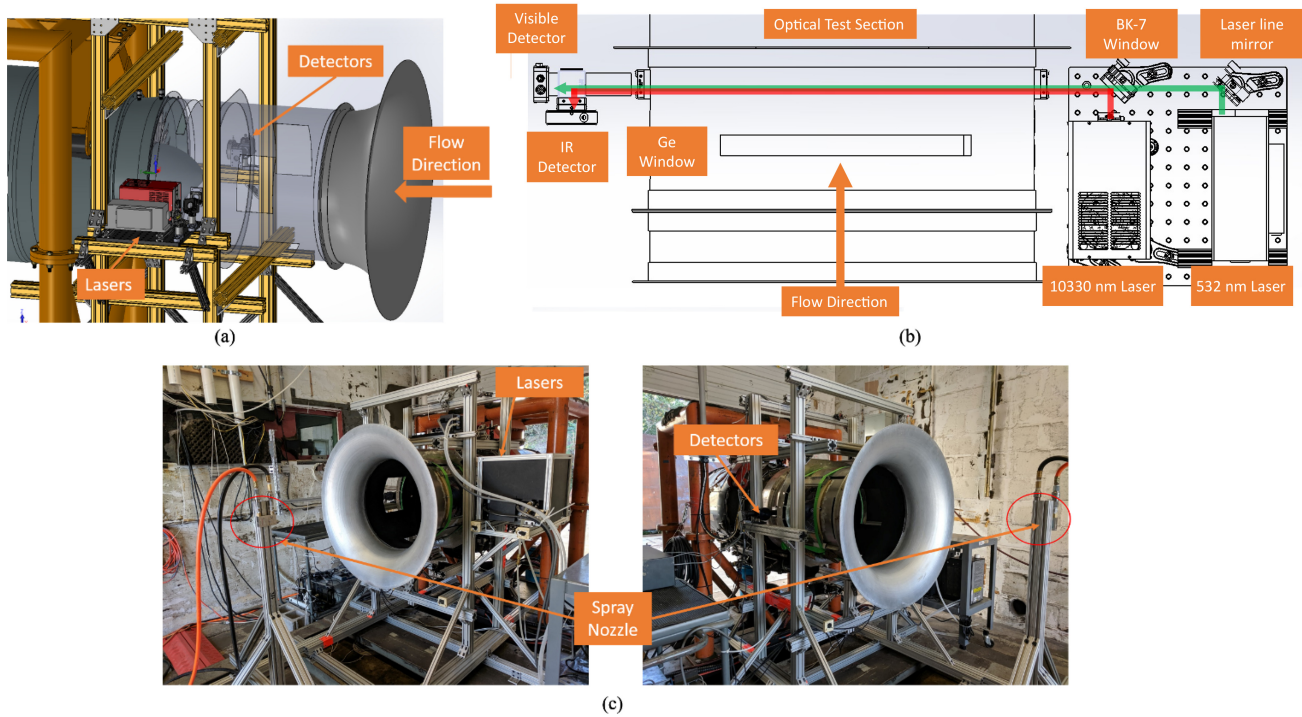


Figure 4. (a) Overall layout of the engine experiment and the location of the extinction lasers and detectors. (b) A top view of the lasers and detectors, as well as the beam paths of each laser. (c) Photos of the experimental setup, including the location of the spray nozzle.

the detector surface. For the 532 nm beam, a 532 nm laser line filter and an achromat lens were used. For the 10330 nm beam, a Germanium longpass filter and a ZnSe plano-convex lens were used. A Thorlabs PDA100A amplified photodetector was used to record the 532 nm laser intensity, while a Newport 919P-003-10 thermopile sensor was used for the 10330 nm laser. A detailed schematic of the extinction laser and detector units are shown in figure 4b. The intensities were recorded on a data acquisition computer in the engine control room.

In addition to the extinction setup, an imaging system for recording the scattering intensities and visualizing the spray pattern at the measurement plane was implemented using a laser sheet. Figure 5 shows the General Scanning Inc. scanning mirror used to create the laser sheet, based on a 488 nm laser emitted by a Genesis MX laser. Any interference between the extinction and scattering measurements was prevented using spectral bandpass filters on both detectors and cameras. The extinction and scattering measurement planes were 19 inches downstream from the bell mouth inlet.

Two Thorlabs DCC3240M CMOS cameras were used to capture the images. These cameras were placed in locations that would provide the angular location described in the previous section. The forward

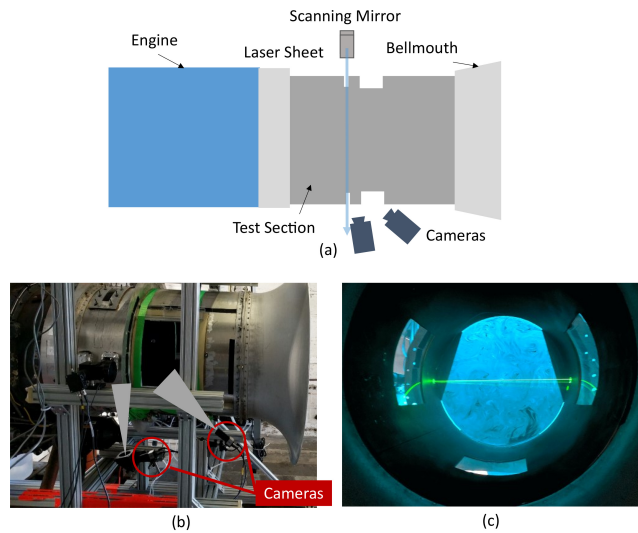


Figure 5. (a) A schematic of the scattering setup. (b) A photo of the scattering setup beneath the test engine. (c) A photo showing the laser sheet for scattering measurements, enhanced using a smoke generator.

scattering camera used a 90 degree mirror to capture the image. Images with a checkerboard plate in the imaging plane were used to spatially calibrate the cameras. The spray images taken were then warped to real-world aspect ratios.

Three different engine conditions were tested: idle, 60%, and 65% corrected fan speed (CFS). At each engine condition, three spray and two clean runs were recorded for 5 minutes. The mean intensities recorded at spray and clean runs were used for the transmitted (I_t) and incident (I_0) intensity terms in equation (5), respectively. Images taken during the clean runs were used for background subtraction.

2.4. Flow Rate Estimation

The extinction and scattering data captured by the setup described in the previous section is used as inputs to the trained machine learning models. The outputs from those models are then used to estimate the liquid volume fraction (LVF). The liquid water content is defined as:

$$LVF = V_{droplet} C_n \quad (7)$$

where $V_{droplet}$ is the volume of the particle in m^3 , and C_n is the number density in number of particle per unit volume. The particle volume is determined based on the shape and size outputs from the models. The number density is determined using the model outputs in Beer's law for extinction:

$$\tau_i = -\ln \frac{I_t}{I_0} = \frac{\pi}{4} C_n L \int_0^\infty Q_{ext}(x, m) f(D) D^2 dD \quad (8)$$

where L is the beam path length in m . The $\pi D^2/4$ term comes from the projected area of a sphere, making this the spherical form of Beer's law. Since the estimated SMD is based on the equivalent area sphere diameter, there is no need to recalculate the area based on the estimated particle shape. With the measured extinction τ_i , set path length L , and the estimated size distribution f and shape, the number density term C_n is found using the measured extinction at 532 nm.

While LVF is typically used for engine performance and condensation correlation, for verification purposes, we use the liquid flow rate to compare against the flowmeter. The flow rate is:

$$\dot{V}_{liquid} = (LVF) \dot{V}_{engine} \quad (9)$$

where \dot{V}_{engine} is the engine's air flow rate, measured from a previous test with identical engine conditions.

2.5. Uncertainty Analysis

The uncertainty in the liquid flow rate estimate is determined using the model sensitivity on outputs using simulated inputs and the experimental uncertainty on acquiring the inputs. By considering the two inputs (extinction and intensity ratios) for the LVF estimation:

$$\delta LVF = \sqrt{(\delta R_{ext})^2 \left(\frac{\partial \dot{V}_{liquid}}{\partial R_{ext}} \right)^2 + (\delta R_{int})^2 \left(\frac{\partial \dot{V}_{liquid}}{\partial R_{int}} \right)^2} \quad (10)$$

The partial derivative terms representing the output sensitivity based on the input is found using simulated inputs into the model.

The uncertainties in the LVF estimate as well as the engine flow rate measurement are considered for the uncertainty in the liquid flow rate estimation:

$$\frac{\delta \dot{V}_{liquid}}{\dot{V}_{liquid}} = \sqrt{\left(\frac{\delta LVF}{LVF} \right)^2 + \left(\frac{\delta \dot{V}_{engine}}{\dot{V}_{engine}} \right)^2} \quad (11)$$

The engine flow rate uncertainty $\delta \dot{V}_{engine}/\dot{V}_{engine}$ was estimated to be 5% based on previous measurements.

2.6. Validation Methods

As mentioned in the experimental setup, a NPL traceable flowmeter is used to compare the \dot{V}_{liquid} estimation. The uncertainty of the flowmeter is rated to 1% of the full measurement range, approximately ± 1 L/hr. In addition, a TSI phase Doppler particle analyzer (PDPA) is used to independently measure the droplet size.

Since the droplets can be safely assumed spherical, a conventional wavelength-multiplexed laser extinction (WMLE) method for retrieving droplet size, distribution, and number density is also used to further validate this new ML approach [7, 11, 13]. The conventional method assumes the particles to be spherical and a log-normal distribution function. It fits the measured extinction ratio (same as the input feature used in the ML approach) to the size distribution parameters (the Sauter mean diameter and the distribution width), then uses Eq. 8 to estimate the number density. The WMLE method's uncertainty propagates from the estimated distribution width, as the method assumes a range of possible distribution width values that leads to the SMD and C_n estimations. A 5% uncertainty in the engine flow rate is used for the liquid flow rate estimation using the WMLE method as well.

3. Results and Discussion

The inputs acquired during the experiment (the extinction signals and the scattering images) are first presented. The model outputs from particle shape, size, and distribution parameters are then presented and compared against the PDPA and the conventional extinction (WMLE) method. In addition, combining all the estimated parameters, a comparison of measured liquid flow rate between the ML, WMLE, and the flowmeter is presented. For engine condition idle run 1, an error in camera settings led to unusable images to form an input feature. Therefore, in the following results sections, only 2 runs at engine condition idle are shown.

Table 2. Estimated aspect ratio from the shape classifier model using the experimental inputs.

Engine Condition	Run	AR
Idle	1	1.5
	2	1.5
60% CFS	1	1.0
	2	1.0
	3	1.0
65% CFS	1	1.0
	2	1.3
	3	1.0

3.1. Experimental Inputs

Figure 6 shows the normalized mean images from the side-scatter camera during engine condition 65% CFS. The image has been warped to real-world aspect ratios, and converted to real world spatial coordinates using the camera calibration data. Some image artifacts are visible from the background subtraction as the dark speckles in the image. The faint ring in the center is a reflection from the fan nose cone.

These images were taken to capture the scattering intensities to be used as inputs to the ML models. However, these images serve as an excellent visualization of the spray pattern and relative concentration as well as. A small patch of the images from both the forward- and side-scatter cameras that corresponds to the same physical space was used to form the intensity ratio input.

Figure 7 shows a short time sample from the extinction signals acquired during the experiment. The recording was started with the engine running at 60% CFS, then the water spray was started after approximately 10 seconds. After an initial burst of water passes through, the intensity profile shows the spray passing through the beam, lowering the intensity through absorption and scattering.

3.2. Particle Size and Shape Estimation

The outputs from the aspect ratio model are listed in Table 2. For most runs, the estimated shape is $AR = 1$ as expected. However, for engine condition idle, both runs estimated $AR = 1.5$ while run 2 of 65% CFS estimated as $AR = 1.3$. While we do not have a direct way for validating the shape estimation, the droplets are expected to be spherical. There are few possible explanations for the three discrepancies in the aspect ratio estimation. First of which can be gleaned by looking at Figure 3. In Figure 3a, where the different profiles show the library entries for the various aspect ratios, the profiles for $AR = 1, 1.3,$ and 1.5 are quite close to each other in the estimated size region of the droplets (using Figure 3c as a guide).

While small measurement errors would not lead to a large deviation in size estimation, they can easily result in the aspect ratio deviations shown in the results. This also shows that if the sensor application is purely limited to spherical particles, it may be better for the training library to only consist of spherical particle data to avoid such misleading results. As mentioned in the model training subsection, the current training scheme is vulnerable to overfitting and converging to a local minimum. Overfitting combined with the random variance in the measured inputs could also lead to the aspect ratio deviations and cascade down to errors in the size and flow rate estimations as well.

For future applications using irregular solid particles, a standardized shape factor, such as aspect ratio (L_{min}/L_{max}) will be utilized for rigorously validating the technique’s ability to accurately estimate the particle shape.

Table 3. Sauter mean diameter estimations from the ML and conventional extinction (WMLE) method, as well as the independent estimation from the phase Doppler particle analyzer (PDPA).

Engine Condition	Run	D_{32} (μm)	
		ML	WMLE
Idle	1	11.0	8.5
	2	11.9	8.2
60% CFS	1	9.3	8.4
	2	10.1	9.4
	3	9.2	9.1
65% CFS	1	9.5	9.7
	2	10.9	10.1
	3	10.1	11.6
PDPA		12.0	

Table 3 shows the estimated Sauter mean diameter using the machine learning (ML) approach, conventional extinction (WMLE) method, and a commercial PDPA system. The ML and WMLE methods have root-mean-squared differences of $1.96 \mu m$ and $2.82 \mu m$ (16.4 % and 23.2 %), respectively to the PDPA estimate. The ML method is closer to the PDPA measurement, while the WMLE approach seems to estimate smaller droplets compared to the other two methods. The engine setup did not allow *in situ* PDPA measurements, rather the spray was sampled by this instrument separately in a laboratory setting. This could explain some of the deviation between the methods in size estimation.

3.3. Flow Rate Estimation

Figure 8 shows the estimated liquid flow rate between the ML and WMLE method, as well as the recorded flow rate from the Atrato ultrasonic flowmeter. Only two ML estimates lie outside the uncertainty range

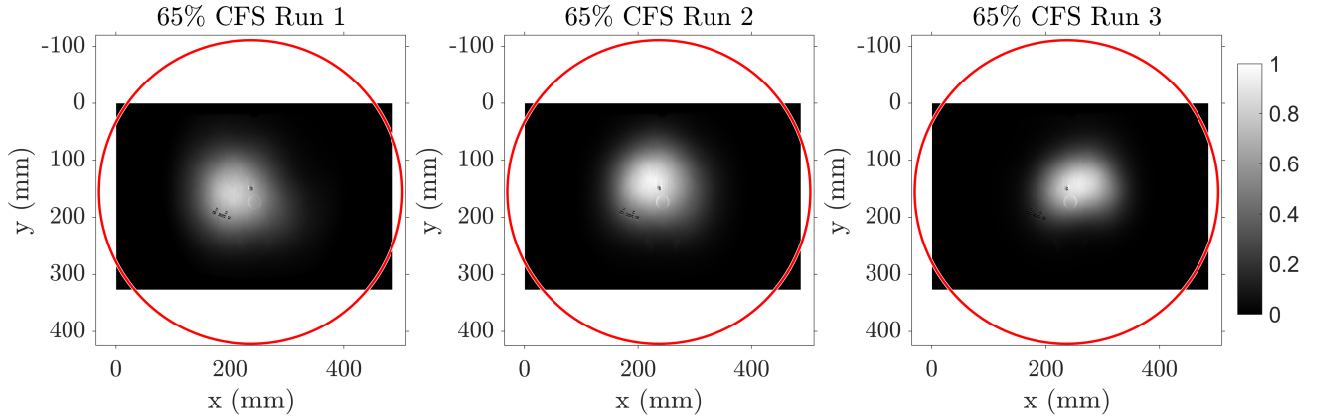


Figure 6. Normalized mean spray visualization images from the 65% CFS case. The outer rings represent the test section wall location.

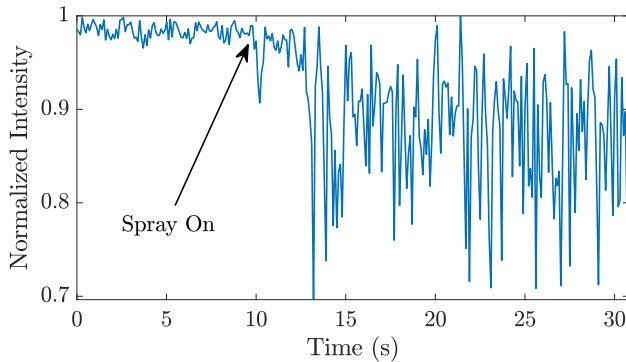


Figure 7. Normalized extinction signal from the 532 nm laser. The water spray is switched on around $t = 10$ seconds to demonstrate the measured extinction as the droplets pass through the beam path.

of the flowmeter (60% CFS Runs 1 and 2), but are still well within the overlapping uncertainties of the measurement and validation. Between the ML and WMLE methods, the RMS differences from the flowmeter are 0.8 and 1.0 L/hr (7.4 % and 8.2 %), respectively. As the flowmeter was installed in-line to the water spray while the experiment was performed and since the flow rate estimation uses all the estimated parameters (size, shape, distribution width), the comparison between the ML method and the flowmeter can therefore help validate the method’s ability to accurately estimate the droplet size, shape, and particle volumetric flowrate.

4. Conclusions

In this work, we presented a particle characterization method that uses light scattering and extinction as input features to a set of supervised machine learning models. The method’s ability to accurately estimate the shape, size distribution, and number density of

an ingested water spray was demonstrated on a test engine inlet. Using four observations (two extinction at different wavelengths and two scattering at different scattering angles) to form two input features, the ML models estimated the liquid flow rate produced by a spray nozzle to values within the uncertainty range of a traceable flowmeter and with a RMS difference of 0.8 L/hr (7.44%) through multiple engine conditions. While care must be taken to avoid draw conclusions when the estimation is within the flow meter uncertainty, the droplet size and shape estimations show that further analysis, especially into the model training and performance evaluation, is required to find the source of these deviations.

The limited number of required observations makes this method attractive for particle remote sensing. While a spherical assumption can be safely made for condensation measurements (as shown by the WMLE comparisons), engine inlets encounter many particles that are non-spherical. This ML method does not rely on such assumptions and can be applied for non-spherical particles.

A solid particle demonstration using non-spherical particles is currently being planned using different samples of test sand and dust. As the scattering and extinction library discussed above was established on water, a new library based on the new materials is being established for training.

In addition, the current approach of many layers filled with a number of models increases in complexity and computational training time as more shapes are introduced and the size range increases. An artificial neural network (ANN) would simplify that process, using the same library as the training data but fitting one function that can output all of the desired quantities, instead of going through the layers and layers of models. The training process described here are prone to overfitting and converging to a local

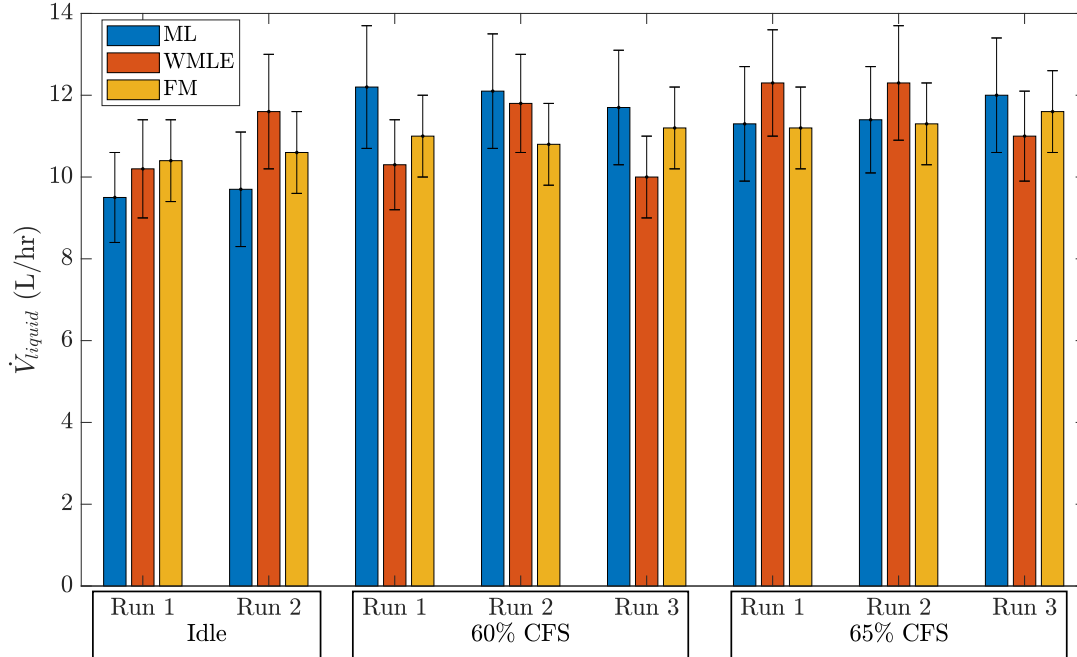


Figure 8. Flow rate estimations from the machine learning (ML) and conventional extinction (WMLE) method, as well as the Atrato ultrasonic flowmeter.

minimum. By employing strategies such as early stopping and training the same model multiple times with random weights, these risks can be avoided. As versatile as this method has already proven to be, we anticipate that these improvements will allow this machine learning approach to be an attractive instrument for particle characterization, particularly in gas turbine inlet settings.

Acknowledgements

This work was supported by Rolls-Royce North American Technologies, Inc. We would also like to thank Cody Dowd, Yogesh Aradhey, and Dr. Joseph Meadows for their assistance in acquiring the PDPA measurements.

References

- [1] R. J. Litchford, F. Sun, J. D. Few, and J. W. L. Lewis, "Optical Measurement of Gas Turbine Engine Soot Particle Effluents," *Journal of Engineering for Gas Turbines and Power*, vol. 120, no. 1, pp. 69–76, Jan. 1998.
- [2] M. G. Dunn, "Operation of Gas Turbine Engines in an Environment Contaminated With Volcanic Ash," *Journal of Turbomachinery*, vol. 134, no. 5, p. 051001, Sep. 2012.
- [3] J. Potter and R. P. Tatam, "Optical condensation measurement in gas turbine engine inlets," in *Optical Technology in Fluid, Thermal, and Combustion Flow III*, S. S. Cha, J. D. Trolinger, and M. Kawahashi, Eds., vol. 3172, Nov. 1997, pp. 422–433.
- [4] R. J. Clarkson, E. J. Majewicz, and P. Mack, "A re-evaluation of the 2010 quantitative understanding of the effects volcanic ash has on gas turbine engines," *Proceedings of the Institution of Mechanical Engineers, Part G: Journal of Aerospace Engineering*, vol. 230, no. 12, pp. 2274–2291, Oct. 2016.
- [5] T. Nikolaidis, "Water ingestion effects on gas turbine engine performance," PhD Thesis, Cranfield University, Feb. 2008.
- [6] J. Blake, "Effects of condensation in the JT9D turbofan engine bellmouth inlet," in *11th Propulsion Conference*. Reston, Virginia: American Institute of Aeronautics and Astronautics, Sep. 1975, pp. 0–9. [Online]. Available: <http://arc.aiaa.org/doi/10.2514/6.1975-1325>
- [7] L. Ma and R. K. Hanson, "Measurement of aerosol size distribution functions by wavelength-multiplexed laser extinction," *Applied Physics B*, vol. 81, no. 4, pp. 567–576, Aug. 2005. [Online]. Available: <http://link.springer.com/10.1007/s00340-005-1913-3>
- [8] L. Wang, X. Sun, K. Sun, and F. Li, "Retrieval of particle size distribution in multispectral region," in *International Conference on Optical Instruments and Technology: Optoelectronic Measurement Technology and Systems*, Nov. 2011, p. 82012H.
- [9] G. P. Box, K. M. Sealey, and M. A. Box, "Inversion of Mie Extinction Measurements Using Analytic Eigenfunction Theory," *Journal of the Atmospheric Sciences*, vol. 49, no. 22, pp. 2074–2081, Nov. 1992.
- [10] G. Ramachandran and D. Leith, "Extraction of Aerosol-Size Distributions from Multispectral Light Extinction Data," *Aerosol Science and Technology*, vol. 17, no. 4, pp. 303–325, Jan. 1992.
- [11] K. Barboza, L. Ma, K. Todd Lowe, S. Ekkad, and W. Ng, "A Diagnostic Technique for Particle Characterization Using Laser Light Extinction," *Journal of Engineering for Gas Turbines and Power*, vol. 138, no. 11, p. 111601, Nov. 2016.

- [12] Y. Yao, A. J. Hoffman, and C. F. Gmachl, "Mid-infrared quantum cascade lasers," *Nature Photonics*, vol. 6, no. 7, pp. 432–439, Jul. 2012. [Online]. Available: <http://dx.doi.org/10.1038/nphoton.2012.143>
- [13] C. Y. Moon, G. B. Byun, T. Lowe, and C. F. Smth, "Turbine Engine Ingested Particle Monitoring: A Novel Application of Quantum Cascade IR Laser Extinction," in *AIAA Propulsion and Energy 2019 Forum*. Reston, Virginia: American Institute of Aeronautics and Astronautics, Aug. 2019, pp. 1–8. [Online]. Available: <https://arc.aiaa.org/doi/10.2514/6.2019-4339>
- [14] C. Y. Moon, A. Gargiulo, G. Byun, and K. Todd Lowe, "Non-spherical particle size estimation using supervised machine learning," *Applied Optics*, vol. 59, no. 10, pp. 3237–3245, Mar. 2020.
- [15] G. James, D. Witten, T. Hastie, and R. Tibshirani, *An Introduction to Statistical Learning*, ser. Springer Texts in Statistics. New York, NY: Springer New York, 2013, vol. 103. [Online]. Available: <http://link.springer.com/10.1007/978-1-4614-7138-7>
- [16] J. E. Hansen and L. D. Travis, "Light scattering in planetary atmospheres," *Space Science Reviews*, vol. 16, no. 4, pp. 527–610, Oct. 1974. [Online]. Available: <http://link.springer.com/10.1007/BF00168069>
- [17] R. C. Flagan and J. H. Seinfeld, *Fundamentals of Air Pollution Engineering*. Englewood Cliffs, NJ: Prentice-Hall, Inc., 1988, vol. 202. [Online]. Available: <https://resolver.caltech.edu/CaltechBOOK:1988.001>
- [18] A. Macke, M. I. Mishchenko, K. Muinonen, and B. E. Carlson, "Scattering of light by large nonspherical particles: ray-tracing approximation versus T-matrix method," *Optics Letters*, vol. 20, no. 19, p. 1934, Oct. 1995.
- [19] J.-P. Schäfer, "Implementierung und Anwendung analytischer und numerischer Verfahren zur Lösung der Maxwellgleichungen für die Untersuchung der Lichtausbreitung in biologischem Gewebe," Ph.D. dissertation, Universität Ulm, Apr. 2011. [Online]. Available: <http://dx.doi.org/10.18725/OPARU-1914>
- [20] W. Somerville, B. Auguié, and E. Le Ru, "smarties: User-friendly codes for fast and accurate calculations of light scattering by spheroids," *Journal of Quantitative Spectroscopy and Radiative Transfer*, vol. 174, pp. 39–55, May 2016.
- [21] T. Hastie, R. Tibshirani, and J. Friedman, *The Elements of Statistical Learning*, ser. Springer Series in Statistics. New York, NY: Springer New York, 2009, vol. 27.

5. Neural-network-based instrument for particle detection and characterization

The contents of this chapter have been prepared for submission as a research article to *Optics Express* (C. Y. Moon, C. Edwards, G. Byun, and K. T. Lowe, "Neural-network-based instrument for particle detection and characterization"). It is in its corresponding submission format, provided by The Optical Society.

Neural-network-based instrument for particle detection and characterization

CHI YOUNG MOON,^{1,*} CAITLYN EDWARDS,¹ GWIBO BYUN,¹ AND K. TODD LOWE¹

¹ Crofton Department of Aerospace and Ocean Engineering, Virginia Tech, 460 Old Turner St., Blacksburg, VA 24061, USA

* chymoon@vt.edu

Abstract: We present a novel optical particle sensor technique using artificial neural networks. This method relies on observations of light scattering and extinction by particles as input features to a trained neural network, which provides relevant particle size and shape parameters for a mass flow estimation. The models are trained on artificial data, generated for particles that the sensor is likely to encounter. The feasibility of our method is demonstrated through an experimental measurement of solid sand particles injected into a high speed wind tunnel. The results show accurate estimations of the injected sand mass flow and particle size statistics, with a sand mass flow root-mean-square error of 0.28 *g/min* or 4.1% from the monitored rate using a precision scale. This measurement framework paves the way for sensor applications in harsh operating environments with limited optical access.

© 2020 Optical Society of America under the terms of the [OSA Open Access Publishing Agreement](#)

1. Introduction

Measurements of particle characteristics such as size and shape are important for a multitude of applications. Aerosol measurements are key components in numerous areas from pharmaceutical researcher into drug delivery and fuel spray atomization in combustion chambers [1, 2]. Remote sensing of non-spherical particles such as sand and ash are critical for atmospheric research as well as space planetary science [3, 4]. The presented research is focused on particle sensing at aerospace propulsion system inlets, where foreign ingested objects can induce significant damage to components [5]. Conventional particle measurement techniques are inadequate due to the complex particle shapes and challenging operating conditions [6–8].

Optical techniques require little access compared to sampling and can be non-intrusive, making them ideal for this application. However, most conventional optical methods for particle sizing assume the particle shape to be spherical, which leads to significant errors for relating ingested mass and effects on gas turbine components [9, 10].

We present a novel application of machine learning models for bridging this gap. Using optical measurements of light scattering and extinction from particles as unique identifying signatures, neural networks trained on synthetic data are used to estimate the particle shape and size statistics. A generalized neural network replaces layers of supervised machine learning models used in our previous efforts [11, 12]. This allows for faster training and much quicker parameter estimations, bringing this technology one step closer to real-time monitoring capabilities.

An experiment to measure the particle size and mass flow of injected sand particles in a high speed wind tunnel is conducted to demonstrate the sensor technology. This development is a major advancement for a robust and accurate measurement of particles in challenging environments.

This paper is structured as the following. Section 2 describes the method in detail, including the library generation, model training, and setup for the demonstrative experiment. Section 3 presents the results from the neural network training, experimental measurements, and the following estimations from the model. Comparisons of the particle size and mass flow rate estimations are also presented and discussed, with a brief discussion concluding the paper with a

summary and future works.

2. Methods

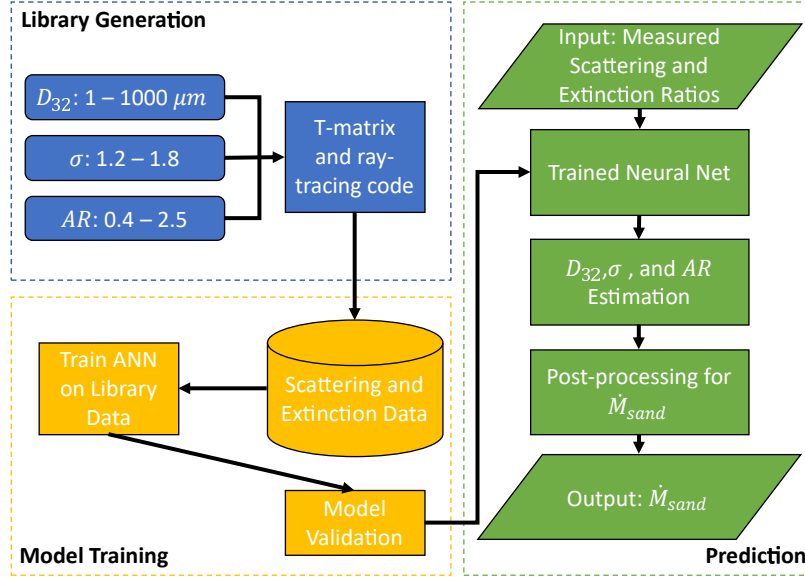


Fig. 1. A flowchart describing the overall process behind the particle sensor concept.

A diagram describing the overall scheme is shown in Figure 1. The synthetic training data for the neural network are first generated using numerical tools, representing the particles the optical sensor is likely to encounter. The particle scattering and extinction measured from the particle-laden flow in the wind tunnel are passed to the trained model for particle size and shape prediction. Those outputs are then used to estimate the injected sand mass flow rate. In the following subsections, each step listed in Figure 1 is described in detail.

2.1. The Particle Scattering and Extinction Library

Neural networks must first be trained before measured inputs can be used. Particle scattering and extinction data are generated artificially and used for training the models. The library must be populated with data representing the particles that the sensor is expected to see, providing the models with the numerical basis formulated by the governing physics.

The scattering and extinction library was previously used for an engine inlet condensation sensor [12]. The numerical tools and the general structure of the library are similar, while the particle parameters, such as the size range and the material refractive indices are changed to accommodate for sand particles. A brief explanation of the library and its composition are presented below, but a full description can be found in the cited source [12].

The highly-complex shapes of sand and dust particles necessitate the need for simpler shapes to be used as surrogates. Numerous particle modeling studies have confirmed that spheres are insufficient for modeling sand and dust particles [13, 14]. By fitting artificial scattering data from ellipsoids into measured dust data, spheroids (ellipsoids with one less degree of freedom) were found to perform very well for matching scattering intensities, but not for polarization parameters [13, 15, 16]. Therefore, the unpolarized scattering profiles ($|S^2|$) and extinction efficiencies (Q_{ext}) for both prolate and oblate spheroids are used to fill out the library.

The incident wavelengths used to calculate those values were matched to the lasers used as light sources in the experimental measurements. A visible wavelength at 488 nm was used for the scattering measurements while 532 nm (visible) and 10330 nm (mid-infrared) were used for the extinction efficiencies.

Wavelength (nm)	n	k
488	1.550	1.0e-8
532	1.547	1.0e-8
10330	2.398	3.5e-2

Table 1. CSPEC sand refractive indices for the three wavelengths used in the library. The data is gathered from [17–20].

The particle material composition provides the refractive index. The complex index of refraction m is defined as:

$$m = n + ik \quad (1)$$

where n is the real component describing the phase velocity of light through the material, and the imaginary component k is the absorption coefficient. Table 1 shows the refractive indices for the three wavelengths used in the numerical calculations. The values are based on the optical properties of quartz found in the literature [17–20].

The calculated single particle scattering and extinction parameters are integrated using a log-normal size distribution, expressed as:

$$n(D) = \frac{1}{\sqrt{2\pi}D \ln \sigma} \exp \left[-\frac{1}{2 \ln(\sigma)^2} (\ln(D) - \ln(\bar{D}))^2 \right] \quad (2)$$

where \bar{D} is the mean diameter and σ is the geometric standard deviation or the distribution width. Since the typical size range for particles span several orders of magnitude, log-normal distributions are commonly used to describe particle size distributions. One of the more commonly used average is the Sauter mean diameter (SMD or D_{32}). The mean diameter and the SMD are related as:

$$\ln(\bar{D}) = \ln(D_{32}) - \frac{5}{2} (\ln(\sigma))^2 \quad (3)$$

The particle size distribution can then be described using only D_{32} and σ .

Table 2. Range of parameters included in the library.

Parameter	Values
D_{32} (μm)	1 - 1000
σ	1.2 - 1.8
Aspect Ratio (AR)	0.4 - 2.5

Table 2 shows the parameter ranges included in the library. Using 2000, 4, and 6 entries to discretize the ranges for D_{32} , σ , and AR , respectively, leads to a total number of 48000 entries in the library.

The integrations of the scattering and extinction parameters are performed as:

$$\overline{Q}_{ext}(\lambda_i, D_{32}, \sigma) = \frac{\int_0^\infty Q_{ext}(D, m)n(D, \sigma)D^2 dD}{\int_0^\infty n(D, \sigma)D^2 dD} \quad (4)$$

$$\overline{|S^2|}(D_{32}, \sigma, \theta) = \int_0^\infty |S^2|(D)n(D, \sigma, \theta)dD \quad (5)$$

The integrated quantities must then be formulated into the features that are measured by the sensor. The extinction efficiency between the two wavelengths are used to formulate the extinction ratio:

$$R_{ext,ij}(D_{32}, \sigma) = \frac{\tau_i}{\tau_j} = \frac{\overline{Q}_{ext}(\lambda_i, D_{32}, \sigma)}{\overline{Q}_{ext}(\lambda_j, D_{32}, \sigma)} \quad (6)$$

where τ and Q_{ext} are the measured and calculated extinction, respectively. The subscripts i and j correspond to $\lambda_i = 10330$ nm and $\lambda_j = 532$ nm.

The two intensity ratios are formed using the scattering intensity $\overline{|S^2|}$ from the three angular positions corresponding to the camera locations:

$$\frac{I_1}{I_3}(D_{32}, \sigma) = \frac{\overline{|S^2|}(D_{32}, \sigma, \theta_1)}{\overline{|S^2|}(D_{32}, \sigma, \theta_3)} \quad (7)$$

$$\frac{I_2}{I_3}(D_{32}, \sigma) = \frac{\overline{|S^2|}(D_{32}, \sigma, \theta_2)}{\overline{|S^2|}(D_{32}, \sigma, \theta_3)} \quad (8)$$

Corresponding to the three cameras used to measure the scattering intensity, the intensity from the largest scattering angle is used to normalize the other two views. This bypasses any need for calibration between incident laser power and camera settings.

2.2. Neural Network Model

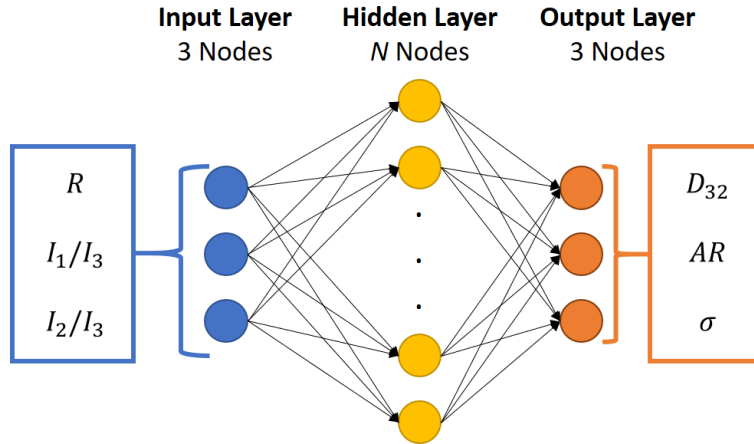


Fig. 2. Feedforward network structure for particle size, shape and distribution width estimation.

Feedforward neural networks are flexible tools that can be used for function approximations [21]. In this application, the neural network is used to approximate a function that takes in optical

measurements as inputs and estimates the particle parameters. Figure 2 shows a diagram of the neural network structure used for this purpose. This form consisting of an input layer, a single hidden layer, and an output layer is a universal functional approximator as long as the function is finite and there are enough neurons in the hidden layer [21, 22].

In a feedforward neural network, each neuron in a layer is connected to every neuron in the subsequent layer. Each connection has an associated weight, indicating how valuable the previous input is. All inputs from the previous layers are summed according to their weights and with the neuron's bias value. This sum is used to determine if the neuron will activate and pass an output to the next layer. The weights and biases are adjusted during neural network training. The number of weights and biases between two layers with N and M neurons are:

$$\gamma_{N \rightarrow M} = N \times M + M \quad (9)$$

Therefore, for the network structure shown in Figure 2 with three neurons in the input and output layers and N neurons in the hidden layer, the number of parameters to be optimized is expressed as:

$$\gamma_{total} = (3 \times N + N) + (N \times 3 + 3) = 7N + 3 \quad (10)$$

The training process is an optimization problem, where weights and biases are adjusted to minimize the error, evaluated using the training data. The number of neurons in the hidden layer affects how complex of a problem the neural network can approximate. However, increased number of neurons also increases the training complexity and can lead to increased error if the network is too large. In addition, the training process must be performed carefully to avoid overfitting the model to the training data.

There are numerous training schemes with their own set of advantages and disadvantages regarding training speed and accuracy. Bayesian regularization backpropagation was chosen to train the neural networks for particle characteristic estimation [21–24]. A detailed basis for Bayesian regularization can be found in the cited sources, but the main advantage of this method is that during the optimization processes, the magnitude of the parameters (weights and biases) is also minimized. If a connection or bias is unnecessary or detrimental for the model's accuracy, the value will converge to zero as the training scheme advances, effectively removing it from the network.

One of the outputs from the training process is the effective parameter (γ_{eff}), which indicates how many of the weights and biases are actively used in the trained model. After the training has concluded, if $\gamma_{eff} \approx \gamma_{total}$, the hidden layer may not be large enough and must be expanded until $\gamma_{eff} < \gamma_{total}$. The models are also trained multiple times to avoid any local minimums that might trap the optimization algorithm. In each training run, the initial weights and biases are randomized. The converged training errors and the effective parameters must be consistent throughout the training runs.

During the training process, networks with 10, 100, and 150 neurons in the hidden layer were trained three times each. The training scheme was considered to have converged when the gradient of the training mean squared error (MSE) reached 10^{-6} . The training MSE and γ_{eff} were monitored for each training run for consistency.

2.3. Experimental Setup

The optical mass loading sensor was tested in a wind tunnel seeded with CSPEC sand particles. The Virginia Tech High Speed Wind Tunnel (HSWT) is a suction tunnel driven by a Hoffman 75103 centrifugal blower. With a 6 inch diameter circular cross-section, the HSWT can reach up to $M = 0.5$. However, with a mesh filter installed to protect the blower from the large sand particles, the flow was throttled to $M = 0.37$. Figure 3a shows the overall layout of HSWT for the sand injection experiment.

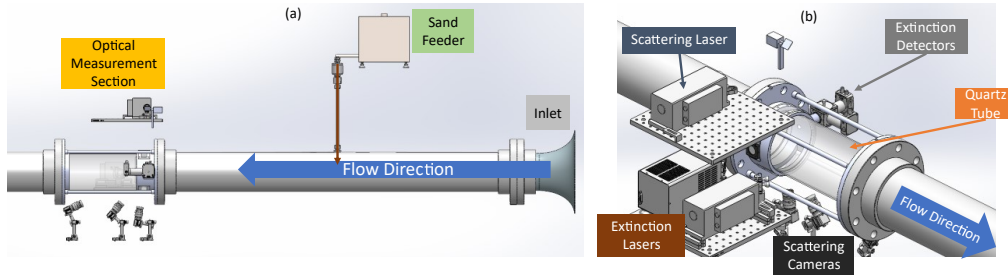


Fig. 3. (a) A schematic showing the wind tunnel layout, including the sand feeder and the optical measurement section. (b) A detailed view of the optical measurement section, with the extinction and scattering components labeled.

CSPEC sand gets its name from MIL-E-5007C specification, a US military specification for aircraft gas turbines [25]. This sample was chosen for its wide size range and material purity (99.9% crushed quartz), which allows for a more accurate refractive index to be used for populating the library.

Modifications were made to accommodate the mixed-phase flow within the tunnel. The sand is delivered by an AccuRate 106M feeder, which uses a continuously rotating helix to push sand into a feeding tube connected to the wind tunnel. The feeding tube into the tunnel was located 8 diameters downstream from the bellmouth inlet. The static pressure inside the tunnel provided enough suction to keep the sand flowing through the feeding tube. The particle mass flow rate is recorded by a scale (Ohaus Ranger 7000 with 2g readability) monitoring the weight of the sand feeder and hopper containing the CSPEC sand. During the experimental campaign, two different conditions (50% and 100% feed rate) were tested. Each condition was repeated five times while alternating for repeatability.

The optical measurements are made approximately 4 diameters downstream of the feeding tube. Figure 3b shows a closer look at the optical measurement section. A clear quartz tube and a 3D printed flange is used to provide optical access into the tunnel. Quartz was chosen over materials such as acrylic for its scratch resistance.

Figure 4 shows a top-down view of the extinction setup, with the scattering equipment hidden for clarity. A Gensis MX solid state laser and a ThorLabs MLQ MIR quantum cascade laser emit at 532 nm and 10330 nm, respectively. A Ge window, which transmits light in the infrared region but reflects in the visible wavelengths, is used to combine the two laser beams. BaF₂ windows provide optical access in and out of the wind tunnel. On the detector side, a Ge window is used once again to split the two beams. A 532 nm laser line filter and an achromatic lens is used to focus the visible laser onto the photodetector, a ThorLabs PDA100A. For the infrared laser, a Ge longpass filter and a ZnSe plano-convex lens is used to direct the beam into a ThorLab PDAVJ10 infrared photodetector. The photodetectors record the reduction in intensity at 100 kHz as the particles pass through the beam path.

Figure 5 shows a sample visible wavelength extinction dataset from the experiment. The incident intensity is reduced by the particles passing through the beam path and detected using a peak-detection algorithm. The incident and the reduced transmitted intensity are averaged and then used to calculate the measured extinction τ as:

$$\tau_i = -\ln\left(\frac{I_t}{I_0}\right) \quad (11)$$

where I_t and I_0 are the transmitted and incident intensities, respectively. The measured extinction for each wavelength are used to form the ratio of extinction per Eq. 6.

The scattering measurement section is shown in Figure 6. A Genesis MX laser emits a

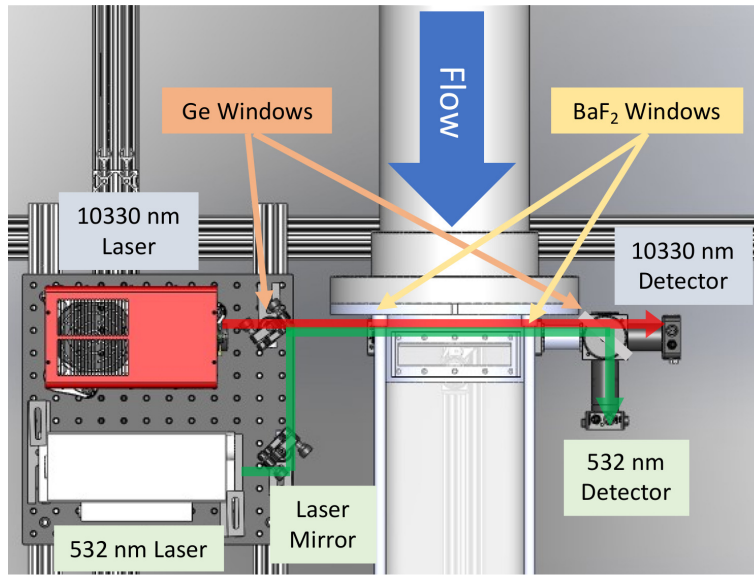


Fig. 4. A top view of the extinction setup, with the lasers located on the left and the detector components on the right. The green and red arrows indicate the paths for the 532 nm and 10330 nm laser beams, respectively.

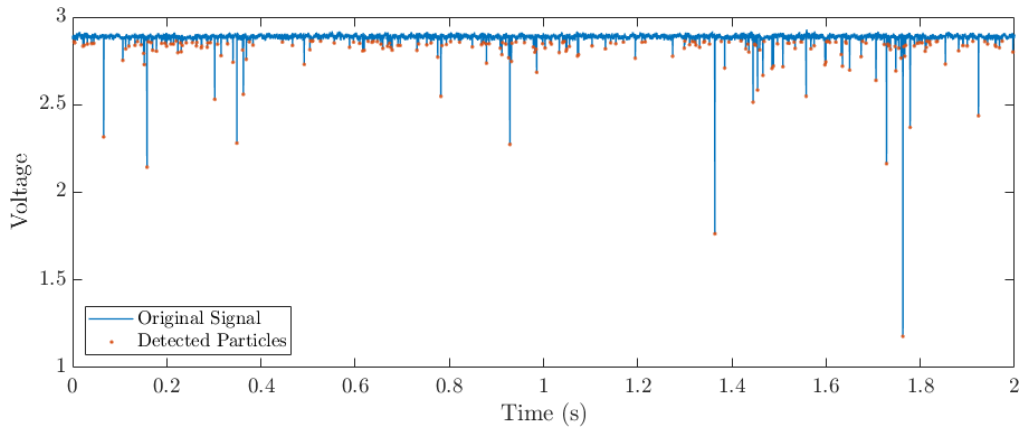


Fig. 5. A sample of the recorded extinction signal from the 532 nm detector. The detected minimums as the particles passing through the beam path are marked.

continuous beam at 488 nm. The beam is turned into a laser sheet through a General Scanning Inc. scanning mirror and introduced into the test section via clear acrylic panels in the flange. Three ThorLabs DCC3240M CMOS cameras located below the tunnel are used to acquire the particle scattering from the laser sheet.

A checkerboard pattern is used to spatially calibrate the cameras relative to the laser sheet plane. Images taken while the sand feeder is off are used as background for subtraction. A synchronized series of 500 images are taken from each camera during a run. Figure 7 shows a sample set of instantaneous images acquired during the experiment. The camera numbers at the top of the figure correspond to the layout shown in Figure 6b.

Images are first background-subtracted then warped to real world coordinates using the camera

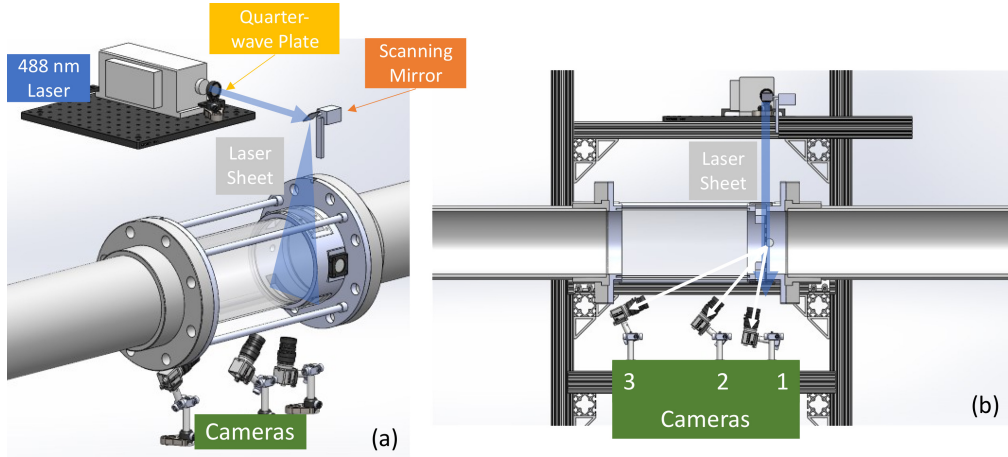


Fig. 6. (a) The scattering setup showing the laser source and the scanning mirror used to create the laser sheet. (b) A side view of the scattering setup showing the three cameras located below the wind tunnel.

calibration data. The edges are then dilated to aid in the binarization process, which converts the grayscale images to binary for particle detection. The binary images are then searched for particles that are visible from all three views, where their integrated intensity and angular locations are recorded and averaged for each run.

2.4. Mass Flow Estimation

To estimate the mass flow rate of the injected sand, an average particle volume and the particle count passing through the tunnel are used. The particle volume is calculated by converting the Sauter mean diameter into a volume moment diameter D_{43} :

$$D_{43} = \frac{\int_0^{\infty} n(D, \sigma) D^4 dD}{\int_0^{\infty} n(D, \sigma) D^3 dD} \quad (12)$$

where $n(D)$ is the size distribution defined by the neural network output D_{32} and σ . The average particle volume Vol_p is then calculated using D_{43} .

For the number density term, the reduced intensities recorded by the extinction detectors are used to count the particles passing through the beam path. Since the extinction beam path crosses through the center-line of the wind tunnel duct, the number of particles per second detected by the extinction lasers is scaled to the tunnel cross-sectional area using:

$$N_{p,total} = N_{p,ext} \frac{A_{duct}}{A_{beam}} \quad (13)$$

Where $N_{p,ext}$ and $N_{p,total}$ are the extinction and total particle counts per second, and A_{duct} and A_{beam} are the duct and extinction laser beam area. The mass flow is then estimated using:

$$\dot{m}_{sand} = N_{p,total} Vol_p \rho_p \quad (14)$$

where ρ_p is the sand particle density, which for quartz sand is 2600 kg/m^3 and Vol_p is the particle volume [26].

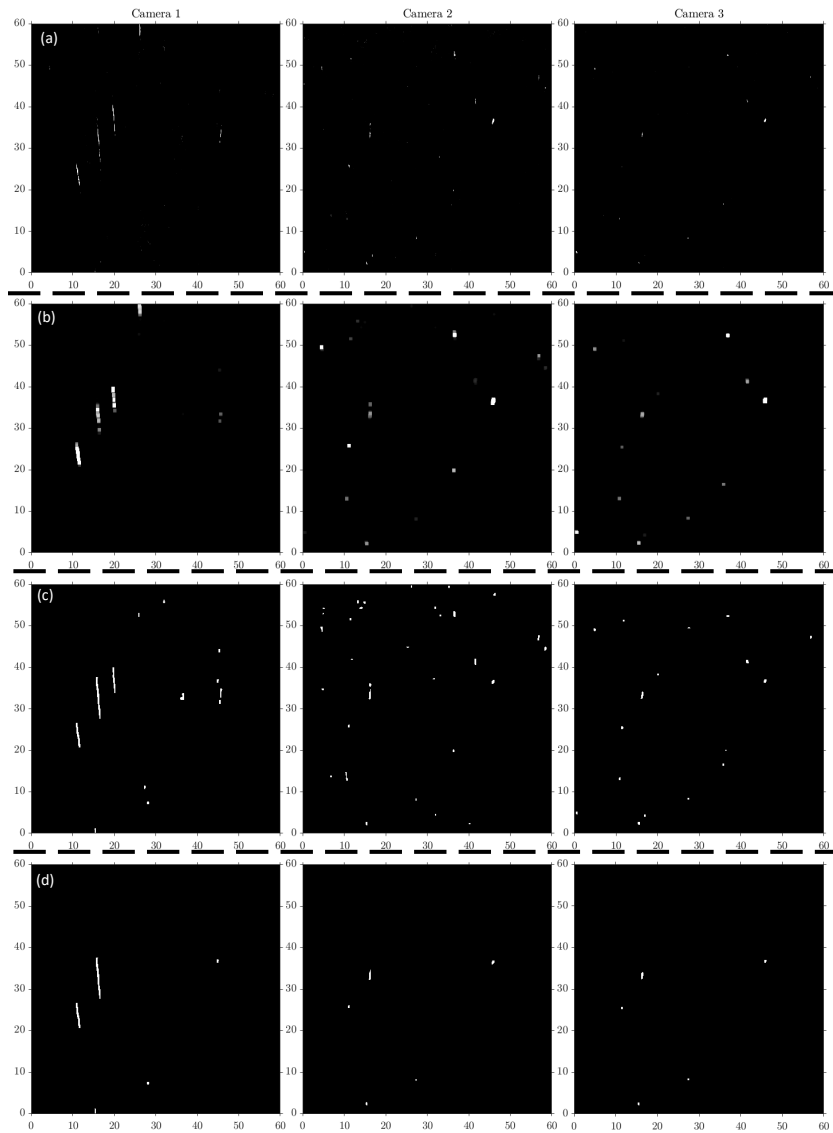


Fig. 7. A set of instantaneous scattering images captured by the three cameras. All spatial coordinates are in mm and the contrast has been adjusted to better highlight the particles. (a) Background-subtracted scattering images. (b) The grayscale images with the edges dilated for aiding edge detection. (c) Binarized images with gaps within particles filled. (d) Detected particles that are common in all three views.

2.5. Validation Methods

The estimated mass flow rate is validated against the sand mass flow rate monitored by the precision scale. For the particle size estimation, the sand sample were analyzed by three particle size analyzers: Sympatec HELOS, QICPIC, and Microtrac Camsizer X2 [27–29]. HELOS is a particle analyzer based on laser diffraction that is representative of conventional optical methods with spherical assumptions. QICPIC and Camsizer X2 use direct imaging to acquire the statistical shape and size of non-spherical particles. Scanning electron microscope (SEM) images of the CPEC sand were also acquired and analyzed for particle size. In addition, the vendor for the

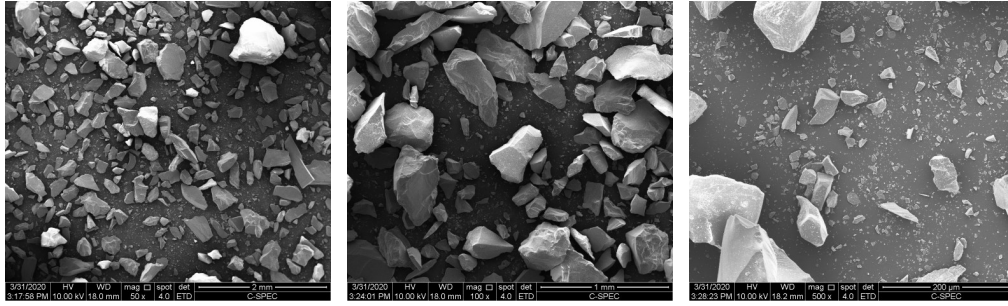


Fig. 8. SEM images of CSPEC sand at three different magnifications.

CSPEC sand (PTI) provided a size distribution measured using sieving.

The uncertainty in the mass flow estimation is affected by each of the terms in Eq. 14. However, only the input features (extinction and scattering) are directly measured. Following the procedures detailed in the previous work using this ML method, the uncertainty in the mass flow estimation is determined using the sensitivity to model outputs using simulated inputs and measurement (extinction and scattering) errors [12]. Additional error sources include the beam and duct area terms used to scale the particle count measurement, as well as the CSPEC sand density.

3. Results and Discussion

The scattering and extinction inputs are used as inputs for the trained models. In this section, the results of the model training procedures, the inputs measured from the experiments, and the output estimates from the model are presented. In addition, comparisons for the particle size and the sand mass flow rate estimations are made against the validation data.

3.1. Neural Network Training

Table 3. The results from the neural network training session for various numbers of neurons in the hidden layer and multiple training runs.

N	Training Run	Training MSE	γ_{total}	γ_{eff}
10	1	0.16	73	71
	2	0.13		69
	3	0.16		71
100	1	0.10	703	691
	2	0.11		686
	3	0.11		688
150	1	0.09	1053	936
	2	0.08		932
	3	0.08		894

Table 3 shows the training results for the various numbers of neurons in the hidden layer. For each N , the model was trained three times with randomized initial weights. The training

mean squared error (MSE) shows how well the final model predicted the training data. For $N = 10$ and 100 , the effective parameter γ_{eff} is within 95% of γ_{total} , meaning that the hidden layer is not large enough for this problem. Networks with $N = 150$, however, have γ_{eff} values converged to less than 90% of γ_{total} , providing confidence that the hidden layers are sufficiently complex to approximate the function described by the training data. The networks with $N = 150$ also show the lowest training error in Table 3. Therefore, for the particle parameter estimation, the three networks with $N = 150$ are used and their outputs are averaged.

3.2. Experimental Inputs

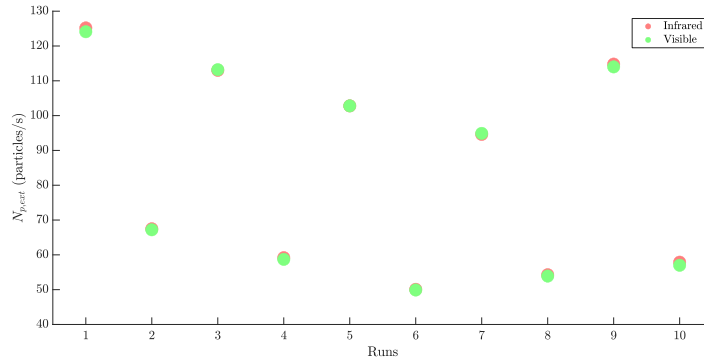


Fig. 9. The number of particles detected by the extinction detectors.

Figure 9 shows the results from the experimental extinction measurements. As the particles pass through the extinction laser beam paths, the attenuation from the incident intensity is recorded as extinction. Each dip in intensity is counted as a particle and the total number of detected particles is recorded. The particle count is divided by the length of time for each run (10 seconds) to get the $N_{p,ext}$ term from Eq. 13. The particle count from each wavelength converge for each run, giving confidence in the data analysis procedures. The attenuated intensity is used to calculate the measured extinction and then the ratio of extinction according to Eq. 6.

3.3. Neural Network Output

Using the measured extinction and scattering intensity ratios, the outputs (AR , σ , and D_{32}) from the trained neural network model are shown on Figure 10. As the same sand sample is injected throughout all the runs, these parameters are not expected to and do not vary for the different feed rates.

Table 4 shows the D_{32} estimations from the various validation sources. Three groups are discernible between the validation measurements. PTI vendor data via sieving and Microtrac - Min (size distribution created using the minimum lengths) group together, while the equivalent area measurements (QICPIC, Microtrac- Eq. Area, and SEM) estimates are similar. As the minimum length affects the particle's ability to pass through sieving filters, the agreement between the PTI and minimum length data are expected. The laser diffraction method (HELOS) and the Microtrac - Max (size distribution created using the maximum lengths) make up the third group. The neural network estimated values are between the minimum length and equivalent area measurements, suggesting that the trained neural network response is more sensitive to particle area and lengths, rather than volume. The particle size validation procedure shows that the measurement technique has a large influence on the resulting estimation, and that the traditional validation procedure against a "true" value is difficult for samples with such wide size distributions.

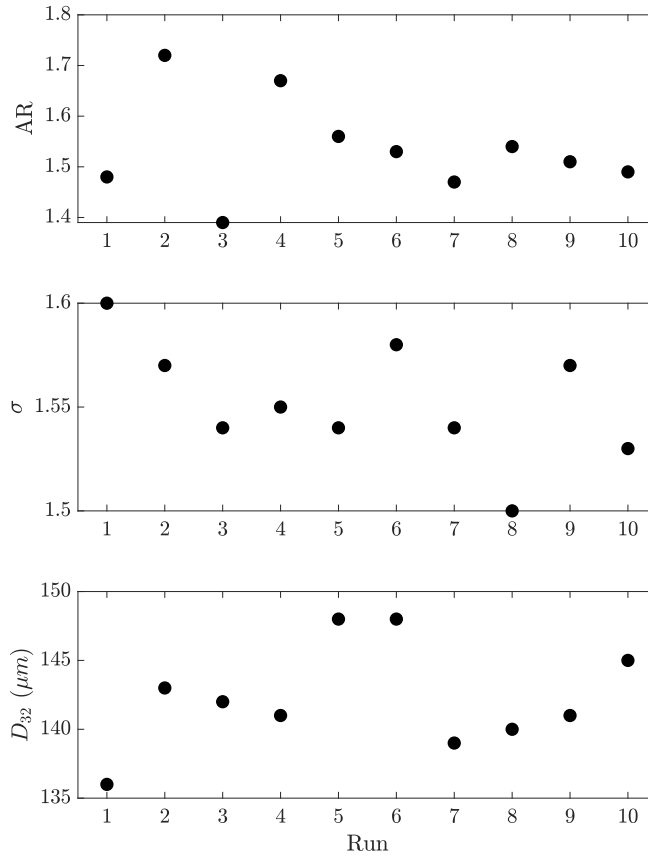


Fig. 10. The neural network outputs from each of the experimental runs.

Combining all three outputs from the neural network, the particle volume was calculated and the resulting sand mass flow rate was estimated using Eq. 14. Figure 11 shows the comparison between the estimated values (shown as ML) and the feed rate monitored using a precision scale. As stated from the previous section, the experiment alternated between 100% and 50% feed rates for each run. For both 50% and 100% feed rate runs, the machine learning approach slightly overestimates the \dot{m}_{sand} , with a root-mean-squared (RMS) error of 0.28 L/min or 4.1%. The estimated \dot{m}_{sand} accurately tracks the change in feed rate between the runs, confirming this method's versatility and repeatability.

A small but consistent overestimation across both feed rates implies a systemic, not a random source of error. The main suspected sources of this error are the neural network training and the mass flow estimation equation. The D_{32} entries in the library reach up to 1 mm, while the highest value measured by the validation sources reaches up to 200 μm . The additional library entries could be providing unnecessary data points that introduces biases in the neural network output during the training process. In addition, during the mass flow estimation, the exposed area of the extinction laser beams are used to scale the recorded particle count. This area is calculated based on the laser specs and the wind tunnel geometry. If the sand flow does not span from one side to the other due to boundary layers, this would affect the said scaling and the mass flow estimation. However, the consistent particle parameter and accurate mass flow estimations give credence to this machine learning approach to particle sensing.

Table 4. D_{32} estimations from the validation measurements and the ML approach.

Source	D_{32} (μm)
PTI	138
HELOS	191
QICPIC	162
Microtrac - Min	141
Microtrac - Eq. Area	165
Microtrac - Max	216
SEM	163
ML	142

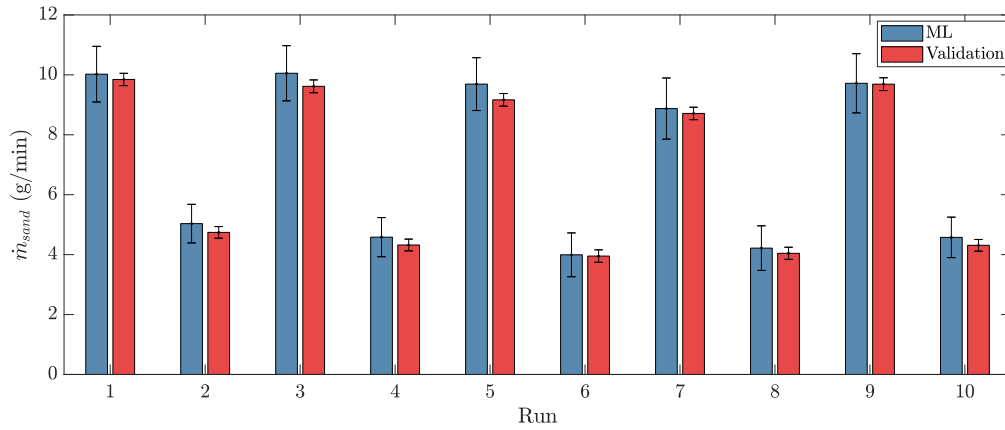


Fig. 11. Sand mass flow rate estimation using the ML approach and monitored values from the precision scale for validation.

4. Conclusion

A machine learning based particle characterization method was presented and demonstrated. The presented method relies on optical observations of light scattering and extinction by particles as input features to artificial neural networks. The models are trained on synthetic data, generated for particles that the sensor is likely to encounter.

A measurement of quartz sand injected into a wind tunnel was made for demonstrative purposes. The model provided consistent particle shape, size, and size distribution parameters that accurately measured the ingested sand mass flow rate with a RMS error of 0.28 L/min (4.1%) through five runs each at two different feed rate settings. This technique makes for an attractive particle remote sensing option due to the limited number of required observations. While many conventional particle measurement methods assume the particle shape to be spherical, the presented method provides non-spherical particle data to the models as the training basis.

The framework for this method could easily be modified, from the optical features used as inputs to the contents of the library for model training. Ice crystals and hail are major hazards for gas turbine operations. Various numerical tools and databases containing optical properties of ice crystals exist already, which could be adapted for this machine learning approach for

measurement and detection [30,31]. Additional features could be investigated for their feasibility as features. Optical modeling studies have revealed that quantities such as the depolarization ratio and back-scattering intensities contain significant information on dust particle shape and size. Improvements in the measurement technique could both simplify and add additional identifying features. We anticipate that some of these changes could further improve the presented measurement system.

Acknowledgments

The authors would like to thank Aditya Acharya, Eric Greenman, Bill Copenhaver, and Randall Monk for their assistance with the wind tunnel operations.

Disclosures

The authors declare no conflicts of interest.

References

1. M. B. Dolovich and R. Dhand, "Aerosol drug delivery: developments in device design and clinical use," *The Lancet* **377**, 1032–1045 (2011).
2. M. Elkoob, "Fuel atomization for spray modelling," *Prog. Energy Combust. Sci.* **8**, 61–91 (1982).
3. Y. Kaufman, D. Tanré, O. Dubovik, A. Karnieli, and L. Remer, "Absorption of sunlight by dust as inferred from satellite and ground-based remote sensing," *Geophys. Res. Lett.* **28**, 1479–1482 (2001).
4. V. R. Baker, "Terrestrial analogs, planetary geology, and the nature of geological reasoning," *Planet. Space Sci.* **95**, 5–10 (2014).
5. A. Hamed, W. C. Tabakoff, and R. Wenglarz, "Erosion and Deposition in Turbomachinery," *J. Propuls. Power* **22**, 350–360 (2006).
6. W. Chen and L. Zhao, "Review – Volcanic Ash and its Influence on Aircraft Engine Components," *Procedia Eng.* **99**, 795–803 (2015).
7. N. Bojdo, A. Filippone, B. Parkes, and R. Clarkson, "Aircraft engine dust ingestion following sand storms," *Aerosp. Sci. Technol.* **106**, 106072 (2020).
8. J. Potter and R. P. Tatam, "Optical condensation measurement in gas turbine engine inlets," in *Optical Technology in Fluid, Thermal, and Combustion Flow III*, vol. 3172 S. S. Cha, J. D. Trolinger, and M. Kawahashi, eds. (1997), pp. 422–433.
9. C. A. Wood, S. L. Slater, M. Zonneveldt, J. Thornton, N. Armstrong, and R. A. Antoniou, "Characterisation of Dirt, Dust and Volcanic Ash: A Study on the Potential for Gas Turbine Engine Degradation," *Tech. rep.* (2017).
10. M. G. Dunn, "Operation of Gas Turbine Engines in an Environment Contaminated With Volcanic Ash," *J. Turbomach.* **134**, 051001 (2012).
11. C. Y. Moon, A. Gargiulo, G. Byun, and K. Todd Lowe, "Non-spherical particle size estimation using supervised machine learning," *Appl. Opt.* **59**, 3237–3245 (2020).
12. C. Y. Moon, A. Panda, G. Byun, C. F. Smith, and K. T. Lowe, "Non-intrusive optical measurements of gas turbine engine inlet condensation using machine learning," *Meas. Sci. Technol.* (2020).
13. P. Yang, Q. Feng, G. Hong, G. W. Kattawar, W. J. Wiscombe, M. I. Mishchenko, O. Dubovik, I. Laszlo, and I. N. Sokolik, "Modeling of the scattering and radiative properties of nonspherical dust-like aerosols," *J. Aerosol Sci.* **38**, 995–1014 (2007).
14. Z. Meng, P. Yang, G. W. Kattawar, L. Bi, K. N. Liou, and I. Laszlo, "Single-scattering properties of tri-axial ellipsoidal mineral dust aerosols: A database for application to radiative transfer calculations," *J. Aerosol Sci.* **41**, 501–512 (2010).
15. J. M. Conny, R. D. Willis, and D. L. Ortiz-Montalvo, "Optical Modeling of Single Asian Dust and Marine Air Particles: A Comparison with Geometric Particle Shapes for Remote Sensing," *J. Quant. Spectrosc. Radiat. Transf.* **254**, 107197 (2020).
16. T. Nousiainen, "Optical modeling of mineral dust particles: A review," *J. Quant. Spectrosc. Radiat. Transf.* **110**, 1261–1279 (2009).
17. J. T. Peterson and J. A. Weinman, "Optical Properties of Quartz Dust Particles at Infrared Wavelengths," *J. Geophys. Res.* **74**, 6947–6952 (1969).
18. D. R. Longtin, E. P. Shettle, J. R. Hummel, and J. D. Pryce, "A Wind Dependent Desert Aerosol Dust Model: Radiative Properties," *Tech. rep.* (1988).
19. G. Ghosh, "Dispersion-equation coefficients for the refractive index and birefringence of calcite and quartz crystals," *Opt. communications* **163**, 95–102 (1999).
20. A. Miffre, T. Mehri, M. Francis, and P. Rairoux, "UV-VIS depolarization from Arizona Test Dust particles at exact backscattering angle," *J. Quant. Spectrosc. Radiat. Transf.* **169**, 79–90 (2016).

21. M. T. Hagan, H. B. Demuth, M. H. Beale, and O. De Jesús, *Neural Network Design* (PWS Publishing Co., 1997), 2nd ed.
22. T. Hastie, R. Tibshirani, and J. Friedman, *The Elements of Statistical Learning*, Springer Series in Statistics (Springer New York, New York, NY, 2009).
23. D. J. MacKay, "Bayesian interpolation," *Neural computation* **4**, 415–447 (1992).
24. D. J. MacKay, "A practical bayesian framework for backpropagation networks," *Neural computation* **4**, 448–472 (1992).
25. Powder Technology Inc., "MIL E-5007 AND MIL-AV-E-8593F," <https://www.powdertechologyinc.com/product/mil-e-5007/>.
26. Powder Technology Inc., "Quartz Dust/Sand Safety Data Sheet," <https://www.powdertechologyinc.com/wp-content/uploads/2020/07/SDS.Quartz.6-April-2020.pdf>.
27. Sympatec GmbH, "HELOS," <https://www.sympatec.com/en/particle-measurement/sensors/laser-diffraction/helos/>.
28. Sympatec GmbH, "QICPIC," <https://www.sympatec.com/en/particle-measurement/sensors/dynamic-image-analysis/qicpic/>.
29. Microtrac, "CAMSIZER X2," <https://www.microtrac.com/products/particle-size-shape-analysis/dynamic-image-analysis/camsizer-x2/function-features/>.
30. L. Bi, "Light scattering by ice crystals and mineral dust aerosols in the atmosphere," Ph.D. thesis, Texas A & M University (2012).
31. P. Yang, L. Bi, B. A. Baum, K. N. Liou, G. W. Kattawar, M. I. Mishchenko, and B. Cole, "Spectrally consistent scattering, absorption, and polarization properties of atmospheric ice crystals at wavelengths from 0.2 to 100 μm ," *J. Atmospheric Sci.* **70**, 330–347 (2013).

6. The Particle Scattering and Extinction Library

6.1 Introduction

The scattering and extinction library is used to train the machine learning models for particle parameter estimation. The scattering and extinction values of likely-encountered particles are calculated and organized into a database for model training. This provides the numerical basis formulated by the physics behind particle-light interaction.

While they may be used for different purposes, similar databases can be found in the literature. The Amsterdam & Grenada Light Scattering database contains the measured phase functions of dust, sand, and volcanic ash particles, as well as size distribution estimations using a laser diffraction particle sizer [1]. Another database for optical modeling of minerals was compiled by Meng et al. [2]. This database contains the single scattering data for ellipsoids from ultraviolet (UV) to far-infrared (IR) wavelengths. The database is parameterized using 42 aspect ratios, 69 refractive indices, and 471 size parameters. Users can use interpolation for values within this design space. The single scattering data was calculated using an array of numerical tools, including discrete dipole approximation, T-matrix method, and a geometric optics method.

The scattering and absorption properties of ice crystals are important for atmospheric science research. Yang et al. has compiled multiple ice crystal scattering databases, for a very wide range of sizes, wavelengths, and complex shapes [3, 4]. The non-spherical crystal shapes (such as aggregates, hexagonal columns, droxtals, and more) are based on observations. The most recent version of the database is focused from the near to far IR regions (3 to 100 μm) and particle lengths ranging from 2 to 10,000 μm .

In this chapter, an overview of the particle parameters and numerical tools used to populate the scattering and extinction library is presented. In addition, the contents of the library generated for CSPEC sand measurements and related discussions follows.

6.2 Methods

6.2.1 Library Parameters

Particle Size Distributions

One of the most important particle parameters for this application is size. However, particles in-reality seldom exist as a single uniform size (monodisperse). Instead, the particle size has a range and densities corresponding to the sizes. Distributions are commonly used to approximate the size variety present in a cloud of particles. Density distributions can be constructed based on number, length, area, and volume, though the length density is rarely used. A common nomenclature for density distributions is to use q_i with the subscript indicating the base: 0 for number, 1 for length, 2 for area, and 3 for volume. The diameter or radius is usually used for defining the discretized size bins, and the diameter is used throughout this chapter for consistency. For non-spherical particles, the equivalent-volume-sphere diameter is used to define the size bins. For spherical particle distributions, the following expression can be used to convert between the different bases:

$$q_r(D) = \frac{D^{(r-t)} q_t(D)}{\int_0^\infty D^{(r-t)} q_t(D) dD} \quad (6.1)$$

where q_t and t indicate the density distribution and its corresponding subscript to be converted, and q_r and r describes converted the distribution and the corresponding subscript. For example, to convert from a number density distribution q_0 to a volume density distribution q_3 , Eq. 6.1 is used with $t = 0$ and $r = 3$.

Statistical distributions are used to model particle density distributions. Some of the commonly used distributions for describing particle number density distributions are normal, log-normal, gamma, power-law, and Rosin-Rammler distributions. Only the log-normal distribution will be detailed here, but the cited sources can be used as references for the other distributions [5, 6].

The log-normal distribution is commonly used because a typical cloud of particles has sizes ranging several orders of magnitude. A log-normal number density distribution is expressed as:

$$q_0(\text{log-normal}) = \frac{1}{\ln \sigma \sqrt{2\pi} D} \exp - \frac{\ln D - \ln \bar{D}}{2 \ln \sigma^2} \quad (6.2)$$

where σ is the geometric standard deviation (or also known as the distribution width), and \bar{D} is the mean diameter. 95% of all particles described by the distribution is between the size ranges of

$\bar{D}/2\sigma$ to $\bar{D}2\sigma$. When σ is 1, the distribution is monodisperse. Typical aerosol distributions have a σ range from 1.5 to 2.0 [5]. A unique property of the log-normal distribution is that the converted area and volume density distributions will have the same standard deviation.

There are various different ways to describe a particle size distribution using averages. One of the more commonly used average is the Sauter mean diameter (SMD or D_{32}). Sometimes referred as the surface-volume mean diameter or twice the value of effective radius r_e (commonly used in atmospheric sciences), the SMD is the diameter of a sphere with the same volume to surface area ratio as the particle distribution. From the number density distribution, SMD can be calculated as:

$$D_{32} = \frac{\int_0^{\infty} D^3 q_0 dD}{\int_0^{\infty} D^2 q_0 dD} \quad (6.3)$$

The mean diameter and the SMD are related as:

$$\ln(\bar{D}) = \ln(D_{32}) - \frac{5}{2}(\ln(\sigma))^2 \quad (6.4)$$

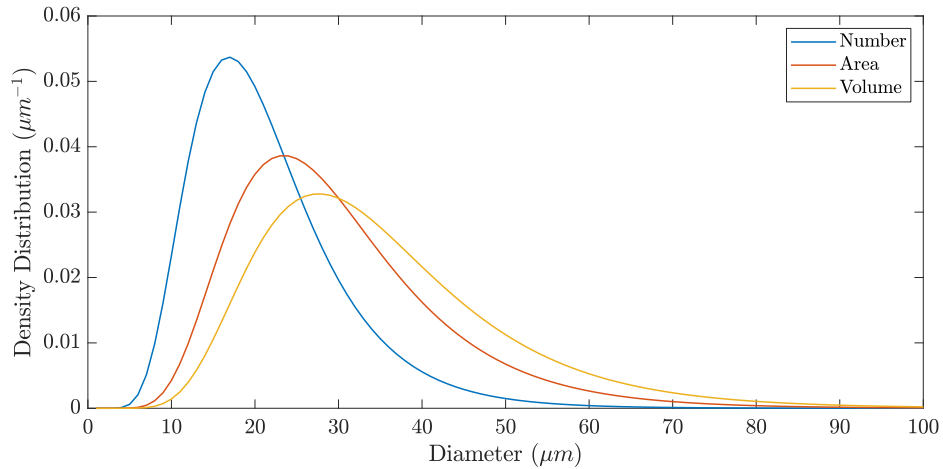


Figure 6.1: Number, area, and volume density distribution for a log-normal distribution with $D_{32} = 30 \mu m$, $\sigma = 1.5$.

Figure 6.1 shows the number, area, and volume density distributions using a log-normal distribution with an arbitrarily shown SMD and σ . It is important to note that all three density distributions are describing the same group of particles. In the latest iteration of the library (as described in Chapter 5), the particle size range from $1 \mu m$ to $1,000 \mu m$ is parameterized using 2000 entries linearly distributed, and σ ranges from 1.2 to 1.8 using 4 linearly distributed entries. This means that for a single shape in the library, there are 8,000 entries describing various the particle sizes

and distribution widths.

The unpolarized scattering intensity $|S^2|$ and extinction efficiency Q_{ext} are first calculated for a single particle of a particular size. The library entries must then be integrated using size distribution functions to calculate the mean scattering and extinction parameters for that size distribution. The extinction efficiency is integrated using:

$$\overline{Q}_{ext}(\lambda_i, D, \sigma) = \frac{\int_0^\infty Q_{ext}(x, m) q_0(D, \sigma) D^2 dD}{\int_0^\infty q_0(D, \sigma) D^2 dD} \quad (6.5)$$

The scattering profile is integrated using:

$$\overline{|S^2|}(D, \sigma) = \int_0^\infty |S^2|(D) q_0(D, \sigma) dD \quad (6.6)$$

The extinction ratio is found by taking the ratio of mean extinction efficiencies at two different wavelengths:

$$R_{ext,ij} = \frac{\tau_i}{\tau_j} = \frac{\overline{Q}_{ext}(\lambda_i, D, \sigma)}{\overline{Q}_{ext}(\lambda_j, D, \sigma)} \quad (6.7)$$

The particle library for CSPEC sand is generated using incident wavelengths of 488 nm for scattering and 532 nm and 10330 nm for extinction.

Particle Shape

The target particles for this sensor application, such as sand and volcanic ash, have very complex and irregular shapes. It is impractical to measure, define, and calculate the scattering parameters for those irregular shapes. Therefore, the particle shape must be modeled using surrogates.

While simpler shapes would make the simulation process easier, the chosen shape must be complex enough to accurately model the particle-light interaction. Yang et al. conducted a study using spheroids and spheres for atmospheric dust observations [7]. As expected, the effects of nonsphericity was found to be significant for dust particles in the visible wavelength region.

Increasing the degree of freedom by one, spheroids are often used for dust modeling. Beginning with the equation describing a general ellipsoid shown in Figure 6.2:

$$\frac{x^2}{a^2} + \frac{y^2}{b^2} + \frac{z^2}{c^2} = 1 \quad (6.8)$$

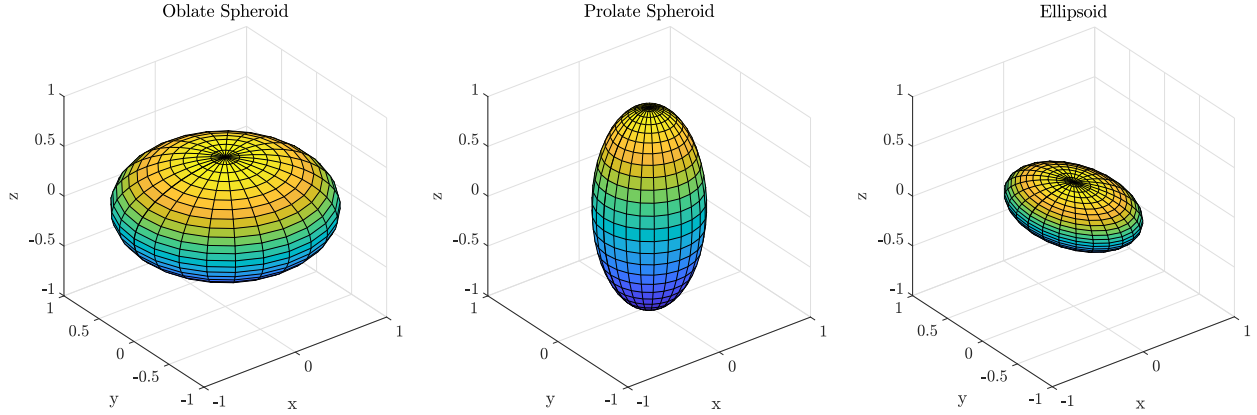


Figure 6.2: An example of an oblate spheroid, a prolate spheroid, and an ellipsoid.

In addition to the overall size (using an equivalent area or volume sphere diameter), the aspect ratios a/c and b/c describe the ellipsoid shape. A special case of ellipsoids, spheroids are ellipsoids with one axis as a symmetric axis. Making the z axis as the symmetric axis, spheroids can be described using:

$$\frac{x^2 + y^2}{a^2} + \frac{z^2}{c^2} = 1 \quad (6.9)$$

The spheroid can then be defined with an overall size and one aspect ratio, $AR = a/c$. Prolate spheroids have $AR > 1$ while oblate spheroids have $AR < 1$. The surface area of the spheroid is given as:

$$\begin{aligned} \text{(Oblate Spheroids)} \quad S &= 2\pi a^2 + \pi \frac{c^2}{\epsilon^2} \ln \left(\frac{1 + \epsilon}{1 - \epsilon} \right), \quad \epsilon^2 = 1 - \frac{c^2}{a^2} \\ \text{(Prolate Spheroids)} \quad S &= 2\pi a^2 + 2\pi \frac{ac}{\epsilon} \arcsin \epsilon, \quad \epsilon^2 = 1 - \frac{a^2}{c^2} \end{aligned} \quad (6.10)$$

As the particles flow past the laser beam, their orientations are expected to be random. Therefore, the scattering and extinction parameters for non-spherical shapes are averaged for random orientations. The projected area A for randomly oriented spheroids are simply $A = S/4$ [8].

To parameterize the aspect ratio, the shape parameter ξ proposed by Kahnert et al. is used for an linearly-spaced AR distribution[9]. This is due to the fact that for prolate spheroids, linearly increasing a also increases AR linearly. However, for oblate spheroids, linearly increasing c

decreases AR hyperbolically. Therefore, ξ allows for a linear shape parameter and is defined as:

$$\begin{aligned}\xi &= \frac{1}{AR} - 1 \text{ (Oblate Spheroid)} \\ \xi &= 1 - AR \text{ (Prolate Spheroid)} \\ \xi &= 0 \text{ (Sphere)}\end{aligned}\tag{6.11}$$

In the library created for CSPEC sand estimations, ξ ranges from -1.5 to 1.5 in six increments, equating to aspect ratios of 0.4, 0.5, 0.67, 1.5, 2, and 2.5. Combined with the particle size and distribution, the total number of entries in the CSPEC sand library is 48,000.

Numerous studies have been conducted to evaluate the effectiveness of spheroids and ellipsoids as dust particle surrogates [2, 10, 11, 12, 13, 14, 15]. Scattering data from spheroids and ellipsoids were fitted to measured dust quantities. Spheroids perform very well, except in one area: the polarization ratio, which describes the scattering power between the two linear polarization direction [14]. Due to this fact, the scattering parameters for the CSPEC sand library were calculated for unpolarized light, and measurements were made using circularly polarized light.

Particle Refractive Index

Wavelength (μm)	Real	Imaginary
0.488	1.550	1e-8
0.532	1.547	1e-8
10.33	2.398	3.5e-2

Table 6.1: CSPEC sand refractive indices for the three wavelengths used in the library. The data is gathered from [16, 17, 18, 19].

The particle's material composition affects its interaction with light via the refractive index. It is expressed as:

$$m = n + ik\tag{6.12}$$

where n is the real component describing how fast light travels through the material and k is the absorption coefficient that describes how much light is absorbed by the material. The refractive index is also dependent on the wavelength of the incident light. CSPEC sand is pure crushed quartz. Table 6.1 contains the CSPEC refractive indices for the three wavelengths used to calculate the scattering and extinction parameters in the library.

6.2.2 Numerical Methods

Multiple numerical methods are necessary to cover the wide range of particle sizes. The size parameter x is used to define the particle size relative to the incident wavelength:

$$x = \frac{\pi D}{\lambda} \quad (6.13)$$

Where D is a characteristic length of the particle (usually the equivalent volume or area sphere diameter) and λ is the wavelength. x determines which scattering regime the light-particle interaction belongs to and the corresponding numerical tool.

Rayleigh scattering regime refers to when the particle is much smaller than the light wavelength ($x \ll 1$) [20, 21]. The scattered intensity is proportional to the fourth power of particle size and inversely proportional to the sixth power of the wavelength. For particles with sizes similar to the wavelength ($x \approx 1$), the scattering regime is commonly referred as Mie scattering, with its name derived from Mie theory or solution. Mie theory only describes the scattering by a sphere, but Mie scattering regime includes all particle shapes and many other solution techniques. Geometric optics scattering regime occurs as the particle gets larger ($x \gg 1$). This scattering regime is named after the geometric optics approximation. Instead of solving Maxwell's equation for electromagnetic wave propagation, geometric optics uses rays to describe the propagation of light. In the particle library, the typical size ranges of sand and dust particles means that only the Mie and geometric optics regimes are considered. For sand particles modeled as spheroids, a T-matrix code (*SMARTIES*) and a ray-tracing code by Macke et al. were used for small and large size parameters, respectively [22, 23].

The T-matrix method allows for the scattering property calculations of any arbitrary shape [24]. A detailed mathematical formulation of the T-matrix method are described in the cited references [22, 24, 25, 26, 27, 28]. The main advantage of the T-matrix method is that a single calculation of the T-matrix for a given particle shape, size, and refractive index is valid for any orientation, making the calculation of randomly oriented scattering parameters very efficient [24]. T-matrix results are also analytical or exact, meaning that no approximations are used, as opposed to the ray-tracing method.

Detailed explanations for the ray-tracing method for the code suite are presented in the cited references [29, 30]. A ray is introduced at a particle with a given shape, orientation, size, and complex refractive index. At every intersection between the ray and the surface of the particle, the

new ray direction is determined by the reflection-refraction equations, and portions of the ray's Stoke vector energy is absorbed according to the the absorption coefficient. This process is continued until the ray is scattered out or the energy reaches 10^{-6} of its initial value, then repeated for a set number of rays. Since geometric optics assumption negates effects such as diffraction and interference, the method presented by Macke et al. adds the effects of diffraction using its far-field assumption. The diffraction terms are calculated using Fraunhofer diffraction equations and the particle's projected cross-sectional area [21]. The resulting phase function is the sum of ray-tracing and diffraction terms.

During the library population process, *SMARTIES* is used the algorithm fails to achieve numerical convergence. From that size parameter and larger, the ray-tracing code is then used for calculations. Using the two different tools, the outputs must be standardized to be used together. *SMARTIES*'s output is a normalized scattering matrix F , while the ray-tracing code uses the phase function P . For converting *SMARTIES*'s output to an unpolarized scattering intensity $|S^2|$:

$$|S^2| = \frac{x^2}{2} F_{11} \quad (6.14)$$

where x is the particle size parameter calculated using the equivalent volume sphere diameter. To get the same quantity from the ray-tracing output:

$$|S^2| = P_{11} \frac{\pi C_{sca}}{\lambda^2} \quad (6.15)$$

where C_{sca} is the scattering cross-section and λ is the incident wavelength.

The switch between *SMARTIES* and the ray-tracing code occurred around $x \approx 50$, depending on the particle shape and the incident wavelength. Since ray-tracing involves the geometric optics assumptions, the transition region between the ray-tracing code and *SMARTIES* was examined for any errors associated with those assumptions. The scattering parameters in this region by the ray-tracing code were closely examined against exact methods and found to be accurate [23]. The extinction efficiency was tested independently.

Figure 6.3 shows the extinction efficiencies calculated for spheres using *SMARTIES*, ray-tracing code, and MatScat, a Mie theory program [31]. Mie theory provides the exact solutions for spherical particle scattering, and its output is used to confirm the analytical solution provided by *SMARTIES*. The extinction efficiency shown in Figure 6.3 relates to single particles, not the integrated quantity for a particle size distribution. It shows where the switch from *SMARTIES* to

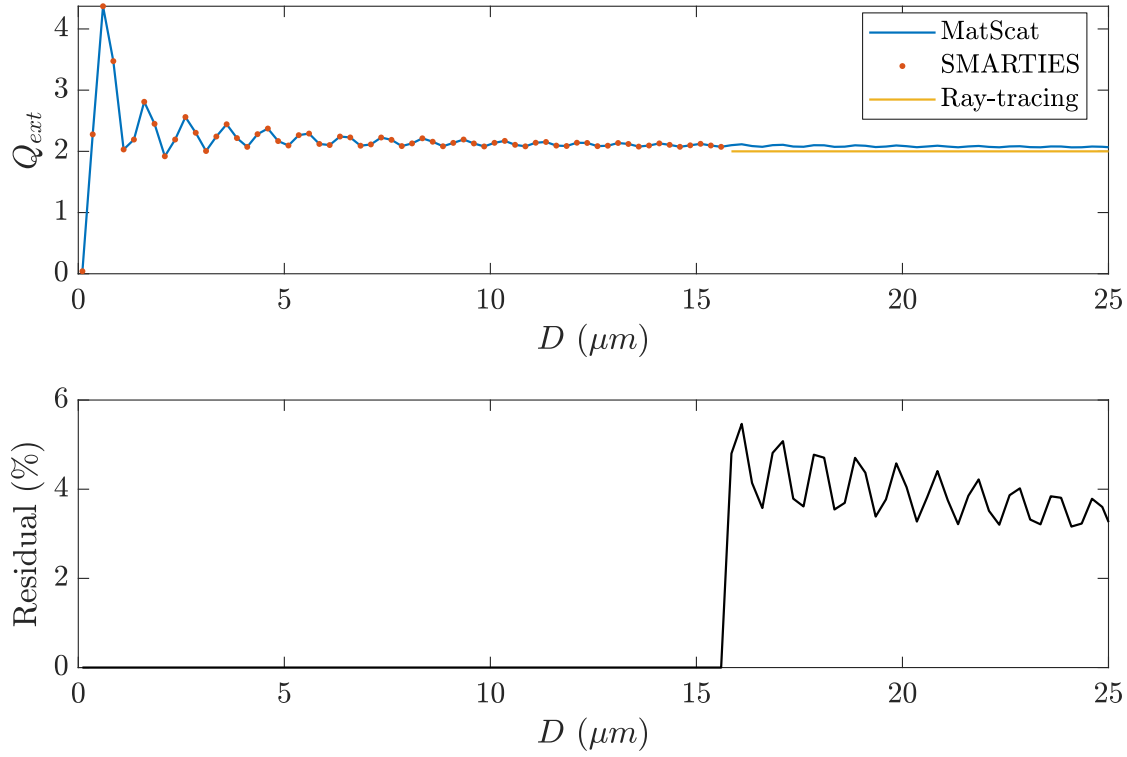


Figure 6.3: Extinction efficiencies calculated with three different numerical schemes for spheres of various sizes and an incident wavelength of 532 nm .

ray-tracing, near $D = 15$, which corresponds to $x \approx 90$ with $\lambda = 532 \text{ nm}$.

Figure 6.4 shows the comparison of the integrated mean extinction ratios of spheres calculated using only the exact solution provided by Mie theory against the combination of *SMARTIES* and ray-tracing, as well as the relative error between them. The largest error occurs for size distributions with small mean diameters, near $D_{32} \approx 2 \mu m$, and the error then converges to around 1.5% as D_{32} increases.

6.3 Library Contents

In this section, the extinction ratio and scattering profiles calculated for the CSPEC sand library are presented. All the parameter ranges (particle size, distribution width, shape, incident wavelength, and the corresponding refractive index) are as detailed in the previous section. The resulting trends from varying the particle parameters are also discussed.

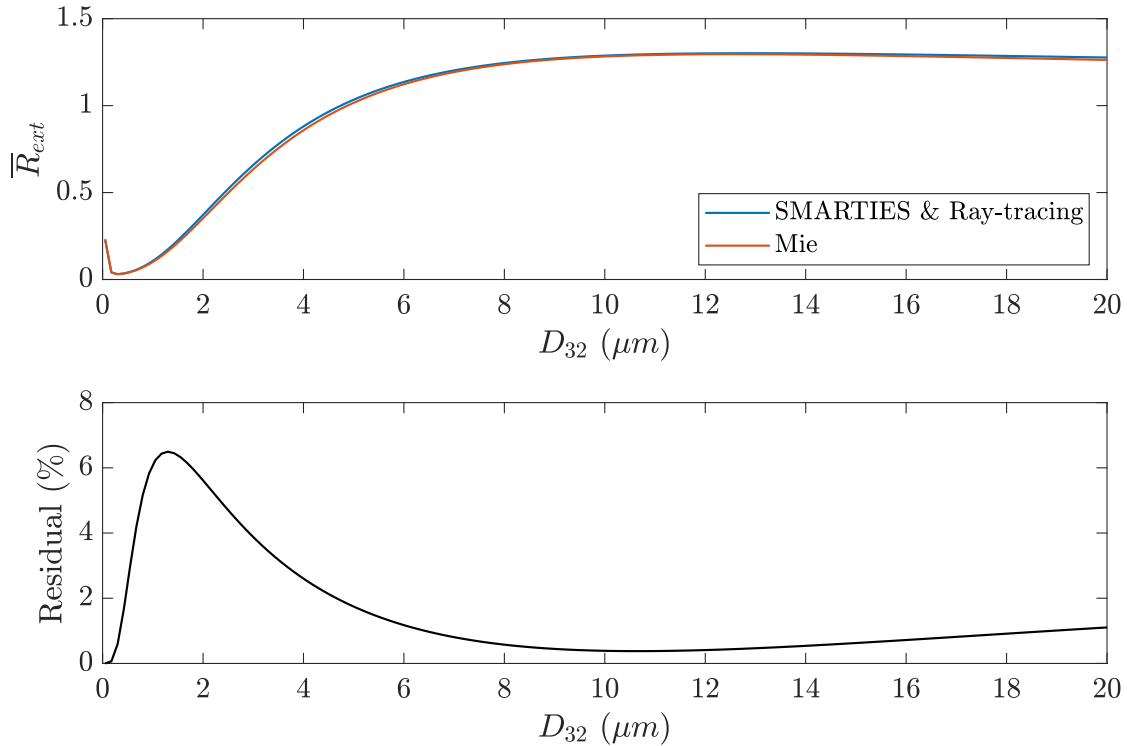


Figure 6.4: Mean efficiency ratio profiles calculated using *SMARTIES*, ray-tracing, and MatScat.

6.3.1 Extinction Ratio

Figure 6.5 shows the calculated ratio of extinction R included in the CSPEC sand library. As the Sauter mean diameter increases, all profiles converge to a value of 1. Geometric optics limit states that $\lim_{x \rightarrow \infty} Q_{ext} = 2$. The extinction ratio dependencies on particle shape and distribution widths are also shown in Figure 6.5.

As the aspect ratio deviates from 1, the peak extinction ratio values near $D_{32} \approx 5 \mu m$ also increase, with the $AR = 0.4$ case being the only exception. In addition, as the particle shape becomes more spherical, the different profiles for varying σ converge to $R = 1$ quicker. Throughout all aspect ratios, increased size distribution σ increases R for $D_{32} \leq 10 \mu m$ and decreases for $D_{32} \geq 10 \mu m$. Increased σ also accelerates the convergence to $R = 1$ as the particle size increases.

6.3.2 Scattering Intensities

Figure 6.6 shows the shape and Sauter mean diameter behaviors for the scattering profiles. The peak intensity in the forward scattering region increases exponentially as the Sauter mean diameter

increases. The low intensity zones, sometimes called the Alexander's dark band and the basis for visible rainbows in the atmosphere, can also be seen for the spheroid particles modeled here [25]. The location and the depth of these bands vary from shape to shape, but not for difference sizes (except in the Rayleigh scattering limit as x approaches 0). The band locations due to external reflections, which explains the shape, but not size dependency.

Figure 6.7 shows the scattering profiles for a constant SMD and shape, but varying σ . The low intensity band can still be observed here, between 90° and 110° . This again shows the shape dependency of the dark band location. The forward scattering region is insensitive to the distribution width, but variations due to the distribution width can be seen everywhere else.. This supports the intensity ratio feature approach with two forward scattering intensities normalized by a side scattering angle.

6.4 Conclusions

In this chapter, the particle characteristics that define the library, the numerical tools, and the resulting scattering and extinction library are presented. Previous studies supported the use of spheroids for modeling sand particles, as long as the unpolarized measurements are used. The resulting extinction ratio and scattering profiles showed their size, shape, and size distribution width dependencies. While only the CSPEC library was shown, the methods used to generate it can be adapted to other particles, dependent on the requirements. Additional research into shape modeling and the refractive index must be done if the new material significantly deviates from properties of sand and dust.

References

- [1] O. Muñoz, F. Moreno, D. Guirado, D. Dabrowska, H. Volten, and J. Hovenier, "The Amsterdam–Granada Light Scattering Database," *Journal of Quantitative Spectroscopy and Radiative Transfer*, vol. 113, no. 7, pp. 565–574, May 2012.
- [2] Z. Meng, P. Yang, G. W. Kattawar, L. Bi, K. N. Liou, and I. Laszlo, "Single-scattering properties of tri-axial ellipsoidal mineral dust aerosols: A database for application to radiative transfer calculations," *Journal of Aerosol Science*, vol. 41, no. 5, pp. 501–512, 2010. [Online]. Available: <http://dx.doi.org/10.1016/j.jaerosci.2010.02.008>
- [3] P. Yang and K. Liou, "Single-scattering properties of complex ice crystals in terrestrial atmo-

- sphere,” *Beitrage zur Physik der Atmosphere-Contributions to Atmospheric Physics*, vol. 71, no. 2, pp. 223–248, 1998.
- [4] P. Yang, H. Wei, H.-L. Huang, B. A. Baum, Y. X. Hu, G. W. Kattawar, M. I. Mishchenko, and Q. Fu, “Scattering and absorption property database for nonspherical ice particles in the near-through far-infrared spectral region,” *Applied optics*, vol. 44, no. 26, pp. 5512–5523, 2005.
- [5] R. G. Grainger, “Some useful formulae for aerosol size distributions and optical properties,” *Lect. Notes (University of Oxford)*, 2012.
- [6] T. Allen, *Particle Size Measurement*. Springer, 1990. [Online]. Available: <http://link.springer.com/10.1007/978-94-009-0417-0>
- [7] P. Yang, Q. Feng, G. Hong, G. W. Kattawar, W. J. Wiscombe, M. I. Mishchenko, O. Dubovik, I. Laszlo, and I. N. Sokolik, “Modeling of the scattering and radiative properties of nonspherical dust-like aerosols,” *Journal of Aerosol Science*, vol. 38, no. 10, pp. 995–1014, 2007.
- [8] V. Vouk, “Projected area of convex bodies,” *Nature*, vol. 162, no. 4113, pp. 330–331, 1948.
- [9] F. M. Kahnert, J. J. Stamnes, and K. Stamnes, “Can simple particle shapes be used to model scalar optical properties of an ensemble of wavelength-sized particles with complex shapes?” *JOSA A*, vol. 19, no. 3, pp. 521–531, 2002.
- [10] T. Nousiainen, “Optical modeling of mineral dust particles: A review,” *Journal of Quantitative Spectroscopy and Radiative Transfer*, vol. 110, no. 14-16, pp. 1261–1279, Sep. 2009. [Online]. Available: <http://dx.doi.org/10.1016/j.jqsrt.2009.03.002>
- [11] J. M. Conny, R. D. Willis, and D. L. Ortiz-Montalvo, “Optical Modeling of Single Asian Dust and Marine Air Particles: A Comparison with Geometric Particle Shapes for Remote Sensing,” *Journal of Quantitative Spectroscopy and Radiative Transfer*, vol. 254, p. 107197, Oct. 2020. [Online]. Available: <https://doi.org/10.1016/j.jqsrt.2020.107197>
- [12] L. Bi, P. Yang, G. W. Kattawar, and R. Kahn, “Single-scattering properties of triaxial ellipsoidal particles for a size parameter range from the Rayleigh to geometric-optics regimes,” *Applied Optics*, vol. 48, no. 1, pp. 114–126, 2009.
- [13] G. Fang, “Optical Properties of Saharan and Asian Dust: Application to Radiative Transfer Simulations,” Ph.D. dissertation, Texas A&M University, 2012.
- [14] O. Dubovik, A. Sinyuk, T. Lapyonok, B. N. Holben, M. Mishchenko, P. Yang, T. F. Eck, H. Volten, O. Muñoz, B. Veihelmann, W. J. van der Zande, J. F. Leon, M. Sorokin, and I. Slutsker, “Application of spheroid models to account for aerosol particle nonsphericity in remote sensing of desert dust,” *Journal of Geophysical Research Atmospheres*, vol. 111, no. 11, pp. 1–34, 2006.

- [15] S. Merikallio, T. Nousiainen, M. Kahnert, and A.-M. Harri, “Light scattering by the Martian dust analog, palagonite, modeled with ellipsoids,” *Optics Express*, vol. 21, no. 15, p. 17972, 2013.
- [16] J. T. Peterson and J. A. Weinman, “Optical Properties of Quartz Dust Particles at Infrared Wavelengths,” *Journal of Geophysical Research*, vol. 74, no. 20, pp. 6947–6952, 1969.
- [17] D. R. Longtin, E. P. Shettle, J. R. Hummel, and J. D. Pryce, “A Wind Dependent Desert Aerosol Dust Model: Radiative Properties,” Tech. Rep., 1988.
- [18] G. Ghosh, “Dispersion-equation coefficients for the refractive index and birefringence of calcite and quartz crystals,” *Optics communications*, vol. 163, no. 1-3, pp. 95–102, 1999.
- [19] A. Miffre, T. Mehri, M. Francis, and P. Rairoux, “UV-VIS depolarization from Arizona Test Dust particles at exact backscattering angle,” *Journal of Quantitative Spectroscopy and Radiative Transfer*, vol. 169, pp. 79–90, 2016. [Online]. Available: <http://dx.doi.org/10.1016/j.jqsrt.2015.09.016>
- [20] H. C. van de Hulst, *Light Scattering by Small Particles*. Dover Publications, 1981.
- [21] C. F. Bohren and D. R. Huffman, *Absorption and Scattering of Light by Small Particles*. Wiley, 2004.
- [22] W. Somerville, B. Auguié, and E. Le Ru, “smarties: User-friendly codes for fast and accurate calculations of light scattering by spheroids,” *Journal of Quantitative Spectroscopy and Radiative Transfer*, vol. 174, pp. 39–55, May 2016. [Online]. Available: <https://linkinghub.elsevier.com/retrieve/pii/S0022407315302247>
- [23] A. Macke and M. I. Mishchenko, “Applicability of regular particle shapes in light scattering calculations for atmospheric ice particles,” *Applied Optics*, vol. 35, no. 21, p. 4291, 1996.
- [24] M. I. Mishchenko, L. D. Travis, and D. W. Mackowski, “T-matrix computations of light scattering by nonspherical particles: a review,” *Journal of Quantitative Spectroscopy and Radiative Transfer*, vol. 55, no. 5, pp. 535–575, 1996.
- [25] M. I. Mishchenko, L. D. Travis, and A. A. Lacis, *Scattering, Absorption, and Emission of Light by Small Particles*. Cambridge: Cambridge University Press, 2002.
- [26] W. Somerville, B. Auguié, and E. Le Ru, “Severe loss of precision in calculations of t-matrix integrals,” *Journal of Quantitative Spectroscopy and Radiative Transfer*, vol. 113, no. 7, pp. 524–535, 2012.
- [27] —, “A new numerically stable implementation of the t-matrix method for electromagnetic scattering by spheroidal particles,” *Journal of Quantitative Spectroscopy and Radiative Transfer*, vol. 123, pp. 153–168, 2013.
- [28] —, “Accurate and convergent t-matrix calculations of light scattering by spheroids,” *Jour-*

- nal of Quantitative Spectroscopy and Radiative Transfer*, vol. 160, pp. 29–35, 2015.
- [29] A. Macke, J. Mueller, and E. Raschke, “Single Scattering Properties of Atmospheric Ice Crystals,” *Journal of the Atmospheric Sciences*, vol. 53, no. 19, pp. 2813–2825, Oct. 1996.
- [30] K. Muinonen, K. Lumme, J. Peltoniemi, and W. M. Irvine, “Light scattering by randomly oriented crystals,” *Applied Optics*, vol. 28, no. 15, 1989.
- [31] J.-P. Schäfer, “Implementierung und anwendung analytischer und numerischer verfahren zur lösung der maxwellgleichungen für die untersuchung der lichtausbreitung in biologischem gewebe,” Ph.D. dissertation, Verlag nicht ermittelbar, 2011.

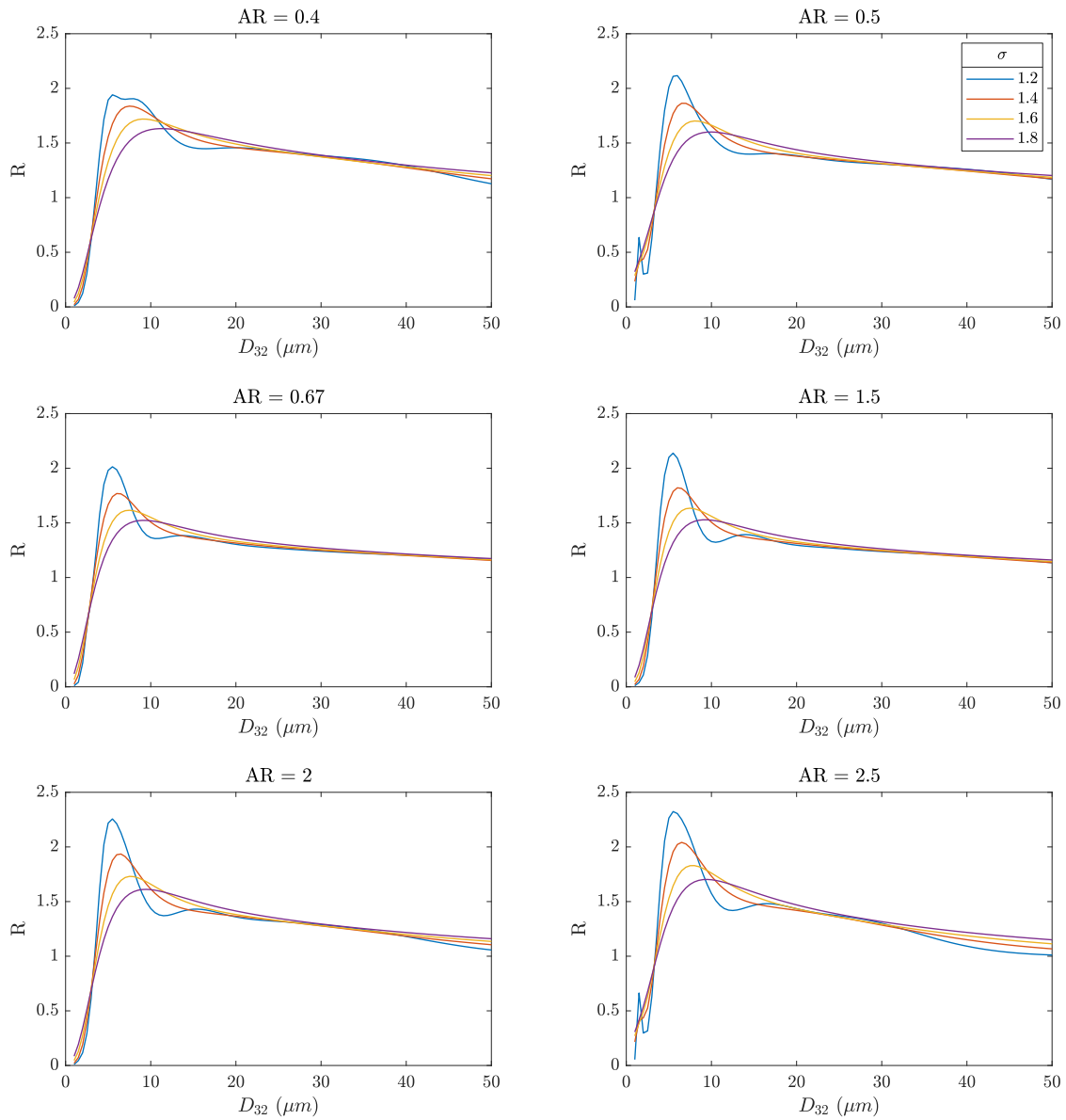


Figure 6.5: Extinction ratio between 10330 nm and 532 nm for the various aspect ratios and distribution widths for CSPEC sand. The refractive indices for the respective wavelengths are listed in Table 6.1.

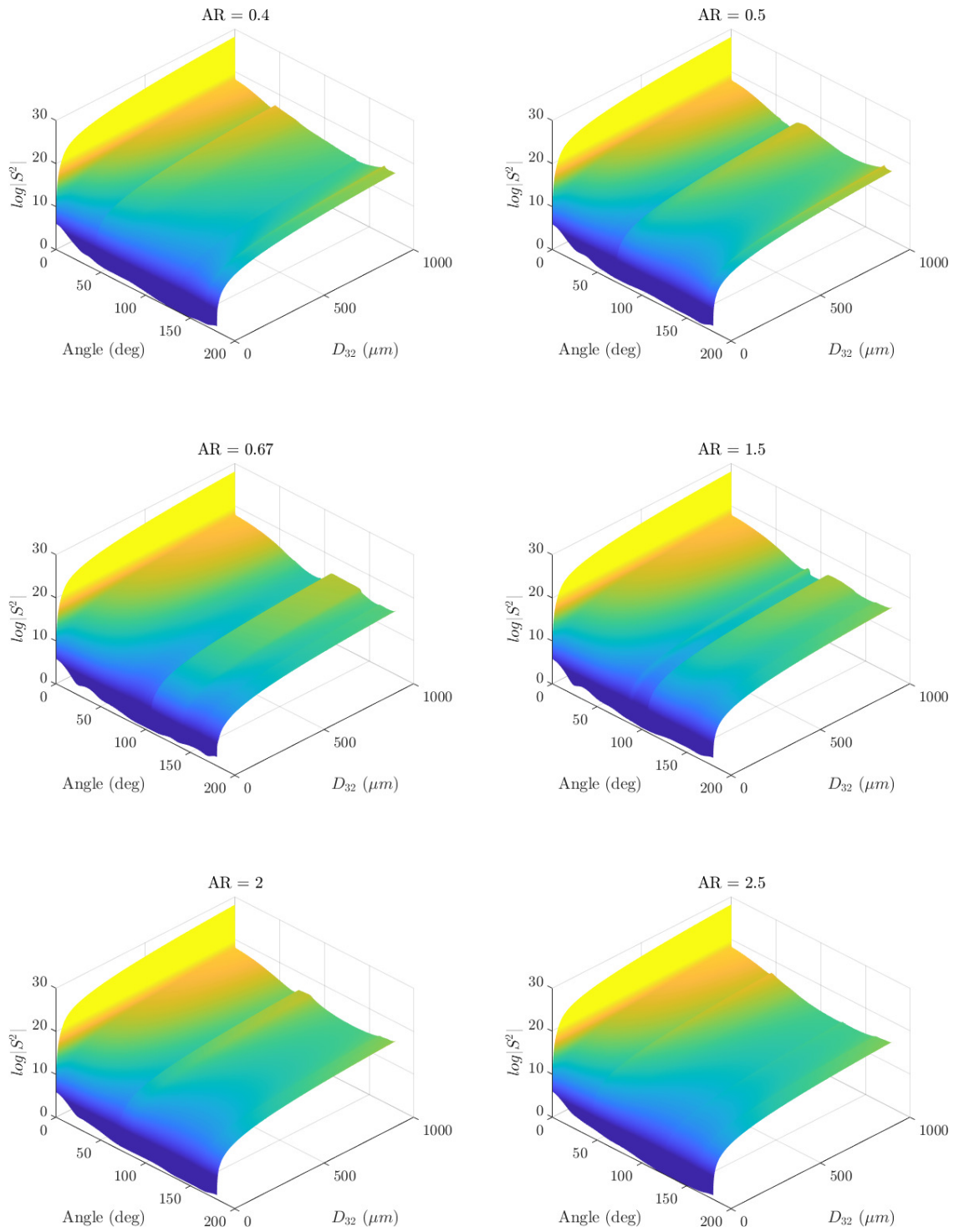


Figure 6.6: Scattering profiles from the CSPEC library for various aspect ratios and Sauter mean diameters. The distribution width σ has been limited to 1.4 for clarity.

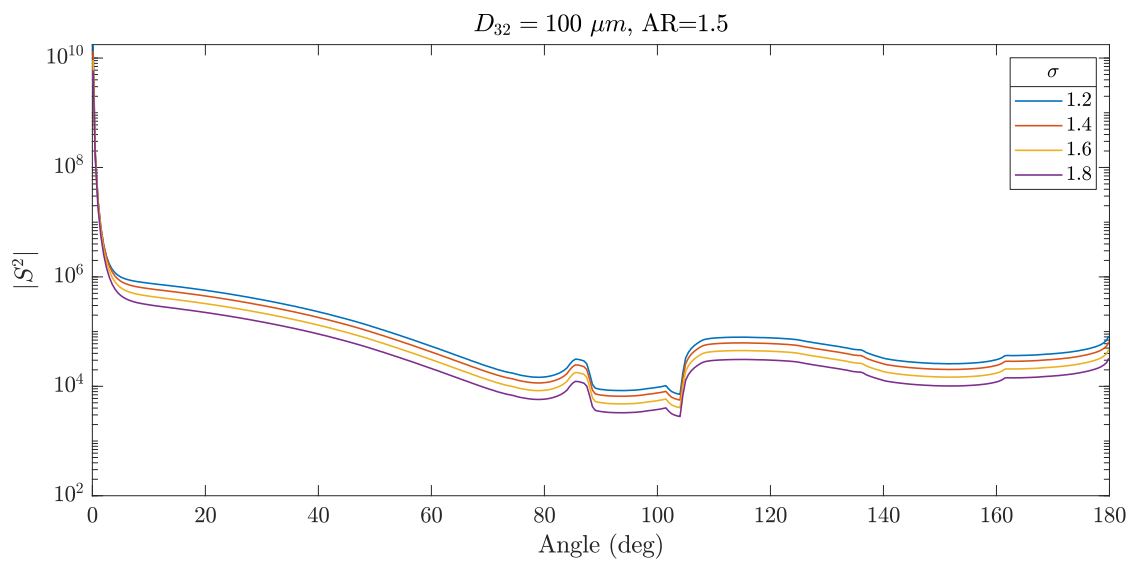


Figure 6.7: Scattering profiles from the CSPEC library for $D_{32} = 100 \mu m$ and $AR = 1.5$ with various aspect ratios.

7. Conclusions and Outlook

7.1 Conclusions

This dissertation details a particle sensor technology utilizing machine learning models using light scattering and extinction as features. An extensive literature review in chapter 2 establishes the particle ingestion problem for gas turbines and existing particle measurement techniques. Key limitation for current technologies are complex particle shape and challenging environmental factors in gas turbines.

The first manuscript in chapter 3 provides an early framework for the machine learning approach. Using only scattering as the input feature, sand and ash particles from the Amsterdam and Grenada particle scattering database are accurately sized. It also features the first attempt at a layered models approach, where a number of supervised machine learning models are used to sort the input into secondary layers of models, which then provide precise estimations. The importance of having non-spherical particles in the library to guide the models during the training process is highlighted in this article as well.

The second and third manuscripts are focused on the application of this sensor technology in realistic inlet environments. The second manuscript in chapter 4 describes the measurement of condensation in a research engine using this method. The liquid volume flow rate of a water spray located upstream of the bellmouth inlet of a JT15D engine is accurately measured by the machine learning models using light scattering and extinction as features. This marks the first time extinction was used as a feature, and to the author's knowledge, also the first time inlet condensation was measured without a prior calibration using any method.

The third manuscript in chapter 5 details an experiment performed in a high-speed wind tunnel to measure the mass flow of the sand particles injected into the flow. A generalized neural network approach replaces the layered models methods detailed in chapters 3 and 4.

The standalone chapter 6 contains a detailed explanation of how the particle scattering and extinction library is constructed, including the various particle parameters and the numerical tools. It also includes a discussion of the library contents prepared for the solid particle mass loading sensor, demonstrated in chapter 5.

7.2 Outlook

The presented research is an exciting combination of applied machine learning and conventional optical measurement techniques. In addition to monitoring applications as a sensor, the capabilities of this method can be used to augment other research efforts. In controlled experiments for studying the effects of particle ingestion in engines, manufactured sample particles are typically injected into the relevant flow in a similar manner to the experiments described in the previous chapters. Simulations studying similar flows and conditions need initial or boundary conditions of the injected particles as well. A measurement of the particle size distribution in a more realistic situation using this technique could then provide more representative experimental and boundary conditions for these efforts.

In particular, simulated studies can reveal valuable insights into particle trajectories and which components would be vulnerable to particular size or shape of particles [1, 2, 3, 4]. This technology could be an enabling technology for measurements not only for the initial particle conditions, but for validations as well. As an example, a simulated study by Vogel et al. revealed that in turbofans, the fan can act as a sort of a filter, removing some of the larger particles from the core flow [3]. The ML measurement technique could be deployed on a simplified experimental rig for validating the mass flow and size differences between the core and the bypass flows. The gas-particle phase flow simulation scheme could then be used with more confidence in larger scales, where experiments with damaging sand and costly equipment would not be feasible.

One of the advantages with this approach is that the supplied training data provides the underlying physics to the models. This means the library can be adjusted and varied as the requirements for the sensor change. In addition, the feature framework can vary as well, changing the input measurement techniques and/or the inputs themselves for future improvements. Summarizing the different ways this method can improve in the future:

- Ice crystals and hail, one of the major hazards for gas turbine operations, has not yet been measured using this concept. Multitudes of tools and databases already exist for optical properties of ice crystals and representative shapes, which could be adapted for the machine learning framework for ice detection and identification [5, 6].
- Volcanic ash also has not been directly measured by the author for validation. Further research into optical modeling of volcanic ash using surrogate shapes would be necessary for extending the method for those particles.

- The measurement methods for light scattering intensities could be simplified using techniques found in the literature. Hussain et al. and Oltmann et al. both present unique methods to capture multi-angle light scattering using a single camera [7, 8]. Adaptation of similar techniques could reduce the measurement complexity and improve the data acquisition process.
- Further investigations into additional input features could prove valuable, with quantities such as the depolarization ratio and back-scattering intensities. Optical modeling studies of dust particles have revealed valuable observations for particle size and shape regarding those additional features [9].

References

- [1] J. P. Bons, R. Prenter, and S. Whitaker, “A simple physics-based model for particle rebound and deposition in turbomachinery,” *Journal of Turbomachinery*, vol. 139, no. 8, 2017.
- [2] O. Desjardins, R. Fox, and P. Villedieu, “A quadrature-based moment method for dilute fluid-particle flows,” *Journal of Computational Physics*, vol. 227, no. 4, pp. 2514 – 2539, 2008. [Online]. Available: <https://doi.org/10.1016/j.jcp.2007.10.026>
- [3] A. Vogel, A. J. Durant, M. Cassiani, R. J. Clarkson, M. Slaby, S. Diplas, K. Krüger, and A. Stohl, “Simulation of Volcanic Ash Ingestion Into a Large Aero Engine: Particle–Fan Interactions,” *Journal of Turbomachinery*, vol. 141, no. 1, pp. 1–12, Jan. 2019.
- [4] A. Ghenaïet, R. L. Elder, and S. C. Tan, “Particles Trajectories Through an Axial Fan and Performance Degradation due to Sand Ingestion,” in *Volume 1: Aircraft Engine; Marine; Turbomachinery; Microturbines and Small Turbomachinery*, vol. 1. American Society of Mechanical Engineers, Jun. 2001, pp. 1–12. [Online]. Available: <https://asmedigitalcollection.asme.org/GT/proceedings/GT2001/78507/NewOrleans,Louisiana,USA/249360>
- [5] L. Bi, “Light scattering by ice crystals and mineral dust aerosols in the atmosphere,” Ph.D. dissertation, Texas A & M University, 2012.
- [6] P. Yang, L. Bi, B. A. Baum, K. N. Liou, G. W. Kattawar, M. I. Mishchenko, and B. Cole, “Spectrally consistent scattering, absorption, and polarization properties of atmospheric ice crystals at wavelengths from 0.2 to 100 μm ,” *Journal of the Atmospheric Sciences*, vol. 70, no. 1, pp. 330–347, 2013.
- [7] R. Hussain, M. A. Noyan, G. Woyessa, R. R. R. Marín, P. A. Martinez, F. M. Mahdi, V. Finazzi, T. A. Hazlehurst, T. N. Hunter, T. Coll *et al.*, “An ultra-compact particle size analyser using

- a cmos image sensor and machine learning,” *Light: Science & Applications*, vol. 9, no. 1, pp. 1–11, 2020.
- [8] H. Oltmann, J. Reimann, and S. Will, “Single-shot measurement of soot aggregate sizes by wide-angle light scattering (WALS),” *Applied Physics B*, vol. 106, no. 1, pp. 171–183, Jan. 2012. [Online]. Available: <http://link.springer.com/10.1007/s00340-011-4781-z>
- [9] T. Nousiainen, “Optical modeling of mineral dust particles: A review,” *Journal of Quantitative Spectroscopy and Radiative Transfer*, vol. 110, no. 14-16, pp. 1261–1279, Sep. 2009. [Online]. Available: <http://dx.doi.org/10.1016/j.jqsrt.2009.03.002>